

AN ABSTRACT OF THE THESIS OF

Kristin A. Marshall for the degree of Master of Science in Chemical Engineering presented on March 16, 2017.

Title: Extensional Characterization of Weakly-Viscoelastic Fluids: Methods & Applications

Abstract approved: _____

Travis W. Walker

The addition of macromolecules to solvent, even in dilute quantities, can significantly alter a fluid's response in an extensional, or stretching, flow. When high-molecular-weight polymers are extended in solution, extensional thickening can result, yielding viscosities that are orders of magnitude larger than values found in shear. Examples of applications where weakly-viscoelastic fluids are used include inkjet printing, turbulent drag flow reduction, and the atomization of fertilizers and pesticides, and understanding the response of such fluids, particularly in extension, is important for making relevant processing and design decisions. The present research was conducted in an effort to make improvements to and to provide an in-depth assessment of the techniques available for characterizing semi-dilute and dilute polymer solutions. Specifically, old and new methods in capillary breakup extensional rheometry are explored. Outcomes of this work include the creation of two new devices for extensional characterization and the completion of a study comparing a number of previously described extensional techniques in an effort to investigate discrepancies and identify limitations in device usage.

©Copyright by Kristin A. Marshall
March 16, 2017
All Rights Reserved

Extensional Characterization of Weakly-Viscoelastic Fluids: Methods
& Applications

by

Kristin A. Marshall

A THESIS

submitted to

Oregon State University

in partial fulfillment of
the requirements for the
degree of

Master of Science

Presented March 16, 2017
Commencement June 2017

Master of Science thesis of Kristin A. Marshall presented on March 16, 2017.

APPROVED:

Major Professor, representing Chemical Engineering

Head of the School of Chemical, Biological, Environmental Engineering

Dean of the Graduate School

I understand that my thesis will become part of the permanent collection of Oregon State University libraries. My signature below authorizes release of my thesis to any reader upon request.

Kristin A. Marshall, Author

ACKNOWLEDGEMENTS

The work herein would not have been possible without the support and guidance of my advisor, Dr. Travis Walker. I would like to thank Dr. Walker for his mentorship over the past two years and for introducing me to the complex and intriguing world of rheology. In this time, I have grown as a student and as a researcher and I am deeply appreciative of Dr. Walker's belief in me and my academic endeavors. Additionally, I would like to thank Dr. Skip Rochefort and my peers in the Rheology Research Group (and elsewhere at OSU) for their time and helpful conversations. Specifically, I would like to acknowledge Britany Swann, Katrina Donovan, Uranbileg Daalkhajav, Ehsan Taghizadeh, Mingyang Tan, Shelley Haug, Alix Robel, Sassan Ostvar, and the CBEE graduate student association. Having an open platform to share my thoughts and receive constructive feedback has been incredibly valuable. Aleesha Liedtke, Zach Wallace, Ryan Kristian Cashen, Anika Todt, and Katie Moreno, words cannot express how appreciative I am of your hard work and eagerness to learn. Thank you for allowing me to serve as your mentor and for helping me to propel my research forward.

I would also like to acknowledge my mother and father for their unconditional love and for supporting my decision to return to school. I would also like to acknowledge my brothers, Jared and Derek, for always pursuing their dreams. If it were not for them, I would not be pursuing mine. I would like to acknowledge Clem and Mu for keeping me company on this journey. Clem, thank you for your patience and constant encouragement, and thank you for being a great roommate and co-parent to Mu. And Mu, thank you for being a cat.

Lastly, I would like to thank the school of Chemical, Biological, and Environmental Engineering at OSU and all of the faculty, advisors (Kristin Rorrer, Anita Hughes), and staff (Elisha Brackett, Charlotte Williams, Lea Clayton) that have helped me along the way. Thank you, thank you, thank you, for taking a chance on me.

TABLE OF CONTENTS

	<u>Page</u>
1 Introduction	1
1.1 Introduction to Rheology	1
1.2 Motivation	2
1.3 Background	5
1.3.1 Dilute Polymer Solutions	5
1.3.2 Extensional Rheology	10
1.3.3 Challenges in Characterizing Weak Viscoelasticity	26
1.3.4 Rheology on the Microscale	34
2 Investigating the dynamics of droplet breakup in a microfluidic cross-slot device for characterizing the extensional properties of weakly-viscoelastic fluids	36
2.1 Abstract	36
2.2 Introduction	37
2.3 Materials and Methods	47
2.3.1 Microfluidic Design and Fabrication	47
2.3.2 Experimental Setup	49
2.3.3 Selection of Continuous- and Dispersed-Phase Solutions	54
2.4 Results & Discussion	59
2.4.1 Droplet Formation at the T-Junction	59
2.4.2 Droplet Breakup for Newtonian and Viscoelastic Fluids	65
2.4.3 Comparison of the DoS and PRIMER techniques	72
2.4.4 Flow-Rate and Continuous-Phase Sensitivity	75
2.4.5 Viscoelasticity of the Dispersed-Phase	78
2.5 Conclusions & Future Work	81
2.6 Acknowledgements	85
3 Handheld Extensional Rheometry with a Mobile Device	86
3.1 Abstract	86
3.2 Introduction	86
3.2.1 Extensional Rheology	87
3.2.2 Capillary Breakup Extensional Rheometry	89
3.3 Experimental Verification	91
3.3.1 Materials & Test Solutions	91
3.3.2 Dripping-onto-Substrate (DoS)	93
3.3.3 Smartphone Protocol	93
3.4 Results & Discussion	94

TABLE OF CONTENTS (Continued)

	<u>Page</u>
3.4.1 Step-strain Comparison	94
3.4.2 DoS Comparison	97
3.4.3 Time-Scale Considerations	98
3.4.4 Length-Scale Considerations	105
3.5 Conclusion and Future Work	106
3.6 Acknowledgements	107
4 General Conclusions	108
Bibliography	110

LIST OF FIGURES

Figure	Page
1.1 Enhanced particle removal (EPR) of 1 μm fluorescent SiO_2 particles from the surface of silicon wafers at varying concentrations of poly(ethylene oxide) (PEO) (MW = 7×10^6). Concentrations were selected to be below the coil overlap concentration, c^* , calculated using the Mark-Houwink-Sakurada for PEO in deionized water (DIW). Data courtesy of R. K. Cashen.	4
1.2 A series of images describing polymer/solvent and polymer/polymer interactions based on the concentration of polymer in a given solvent. On the left, an idealized linear polymer occupies a volume of radius, R_g , that depends on the molecular weight of the polymer, solvent quality, and temperature of the system. The remaining images depict systems containing multiple polymer chains, described by the critical overlap concentration, c^* , adapted from [1]. The three regimes include dilute ($c < c^*$), semi-dilute ($c \approx c^*$), and entangled ($c \gg c^*$) polymer solutions.	6
1.3 Uniaxial extension of a cylindrical filament of initial length L_0 . The fluid is being stretched at a rate $\frac{dL}{dt}$. To maintain a constant strain rate, the length of the filament, L , must grow exponentially in time ($L = L_0 \exp[\dot{\epsilon}t]$).	14
1.4 Parameter space characterizing free surface flows of viscoelastic fluids, adapted from [2]. The parameter space is dependent on parameters the capillary, Reynolds, and Weissenberg numbers to describe the relative capillary, inertial, and elastic contributions to the flow. From these parameters, the elastocapillary, elasticity, and Ohnesorge numbers can be evaluated.	17
1.5 Parameter space characterizing capillary self-thinning of viscoelastic filaments using viscous, inertial, and elastic time scales describing a breakup event adapted from [2]. The limitations for the CaBER are plotted, below which measurements cannot be taken. The locations for fluids studied in EPR and TDR are sketched as well as the locations for Boger fluids. The dashed-arrow represents where the elastocapillary number is unity, $Ec = 1$	20
1.6 Representative CaBER data for Newtonian and viscoelastic fluids. The diameter is normalized by the diameter of the filament after the initial step-strain, D_1 . The black-dashed line represents the linear (Newtonian) fit and the black-dotted line represents the exponential (viscoelastic) fit of the data according to Equations 1.23 and 1.34, respectively.	26

LIST OF FIGURES (Continued)

Figure	Page	
1.7	Dynamic oscillatory shear test depicting the crossover frequency, ω_c , where the storage modulus (G') and loss modulus (G'') intersect. The characteristic relaxation time of a polymer solution, λ , can be approximated as the inverse of the crossover frequency, $1/\omega_c$. Higher frequencies are needed to evaluate the characteristic relaxation times of weakly viscoelastic solutions, represented by the comparison of G'_1 and G'_2 relative to G''	27
1.8	(a) DoS setup adapted from [3]. (b) In-house setup with the components: (i) Phantom [®] V4.1 high-speed camera, (ii) syringe holder and syringe, (iii) substrate (glass slide), (iv) motorized syringe pump, (v) tube lens and 10x objective, and (vi) light source.	31
1.9	DoS diameter decay profiles for (a) a 60 wt% glycerol/deionized (DIW) water solution and (b) a 65 wt% glycerol/DIW with 65 ppm PEO. The breakup of the Newtonian glycerol/DIW solution is observed to occur rapidly, whereas the breakup of the viscoelastic PEO solution occurs in over double the amount of time. Additionally, no noticeable filament formation is observed for the glycerol/DIW solution.	32
1.10	DoS diameter decay plots for 250- and 500-ppm aqueous PEO solutions. (a) Natural log of the diameter versus time. (b) Natural log of the normalized diameter versus normalized time. The diameter is normalized by the initial diameter of the filament, D_0 . Time is normalized by the relaxation times (1.3 ms and 4.3 ms) evaluated for the two samples, λ_E	33
2.1	Applications employing semi-dilute and dilute polymer solutions. (a) Polymers used in subsurface flows include surfactants for enhanced oil recovery. Pore sizes can vary from nanometers to millimeters, impacting how a fluid is transported. (b) In turbulent drag flow reduction, polymers hinder the formation of turbulent eddies and reduce energy costs associated with pumping. (c) In enhanced particle removal, the addition of polymer to chemical mechanical planarization (CMP) chemistries can assist in the removal of micro- and nano-sized particles from the surfaces of silicon wafers in semi-conductor processing. (d) Polymers are added to inkjet printing chemistries to increase the robustness of the ink and to eliminate satellite droplets. Viscoelastic behavior is noted as small volumes of ink are jetted from micron-sized nozzles.	38

LIST OF FIGURES (Continued)

Figure	Page	
2.2	<p>A schematic of droplet splitting at the stagnation point of a microfluidic device. (a) A generic cross-slot configuration is presented with opposing inlet and outlet channels (solid lines). A stagnation point is depicted at the center of the geometry. To reduce shearing effects at the channel walls and to promote a purely extensional flow, the shape of the cross-slot can be modified (dashed-lines) as discussed by Haward et al. [4]. (b) Droplet splitting at the stagnation point of the cross-slot is depicted. Initially, the droplet is elongated towards the outlet channels until a rapid breakup event is initiated. (c) An enlarged view of the cross-slot where filament thinning is presented. For viscoelastic fluids, filaments can be formed that connect the two droplet segments. The resulting filament decay profile is monitored and analyzed using a similar approach as in CaBER experiments.</p>	46
2.3	<p>The two main geometries used in the PRIMER design. (a) A T-junction geometry used to create droplets as the continuous phase silicone oil pinches the dispersed-phase sample. (b) A cross-slot geometry used to initiate a droplet-breakup event at a stagnation point.</p>	47
2.4	<p>An overall schematic of the cross-slot device, including the continuous- and dispersed-phase inlet channels with widths of w and w_{in}, respectively. The length, l_d, and time spacing, t_d, between droplets were controlled by adjusting the ratio of the continuous and dispersed-phase flow rates, q_{cont}/q_{disp}. The height of the device, h, was similar in magnitude to the width of the channels. The width of the cross-slot, w_{xslot}, was greater than the width of the channels, minimizing wall effects.</p>	49
2.5	<p>Image processing of droplets forming at a T-junction. Droplets are tracked based on parameters such as orientation and size relative to other objects in the frame.</p>	51
2.6	<p>Image processing of a single droplet-breakup event in the cross-slot of the PRIMER device at early, middle, and late times. Images were captured in grayscale and converted to binary using a custom-built MATLAB[®] code. (a) Raw images captured in grayscale. (b) A binary filter applied to the raw images. (c) A custom filter applied to remove background noise.</p>	52
2.7	<p>Validating the accuracy of the syringe pumps used in the present study. A comparison of the volumetric flow rates evaluated by droplet tracking (V_{actual}) to the summation of the continuous (V_{cont}) and dispersed phase (V_{disp}) flow rates input into the syringe pumps.</p>	53

LIST OF FIGURES (Continued)

Figure	Page
2.8 AR-G2 flow sweep results for the 10 to 500-ppm PEO ($MW = 7 \times 10^6$) solutions tested using the cross-slot microfluidic device. Shear characterization was performed at 25°C. The black dashed lines indicate where low-torque (left limits) and inertial effects (right limits) may lead to errors in measurement, evaluated according to Ewoldt et al [5].	56
2.9 AR-G2 flow sweep results for the 5000-ppm PEO ($MW = 7 \times 10^6$) stock solution tested using the cross-slot microfluidic device. Shear characterization was performed at 25°C	57
2.10 AR-G2 flow sweep results for the glycerol/DIW solutions tested using the cross-slot microfluidic device. Shear characterization was performed at 25°C. The data reflects compositions of 10 (Δ), 80 (\square), and 90 (\diamond) wt% glycerol.	57
2.11 Droplet formation at a T-junction for a 5000-ppm PEO solution in 200-mPa·s silicone oil over a range of flow rates from 0.01 ml/hr to 1 ml/hr. The blue solid-line indicates a linear fit using Equation 2.10: $V/(hw^2) = V_f/(hw^2) + \alpha q_{disp}/q_{cont}$, where $V_f/(hw^2)$ and α were found to be 1.4 and 2, respectively. The blue dashed-line indicates the line predicted using the theoretical model presented by van Steijn et al. [6], where values for $V_f/(hw^2)$ and α have been evaluated to be approximately 1 and 2, based on the geometry of the T-junction.	62
2.12 time spacing, t_d , and filling period, Δt_f^* , for 5000-ppm PEO droplets formed at a T-junction over a range of flow rates from 0.01 ml/hr to 1 ml/hr dispersed in 200-mPa·s silicone oil. The black dashed-line represents the line of equality between the abscissa and ordinate. The filled-squares represent droplets successfully split in the cross slot without interference. The unfilled squares represent droplets that split with interference from another incoming droplet. The star symbols represent droplets that did not break and that instead entered either outlet channel. For droplets to break without interference, larger time spacings were required.	66

LIST OF FIGURES (Continued)

<u>Figure</u>	<u>Page</u>
<p>2.13 Criteria for the successful breakup of droplets in a cross-slot for a 5000-ppm PEO solution dispersed in a 200-mPa·s silicone oil over a range of flow rates from 0.01 ml/hr to 1 ml/hr. The time spacing of the droplets is normalized by the relaxation time of the dispersed phase and is plotted against the initial aspect ratio of the droplets, $l_d/(\pi w)$. The filled-squares represent droplets successfully split in the cross-slot without interference. The unfilled-squares represent droplets that split with interference from another incoming droplet. The star symbols represent droplets that did not break. For a successful breakup event to be observed, both the size and spacing of the droplets is important.</p>	67
<p>2.14 Droplet breakup of Newtonian and viscoelastic fluids in the cross-slot of the PRIMER device. At time $t=0$, capillary pressures initiate the droplet-breakup event. (a) A 10-wt% glycerol/water solution rapidly decays in time. Sattelite droplets are observed at late times, and depending on the viscosity of the glycerol/water solution, the number and size of these satellite droplets vary. (b) A 500-ppm PEO/water solution forms a cylindrical filament that decays exponentially in time. At late times, the well-known beads-on-a-string morphology is observed, and depending on the concentration of PEO, the size of the initial filaments and the structure of the beading patterns vary. . . .</p>	69
<p>2.15 Diameter decay profile for a droplet of 5000-ppm PEO stock solution at a range of points along the filament profile. Four distinct regimes are noted including (i) the early stretching and necking of the droplet as it reaches the stagnation point, (ii) a rapid decrease in the diameter caused by dominating capillary forces, (iii) an elastocapillary regime where the growth of elastic stresses compete with the capillary pressures driving the breakup process, and (iv) the formation of the beads-on-a-string morphology. The initial time at $t=0$, is the time at the end of regime (ii) in which a filament forms. The natural logarithm of the diameter at this point is highlighted on the plot. . .</p>	71
<p>2.16 A comparison of diameter-decay profile for a 5000-ppm PEO stock solution using PRIMER and DoS techniques. For the PRIMER results (green triangles), a 200-mPa·s silicone oil was used as the continuous phase fluid. The solid lines represent the linear fits in the elastocapillary regime of interest, where relaxation times can be extracted.</p>	73
<p>2.17 Plot of diameter versus time for varying flow rates for stock solution of 5000-ppm PEO dispersed in 200-mPa·s silicone oil. The slope of the initial viscous-drag regime is increased as the overall flow rates in the device are increased.</p>	76

LIST OF FIGURES (Continued)

<u>Figure</u>	<u>Page</u>
<p>2.18 Results for trials varying the size of the droplets, a function of q_d/q_c, and the capillary number, a function of U_c and μ_c using the 5000-ppm PEO dispersed in 200-mPa·s silicone oil. (a) The extensional relaxation time is plotted versus the ratio of the dispersed- and continuous-phase flow rates. (b) The extensional relaxation time is plotted versus the capillary number. The filled-black markers represent varying continuous-phase viscosity at a fixed flow ratio, $q_{disp}/q_{cont} = 0.8$. The blue-dotted lines represent the relaxation time characterized in the DoS trial.</p>	77
<p>2.19 Diameter-decay profiles for filaments at concentrations of 10, 50, 100, and 500 ppm PEO. The natural logarithm of the diameter is plotted versus time. Only the 500-ppm solution had a elastocapillary regime that could be fit.</p>	79
<p>2.20 Beading profiles for filaments of PEO at (a) 5000, (b) 500, (c) 100, (d) 50, (e) 10 ppm PEO dispersed in 200-mPa·s silicone oil. When going to lower concentrations, the initial size of the filament decreased and the beading profiles were altered.</p>	80
<p>2.21 A sample pump design for the PRIMER. Two flow sensors are used to accurately monitor the flow rates into the device. Pressure sensors at the waste streams can be used to control the droplet-splitting event.</p>	83
<p>2.22 Sample geometry designs for the PRIMER. (a) CaBER-like design in which a droplet is rapidly extended and then remains still to allow for the self-thinning of a filament. (b) FISER-like design where a filament is extended at a constant strain rate.</p>	84
<p>3.1 Saliva spinnbarkeit test performed by stretching saliva between two glass slides and observing the formation and breakup of the resulting filament as the slides are pulled apart.</p>	88
<p>3.2 Capillary-breakup techniques for characterizing the extensional properties of fluids, with relevant dimensions including D_0, D_1, and L_1. (a) A schematic of the DoS technique adapted from Dinic et al. [3]. (b) The thinning and breakup of a filament by allowing a sample to wet the surface of a substrate (DoS). (c) The formation of a filament using one's index finger by placing a sample on a glass substrate and stretching the sample to a set height. (d) The formation of a filament using a clothespin by placing a sample between the prongs of a wooden clothespin and stretching the sample to a set height.</p>	92

LIST OF FIGURES (Continued)

Figure	Page	
3.3	<p>Comparison of results for the techniques providing an initial step-strain to a material. (a) Normalized diameter-decay profile using the index-finger method in an attempt to stretch and hold a sample at a set height. (b) Normalized diameter decay profile using the clothespin method to stretch and hold a sample at a set height. Ten trials were performed for each technique and the average of the ten trials is given (black-dotted curves). Diameter profiles were normalized by the diameter of the filament after the initial step-strain, D_1. Images depicting the filament-breakup process are included for each technique.</p>	95
3.4	<p>Filament decay profiles for concentrations of (a) 660 ppm, (b) 110 ppm, (c) 40 ppm, and (d) 20 ppm PEO in a glycerol/water solution. The time for filament breakup is dependent on the concentration of PEO in the solution.</p>	96
3.5	<p>Comparing the resulting decay profiles for the DoS and smartphone techniques. (a) Normalized diameter decay profiles for Boger fluids with PEO concentrations ranging from 20 ppm to 660 ppm tested using the DoS technique. The initial diameter, D_0, is defined as the diameter of the syringe tip used to expel the sample [3]. (b) Averaged diameter results from the clothespin method for ten repetitions for Boger fluids with PEO concentrations ranging from 20 ppm to 660 ppm. Solid black lines on the diameter decay profiles indicate the exponential fits of the elasto-capillary regime. . .</p>	99
3.6	<p>Resulting relaxation times (λ_E) versus concentration (Φ) for the DoS (black diamonds) and clothespin (blue circles) techniques. Dashed lines indicate a power law fit of the relaxation time versus concentration, $\lambda_E \propto \Phi^\alpha$. The clothespin relaxation times represent the average relaxation times over ten trials, with error bars representing the standard deviation of these trials. A single point (red square) for the index-finger method is plotted for the 660-ppm Boger fluid and shows good agreement with the clothespin method.</p>	100
3.7	<p>Results for fifteen trials of the 4,870-mPa·s silicone oil. The normalized diameter is plotted versus time. The average of the fifteen trials (black stars) and the linear fit (blue line) are also included.</p>	104
3.8	<p>Diameter decay results for a range of 41 points along the length of a filament for the 660 ppm Boger fluid. The raw pixel length is plotted versus the frame number. The average of the results (black points) are included. Depending on the point along the length of the filament, the slope calculated from the line of best fit fell within 15% of the average. Thus, a small amount of error is introduced in the location along the filament from which a measurement is taken.</p>	106

LIST OF TABLES

<u>Table</u>		<u>Page</u>
1.1	Mark-Houwink-Sakurada data for poly(ethylene oxide) in water adapted from the Polymer Handbook [7].	7
1.2	A summary of predicted scaling laws for dilute polymer solutions with dominant hydrodynamic interactions [8,9]. M is the molecular weight of a polymer chain and ν is the Flory exponent.	10
1.3	Comparison of extensional rheological techniques for mobile polymer solutions.	13
2.1	A summary of the dispersed-phase solutions tested in the PRIMER device, including viscoelastic solutions composed of poly(ethylene oxide) (PEO) in deionized water and Newtonian glycerol (GLY)/water solutions.	54
2.2	A summary of the continuous- and dispersed-phase flow rates tested for the 5000-ppm stock solution dispersed in the 200-mPa·s in the PRIMER.	75
3.1	Composition and physical properties of test fluids.	92

Chapter 1: Introduction

1.1 Introduction to Rheology

Rheology is the science that investigates the deformation and flow properties of various types of matter. Albeit a highly specialized field, rheologists are equipped to tackle a wide range of problems by combining a fundamental understanding of physics, thermodynamics, and transport phenomena. On the bulk scale, most fluids do not behave as simply as water or air and may exhibit a solid-like “memory.” Such fluids are labeled as complex and make up the majority of the biological and synthetic fluids that govern our lives.

Characterizing how materials will respond to given deformations is imperative for making relevant processing and design decisions in industry and for understanding transport phenomena in complex media. For example, the resulting material properties of a plastic product may change depending on the how the plastic (polymer melt) is extruded. Thus, characterizing the rheology of the polymer melt is important for the design of the extruder and for controlling the resulting mechanical properties of the object. Other examples where rheology serves an important role include the characterization of biological fluids, such as mucus, the design of better drug delivery systems [10, 11], the development and quality control of food and cosmetic products [12], and the selection of additives that can assist in enhanced oil recovery and subsurface remediation [13, 14].

A fluid’s response to a given deformation is determined by whether the fluid’s solid-like (elastic) or liquid-like (viscous) properties dominate. Over the past century, ample research has focused on the development of rheological techniques to quantify such “viscoelastic” behavior and to provide insight on the macro- and molecular-scale parameters that influence flow. Although the majority of the literature focuses on shear techniques, the present thesis

will address an important, yet far less utilized, method for rheological characterization – extensional rheometry and its applications – and discuss the development of two novel techniques for extending current measurement capabilities.

The present thesis contains two manuscripts. The first manuscript (Chapter 2) discusses the extensional characterization of weakly-viscoelastic liquids in the cross-slot geometry of a microfluidic device by examining droplet breakup at a stagnation point. The second manuscript (Chapter 3) explores a portable, low-cost means of capillary breakup extensional rheometry by employing the high-speed video capabilities of a smartphone device. The present work concludes with a statement on the current state of capillary breakup extensional rheometry and discusses recommendations for future research.

1.2 Motivation

The motivation for the present work stems from areas of research ranging from turbulent drag flow reduction (TDR) to enhanced particle removal (EPR), where changes in the performance of working fluids have been observed with the addition of small quantities of high-molecular-weight polymer. In enhanced particle removal, for example, the addition of semi-dilute and dilute concentrations of polyacrylamide (PAM) to chemical mechanical planarization (CMP) chemistries has been shown to aid in the removal of micron-sized particles from the surfaces of silicon wafers [15]. EPR is attractive for semiconductor manufacturing, where an essential step in the semiconductor fabrication process is to clean and smooth the surfaces of silicon wafers. Example data showing the effects of small quantities of high-molecular-weight polymer on particle-removal efficiency is included below (Figure 1.1). Similarly, in turbulent drag flow reduction, the presence of polymer has been shown to dampen the formation of turbulent eddies. This phenomena is known to reduce the energy costs required for pumping, and it has been shown to enhance certain irrigation and fire fighting systems [16, 17].

As the saying goes, “less is more,” and in applications utilizing dilute and semi-dilute polymer solutions, achieving the same performance with smaller amounts of polymer is desirable, limiting material costs and keeping shear viscosities low. Problems, however, arise when attempting to characterize such weakly-viscoelastic fluids, and correlating a fluid’s material properties to its performance can prove difficult. The present thesis addresses such issues, exploring novel techniques for characterizing dilute and semi-dilute polymer solutions having lower shear viscosities. In the present section, topics to be discussed include what constitutes a dilute polymer solution, important considerations when selecting appropriate characterization techniques, and why weak viscoelasticity is difficult to characterize.

Example Data for Enhanced Particle Removal (EPR): Figure 1.1 presents preliminary data collected for EPR studies using high-molecular-weight poly(ethylene oxide) (PEO) ($MW = 7 \times 10^6$) dissolved in deionized water (DIW) as the working fluid. In the experimental setup, a silicon wafer was coated with micron-size fluorescent particles. To remove the particles from the wafer’s surface, CMP processes were employed that involved dispensing the working fluid over the wafer’s surface while simultaneously rotating the wafer. To observe how weak viscoelasticity impacts particle removal, varying concentrations (0, 4, 40, 100, 200, and 400 ppm) of high molecular-weight-PEO were used.

From the data collected, a trend in percent removal of particles is observed with increasing PEO concentration (Figure 1.1). Relative to removal using pure DIW, the addition of even 4 ppm of PEO yielded a nearly 10% jump in particle removal. When characterizing the shear rheology of the PEO solutions, all solutions behaved Newtonian over the range of shear rates tested ($10 - 10^3 \text{ s}^{-1}$), having shear viscosities on the same order of magnitude as water $O(1 \text{ mPa}\cdot\text{s})$. Despite “appearing” the same, these solutions had quantifiable differences in particle removal efficiency.

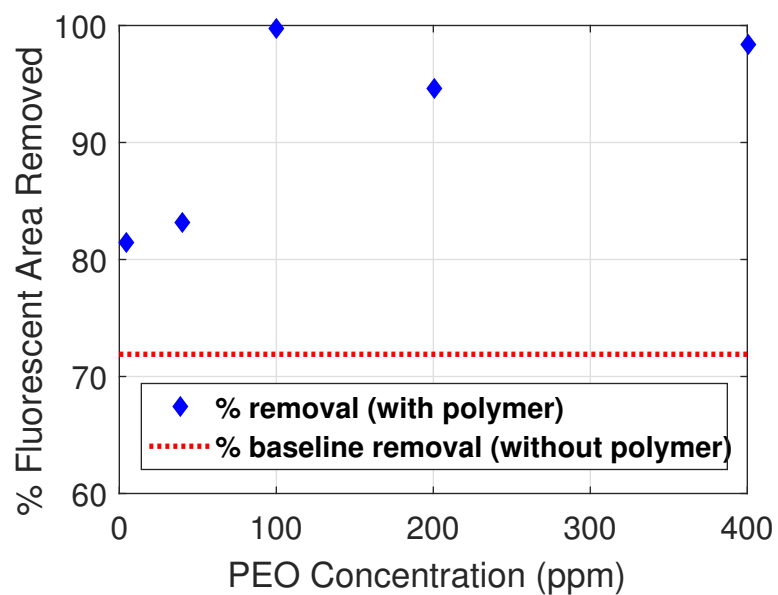


Figure 1.1: Enhanced particle removal (EPR) of $1\ \mu\text{m}$ fluorescent SiO_2 particles from the surface of silicon wafers at varying concentrations of poly(ethylene oxide) (PEO) ($\text{MW} = 7 \times 10^6$). Concentrations were selected to be below the coil overlap concentration, c^* , calculated using the Mark-Houwink-Sakurada for PEO in deionized water (DIW). Data courtesy of R. K. Cashen.

1.3 Background

1.3.1 Dilute Polymer Solutions

To define “dilute,” the concept of the coil overlap concentration will first be presented. The coil overlap concentration (c^*) describes the concentration in which polymers in their equilibrium, coiled conformations begin to overlap. When any additional polymer is introduced into a given system, polymer/polymer interactions begin to form. Factors influencing c^* include the polymer type, molecular weight, and solvent quality, as well as the temperature of the system.

A linear idealized polymer chain is depicted in Figure 1.2, occupying a spherical volume with a radius of gyration, R_g . At concentrations below c^* , the individual polymer chains do not interact, and they are thought not to “see” one another, taking random conformations in the solvent. Consequently, only polymer/solvent interactions are considered important. As polymer is added, the polymer chains collapse to minimize contact with the other chains. Eventually, enough polymer is added so that the coils begin to overlap. The critical overlap concentration can thus be thought as the concentration in which the volume of a single coil times the number density of coils is equal to one.

At concentrations above c^* , polymer molecules become highly entangled, and these entanglements dominate the resulting flow properties of the solution. From a plot of the zero-shear viscosity versus concentration of polymer, a significant increase in shear viscosity is often observed when transitioning into this regime. For the present work, dilute concentrations are defined as concentrations below c^* , where the viscoelastic properties of a fluid are determined by the behavior of a single polymer molecule [18, 19]. Nevertheless, even at “dilute” concentrations, polymer/polymer interactions can still occur when polymer chains deviate from their equilibrium conformations [20].

A common approach for evaluating c^* is to use the following approximation for flexible

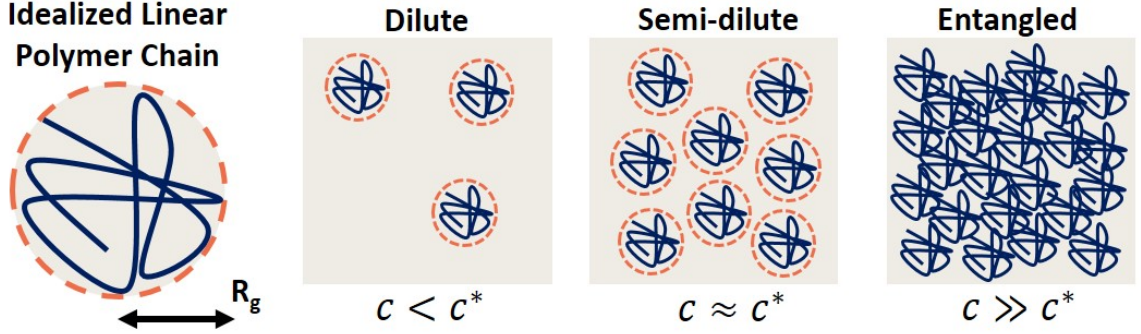


Figure 1.2: A series of images describing polymer/solvent and polymer/polymer interactions based on the concentration of polymer in a given solvent. On the left, an idealized linear polymer occupies a volume of radius, R_g , that depends on the molecular weight of the polymer, solvent quality, and temperature of the system. The remaining images depict systems containing multiple polymer chains, described by the critical overlap concentration, c^* , adapted from [1]. The three regimes include dilute ($c < c^*$), semi-dilute ($c \approx c^*$), and entangled ($c \gg c^*$) polymer solutions.

polymer solutions:

$$c^* \approx \frac{1}{[\eta]}. \quad (1.1)$$

This relationship results in values of c^* that are slightly greater than the values determined using the relationship presented by Graessley, where $c^* = \frac{0.77}{[\eta]}$ [21]. Here, $[\eta]$ is the intrinsic steady-state shear viscosity with units of cm^3/g . The intrinsic viscosity is a measure of the polymer's contribution to the overall solution viscosity. Experimentally, $[\eta]$ can be determined using a capillary viscometer by plotting measurements of the reduced or relative viscosities over a range of concentrations, where $[\eta]$ is found by taking the limit as the concentration of polymer goes to zero, according to the Huggins and Kraemer equations [1].

Yet, if the necessary parameters are known, $[\eta]$, and thus c^* , can more simply be approximated using the well-known Mark-Houwink-Sakurada equation (MHS)

$$[\eta] = K[M_v]^a. \quad (1.2)$$

The MHS equation was developed from solution-viscosity measurements for monodisperse

polymers and relates the intrinsic viscosity to a polymer's molecular weight [19]. The parameters K and a depend on the polymer/solvent system, where a is a descriptor of the solvent quality. For polymers that behave as random coils, a ranges from 0.5 (for a theta solvent) to 0.8 (for a good solvent) [19]. In a theta solvent, a polymer molecule experiences enough of a repulsive interaction towards the solvent that the repulsive excluded-volume interaction between chain segments are canceled [22]. The term M_v is the viscosity-average molecular weight of the polymer. Since the viscosity-average molecular weight is difficult to obtain, the weight-average molecular weight, M_w , of polymer with a narrow-molecular-weight distributions is often used [7]. Knowing the molecular weight of the polymer and using tabulated values of K and a , one can approximate $[\eta]$ and thus the value of c^* using Equations 1.1 and 1.2.

Calculating c^* for the Present Work: For the present work, DOW Chemical POLYOXTM Water-Soluble Resin WSR-303 NF (MW $\approx 7 \times 10^6$ g/mol) was used to make test solutions. To approximate the coil overlap concentration, two approaches were taken. First, the parameters for K and a were found using the Polymer Handbook [7] for poly(ethylene oxide) in water. The information gathered is provided in Table 1.1. Using Equations 1.1 and 1.2 with the data for a 7×10^6 g/mol PEO powder, c^* was evaluated to be approximately 3.8×10^{-4} g/cm³ for a solution at 35°C. Because solutions were made and experiments were performed at room temperature ($\approx 25^\circ\text{C}$), this value for c^* served only as a rough estimate of the actual overlap concentration.

Table 1.1: Mark-Houwink-Sakurada data for poly(ethylene oxide) in water adapted from the Polymer Handbook [7].

Temp (°C)	MW (g/mol)	K (cm ³ /g)	a
25	$(0.019 - 0.1) \times 10^4$	0.156	0.50
30	$(2 - 500) \times 10^4$	0.0125	0.78
35	$(0.04-0.4) \times 10^4$	0.0166	0.82
35	$(3 - 700) \times 10^4$	0.0064	0.82

Additionally, for PEO solutions in water and glycerol/water mixtures, an alternative MHS equation,

$$[\eta] = 0.072M_w^{0.65}, \quad (1.3)$$

was determined by Tirtaatmadja et al. [23] by fitting results collected by a number of researchers for water and glycerol/water mixtures over a range of molecular weights. This equation has been used throughout the literature for studies involving poly(ethylene oxide) in water or in glycerol/water mixtures [23–25]. Using Equation 1.3 to evaluate c^* , the resulting value was found to be $4.9 \times 10^{-4} \text{ g/cm}^3$, approximately 30% greater than the previously calculated value. Thus, the solutions that are made could be considered more or less concentrated depending on how c^* is evaluated. When comparing values of c^* in the literature, knowing the values for K and a as well as how these parameters were determined is important.

A polymer solution’s response to a given deformation is strongly dependent on the interactions (or non-interactions) between the individual polymers in solution and, thus, on the solution’s concentration regime (dilute, semi-dilute, and concentrated). In industry, at low concentrations below c^* , solutions are often modeled as Newtonian and considered as having similar flow properties as water. As evidenced in EPR experiments (Figure 1.1), however, solutions with small amounts of macromolecule added to solvent can still perform or respond differently than the solvent alone.

To have a better understanding of the molecular dynamics within a given system, characterization of a fluid’s viscoelastic behavior is useful. Viscoelastic fluids have characteristic relaxation times that reflect the amount of elasticity present in their microstructure. Sometimes referred to as a “memory time,” relaxation times are an intrinsic property that describe the time required for a material to return to a previous state after a small disturbance has been applied. Depending on the concentration and type of polymer in a given system,

the relaxation process may involve different restoring mechanisms. For the relaxation of simple Newtonian fluids, for example, the relaxation time scales are related to molecular self-diffusion. For fluids such as water, such time scales are on the order of 10^{-13} to 10^{-12} s and are only relevant at large velocity gradients that are rarely achieved in natural or designed systems [26, 27]. In terms of fluids containing long flexible polymers, however, applied flows are more capable of altering the local microstructure, and they can cause the time scales of the stress relaxation to be significantly longer.

For dilute polymer solutions, the total solution relaxation time is proportional to the relaxation time of a single polymer molecule [28]. Although the polymer may have multiple mechanisms of relaxing, a longest relaxation time is often used to describe the magnitude of the overall process. The longest relaxation time in Zimm theory can be approximated by

$$\lambda_Z \cong \frac{[\eta]M_w\eta_s}{\zeta(3\nu)N_Ak_B T}, \quad (1.4)$$

such that η_s is the solvent viscosity, N_A is Avogadro's number, k_B is the Boltzmann constant, and $[\zeta(3\nu)]^{-1}$ is a coefficient that depends on the solvent/solute system [23, 29]. This coefficient corrects for hydrodynamic interactions and can be evaluated as $[\zeta(3\nu)]^{-1} = \sum_{i=1}^{\infty} i^{-3\nu}$, where ν is the Flory exponent that describes the excluded volume of a polymer chain [1, 22]. Zimm theory describes the hydrodynamic interactions between the solvent and the beads of a Gaussian chain, and it is often used as a comparison for describing the relaxation times of dilute polymer solutions [20, 24]. Here, the Gaussian chain serves as a statistical representation of a randomly-coiled polymer in solvent [18]. A review of polymer statistical mechanics is presented by Yamakawa [30].

The Zimm relaxation time can be determined if the polymer's molecular weight and solvent shear viscosity are known. From the scaling of the radius of gyration with molecular weight for PEO in water and glycerol/water mixtures, ν has been experimentally determined to be 0.55 [23]. Thus, for the present work, for a dilute PEO solution with a molecular

weight of approximately 7×10^6 in water (1 mPa·a) at room temperature (25°C), the Zimm relaxation time is estimated to be approximately 2.6 ms. Thus, for small deformations of the PEO solutions studied herein, we may expect the reported relaxation times to be near this value. At large deformations, however, other characteristic times may be observed that deviate from the Zimm relaxation time [20], and they will be discussed in the present manuscript.

A summary of predicted scaling laws in dilute solutions for chains with dominant hydrodynamic interactions have been presented by de Gennes [8] as well as by Larson et al. [9], and it is presented in Table 1.2.

Table 1.2: A summary of predicted scaling laws for dilute polymer solutions with dominant hydrodynamic interactions [8,9]. M is the molecular weight of a polymer chain and ν is the Flory exponent.

	Theta Solvent $\nu = 0.5$	Gaussian Chain $\nu = 0.6$
Relaxation time, λ $\lambda \sim M^{3\nu}$	$M^{3/2}$	$M^{9/5}$
Intrinsic viscosity, $[\eta]$ $[\eta] \sim M^{3\nu-1}$	$M^{1/2}$	$M^{4/5}$

1.3.2 Extensional Rheology

To select an appropriate characterization technique for a particular fluid, knowing how the fluid will be processed is essential. Two important considerations when collecting rheological information are the length scales and predominant modes of deformation governing a given application. In turbulent drag flow reduction (TDR) and enhanced particle removal (EPR), the predominant mode of deformation is extensional, and the length scales are on the order of a few microns or less. The present work is thus interested in exploring extensional rheological techniques. After reviewing the basic principles of extensional rheology and a number of previously described techniques on the macro-scale and after reviewing important

dimensionless parameters for such processes, micro-scale devices will be considered.

Overview of Extensional Rheology Rheometry is a term that is often used interchangeably with shear characterization. Shear flows are the simplest flow fields to reproduce in a laboratory setting, and they are the basis for standard viscometers and rotational rheometers. Shear flows, however, are a combination of two fundamental types of flow – vortical (rotational) and elongational (extensional), and a fluid’s response can differ depending on flow type.

For example, if a high-molecular-weight polymer is added to solvent, and the solution is subjected to a purely extensional flow, similar to stretching a rubber band, the polymer will quickly resist any additional deformation as it is unraveled. In a shear flow, however, the rotation of the polymer away from the principle axis of stretching will reduce the buildup of stress in the fluid as it is strained, relative to if it was stretched in pure extension, as it is strained. Extensional flows can generate significant alignment of species along the flow direction, inducing microstructural changes and increasing the total drag acting on the polymer chains. Thus, the extensional viscosity (η_E), or resistance to an extensional deformation, of a fluid can be orders of magnitude larger than values found in shear (η).

The Trouton ratio (Tr) is a dimensionless parameter that is defined as the ratio of extensional viscosity to shear viscosity. For Newtonian fluids in uniaxial extension, the extensional viscosity can mathematically be proven to be three times the shear viscosity ($Tr = 3$). This value of the Trouton ratio holds true for polymer solutions and melts at small deformations and deformation rates. Extensional thickening, however, can occur at high strains and strain rates, where the extensional viscosity increases, and the shear viscosity decreases relative to their linear-viscoelastic results ($Tr \gg 3$).

Extensional thickening has been used to describe phenomena ranging from the load-dampening properties of synovial fluid in our knee joints [31] to the effect of surfactants on enhanced oil recovery processes [32]. Despite decades of research, no reliable correlations

exist between nonlinear-viscoelastic behavior in extension and in shear [28]. Therefore, for the complete characterization of a complex fluid, considering both shear and extensional properties is important. Nevertheless, extensional measurements are challenging to perform, particularly for more mobile (less viscous) polymer solutions. Such obstacles include imposing a constant strain history and strain rate on the material and ensuring a completely shear-free flow.

Significant research has been devoted to improving old and developing new extensional rheological techniques, and significant efforts have been made to extend the range of fluids that can be characterized. Several reviews of extensional rheological techniques have been written for polymer melts [33–35] and for weakly-viscoelastic solutions [36–38]. For simplicity, we will consider techniques that are applicable for dilute and semi-dilute polymer solutions having lower shear viscosities (Table 1.3).

Many of the techniques discussed in the present work assume uniaxial extension (Figure 1.3), where a fluid is stretched in one direction and, to ensure incompressibility ($\nabla \cdot v = 0$), compressed in the other two. For visualization, imagine stretching dough to make noodles. As the dough is stretched, the resulting noodles will thin. Here, the strain rate ($\dot{\epsilon}$) is defined as

$$\dot{\epsilon}(t) = \frac{1}{L} \frac{dL}{dt} = -\frac{2}{D} \frac{dD}{dt}, \quad (1.5)$$

such that L is the length of a cylindrical fluid element at time t . Assuming a constant volume ($V = \pi DL$), the strain rate can be rewritten in terms of the fluid’s diameter. Integrating to solve for the amount of strain that has been applied, the Hencky strain is defined as

$$\epsilon(t) = 2 \log \left[\frac{D_0}{D(t)} \right], \quad (1.6)$$

such that D_0 is the initial diameter of the filament. To apply a constant strain rate in uniaxial extension, the length of the filament must grow, and the diameter must decay exponentially. The stress involved in uniaxially stretching a fluid is the first normal stress

Table 1.3: Comparison of extensional rheological techniques for mobile polymer solutions.

Method	Advantages	Disadvantages	Citation
Filament Stretching Rheometry (FISER)	<ul style="list-style-type: none"> • imposes constant strain rates • monitors both the diameter decay and the axial force 	<ul style="list-style-type: none"> • requires higher shear viscosity samples 	[39, 40]
Capillary Breakup Extensional Rheometer (CaBER)	<ul style="list-style-type: none"> • is capable of testing lower viscosity samples • is relatively well understood on the macro-scale 	<ul style="list-style-type: none"> • applies a finite step-strain • is hindered by gravitational and edge effects • cannot control strain rate 	[41, 42]
Dripping onto Substrate (DoS)	<ul style="list-style-type: none"> • is similar to the CaBER • does not involve a finite step strain 	<ul style="list-style-type: none"> • requires a wettable substrate • involves an external forcing that may impact measurements 	[3, 43]
Opposed-Jet Device (RFX)	<ul style="list-style-type: none"> • was developed for low-viscosity fluids • has been used to measure fluids with shear-viscosities approaching that of water 	<ul style="list-style-type: none"> • requires large deformation rates to induce significant viscoelastic effects • is hindered by inertial effects that can dominate over viscoelastic effects • requires large sample volumes 	[36, 44–46]
Rayleigh-Ohnesorge Jetting Extensional Rheometry (ROJER)	<ul style="list-style-type: none"> • does not require a finite step-strain • makes use of the capillary breakup of jets which is well described in the literature 	<ul style="list-style-type: none"> • requires a complex set-up with a spatiotemporally evolving jet 	[47–49]
Optimized Cross-Slot (OSCER)	<ul style="list-style-type: none"> • makes use of micron length scales for applying a constant strain rate 	<ul style="list-style-type: none"> • has a limited range of operability • requires complicated optical techniques such as birefringence 	[4, 38]
Plateau-Rayleigh Instability Microfluidic Extensional Rheometer (PRIMER)	<ul style="list-style-type: none"> • makes use of micron length scales • does not require complicated optical techniques • does not require samples to be exposed to air 	<ul style="list-style-type: none"> • is still being developed 	[50]

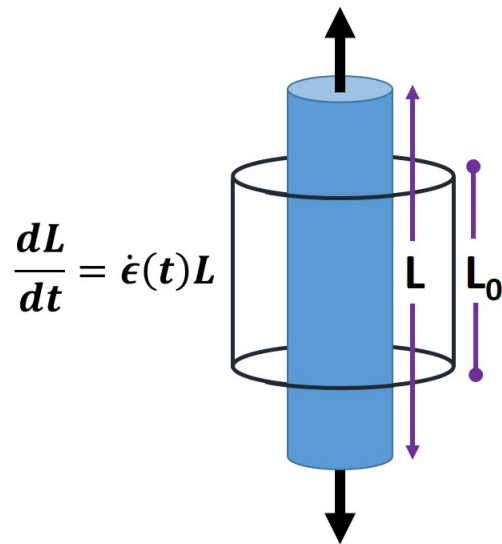


Figure 1.3: Uniaxial extension of a cylindrical filament of initial length L_0 . The fluid is being stretched at a rate $\frac{dL}{dt}$. To maintain a constant strain rate, the length of the filament, L , must grow exponentially in time ($L = L_0 \exp[\dot{\epsilon}t]$).

difference $[T_{zz} - T_{rr}]$, and the transient extensional viscosity can be defined as

$$\eta_E^+(\dot{\epsilon}, \epsilon, t) = \frac{T_{zz} - T_{rr}}{\dot{\epsilon}}. \quad (1.7)$$

At late times, in the nonlinear regime of an extensional flow, one may arrive at a steady-state extensional viscosity (η_E). In most (if not all) processing environments, approaching this plateau is unrealistic. During processing, extensional flows generally do not last long enough for a steady state to be reached. Plots of the transient extensional viscosity versus Hencky strain are thus more useful [51].

Capillary Breakup Extensional Rheometry For assessing the extensional properties of less-viscous polymer solutions, samples are often measured using the commercially available capillary breakup extensional rheometer (CaBERTM). Capillary breakup extensional rheometry (CaBER) is a form of filament stretching rheometry that emerged from the fil-

ament stretching extensional rheometer (FISER), which was used for polymer melts and more viscous samples [40, 52, 53]. The FISER operates by stretching a fluid at a constant stress or strain rate and monitoring the diameter of the filament and the axial force as the sample is stretched. A drawback of the FISER, however, is that it cannot be used on more mobile (less viscous) polymer solutions as a result of the rapid breakup of such filaments. In identifying differences in sample thinning in the late stages of FISER experiments, the CABER technique was born [39–41, 52].

Capillary breakup extensional rheometry works by applying a step-strain to a sample to form an unstable filament that thins and subsequently breaks under the action of capillary forces. The breakup process is monitored using either a laser micrometer and/or a high-speed camera at the filament’s mid-point. From the diameter decay profile, information can be gained on the presence of elasticity and the material properties of a given sample.

The experimental and theoretical work behind capillary breakup extensional rheometry will be discussed in later chapters of this thesis. Ultimately, the literature describes an interplay between inertial, viscous, elastic, and capillary forces during the thinning and breakup event [42]. The stress balance describing the decay profile for an idealized cylindrical filament with a radius independent of the z -coordinate is given in as

$$3\eta_s \left(\frac{-2}{D(t)} \frac{dD(t)}{dt} \right) + [\tau_{zz} - \tau_{rr}] + \frac{2\sigma}{D(t)} = \frac{4F_z}{\pi D^2(t)} \quad (1.8)$$

such that η_s is the viscosity of the Newtonian solvent, σ is the interfacial tension of the sample, $[\tau_{zz} - \tau_{rr}]$ is the polymeric contribution to the normal-stress difference that depends on the constitutive model chosen, and F_z is the tensile force acting on the sample ends. The term in parenthesis on the left of Equation 1.8 is the strain rate presented in Equation 1.5. Depending on the dominating physics in the capillary-breakup process, Equation 1.8 can be simplified.

Dimensionless Groups for Free Surface Flows Before continuing, a discussion of the relevant dimensionless parameters for the current thesis is warranted. The use of dimensional analysis is helpful for understanding processing operations involving free-surface deformations. A useful resource for performing dimensional analysis is provided by Bridgeman [54]. Furthermore, McKinley [2, 42] provides a helpful overview of the dimensionless groups relevant for free surface flows.

As previously discussed, flows involving viscoelastic samples can involve competing capillary, viscous, inertial, and elastic effects, where the dominant balance of forces depends on the relative magnitude of such contributions for a given process. In the analysis provided by McKinley [2, 42], the parameter space depends on three main parameters that describe the size of the capillary, inertial, and elastic effects relative to the viscous stresses for a given processing environment. These parameters are the capillary number,

$$Ca = \frac{\eta_0 U}{\sigma}, \quad (1.9)$$

Reynolds number

$$Re = \frac{\rho U l}{\eta_0}, \quad (1.10)$$

and Weissenberg number

$$Wi = \frac{\lambda U}{l}, \quad (1.11)$$

respectively (Figure 1.4). Here, U and l are the characteristic velocity and length scales of interest, ρ is the density, η_0 is the zero-shear viscosity, σ is the surface tension, and λ is the characteristic relaxation time of the fluid.

Collectively, these parameters define the three-dimensional operating space in Figure 1.4. For bulk flows of viscoelastic fluids, the Reynolds and Weissenberg numbers are compared to describe the relative importance of inertial and elastic stresses. The ratio of these two

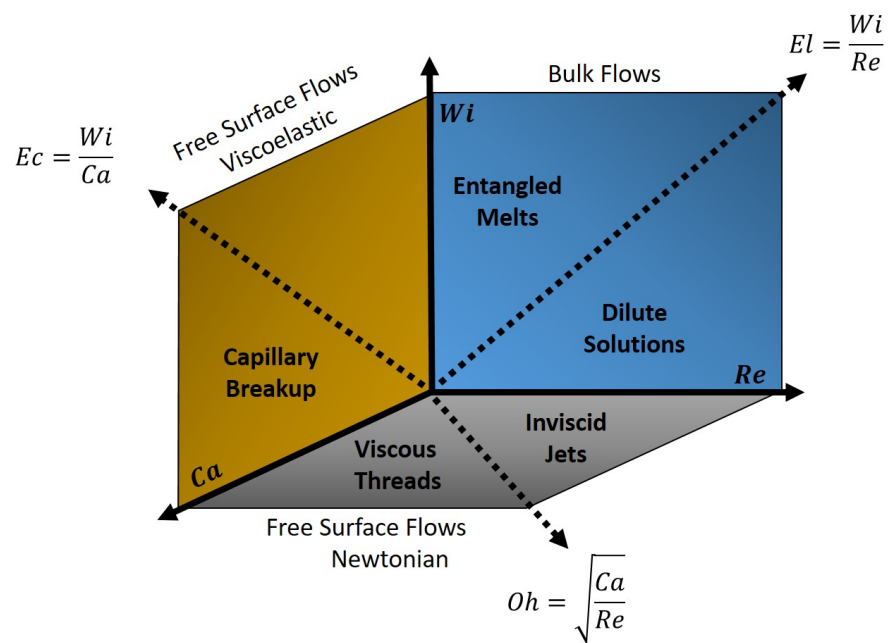


Figure 1.4: Parameter space characterizing free surface flows of viscoelastic fluids, adapted from [2]. The parameter space is dependent on parameters the capillary, Reynolds, and Weissenberg numbers to describe the relative capillary, inertial, and elastic contributions to the flow. From these parameters, the elastocapillary, elasticity, and Ohnesorge numbers can be evaluated.

parameters forms a new dimensionless group such that

$$El \equiv \frac{Wi}{Re} = \frac{\eta_0 \lambda}{\rho l^2}, \quad (1.12)$$

and this new group is often referred to as the elasticity number, El [55]. The elasticity number depends only on the fluid properties and the geometry of the processing system. In general, when the elasticity number is much greater than unity ($El \gg 1$), such as during the extrusion of a polymer melt for 3D printing, significant elastic effects are observed.

Similarly, comparing the Reynolds and capillary numbers, free surface flows of Newtonian fluids are characterized by the Ohnesorge number (Oh) as follows

$$Oh^{-2} \equiv \frac{Re}{Ca} = \frac{\rho \sigma l}{\eta_0^2}. \quad (1.13)$$

First identified by von Ohnesorge [56], this number is used in parameterizing operations involving viscous threads or inviscid jets. Although important, the current study focuses on the relevant dimensionless groups for non-Newtonian fluids.

Describing flows of viscoelastic fluids where inertial effects are negligible, an elastocapillary number can be defined as

$$Ec \equiv \frac{Wi}{Ca} = \frac{\lambda \sigma}{\eta_0 l}, \quad (1.14)$$

such that elastic and capillary stresses are compared with viscous stresses.

As discussed by McKinley [2], the space presented in Figure 1.4 can be used to describe general free surface flows. Note that the parameters that are discussed involve the flow velocity in the system. For flows that describe “self-thinning” processes, such as the capillary thinning and breakup of cylindrical filaments, one may consider a different set of dimensionless parameters not dependent on velocity. For this case, three important time scales are considered that describe the relevant viscous, inertial, and polymeric contributions to the thinning dynamics.

Most intuitively, the elastic time scale is the time scale associated with the longest relaxation time of polymer in solution (λ). Requiring more thought, however, are the viscous and inertial time scales associated with a capillary-breakup event. For a filament, the viscous time scale is the critical time scale to breakup during the viscocapillary thinning process previously discussed, where the viscous-breakup time (t_{vb}) is evaluated using Equation 1.23,

$$t_{vb} = 7.1 \frac{\eta_0 D_0}{\sigma}. \quad (1.15)$$

Additionally, the Rayleigh time scale describing the breakup of an inviscid jet can be used to express the magnitude of inertial effects in the system,

$$t_R = \left[\frac{\rho D_0^3}{8\sigma} \right]^{1/2} \quad [57]. \quad (1.16)$$

For the capillary breakup of an inviscid thread, the similarity solution takes the form

$$t_{ib} = (0.64^{-3/2}) \left[\frac{\rho D_0^3}{8\sigma} \right]^{1/2} = 1.95 t_R \quad [58]. \quad (1.17)$$

These time scales are mapped in Figure 1.5.

In the parameter space presented, the Ohnesorge number again arises. An additional numerical factor describes the similarity solutions for viscocapillary and inertiocapillary thinning and breakup, $t_{vb}/t_{ib} = (7.23) Oh$ [25]. To define a low-viscosity fluid in capillary breakup experiments, the viscous time scale should be less than the inertial time scale, $t_{vb} < t_{ib}$ or $Oh < [7.23]^{-1}$. Additionally, a second dimensionless parameter arises when comparing the time scale for stress relaxation to the Rayleigh time scale presented above. This time scale is often described as an ‘‘intrinsic’’ Deborah number for free-surface viscoelastic flows and is defined as follows

$$De_{int} = \frac{\lambda}{t_R} = \lambda \left[\frac{\sigma}{\rho \ell^3} \right]^{1/2}. \quad (1.18)$$

The parameter space in Figure 1.5 characterizes capillary self-thinning of viscoelastic

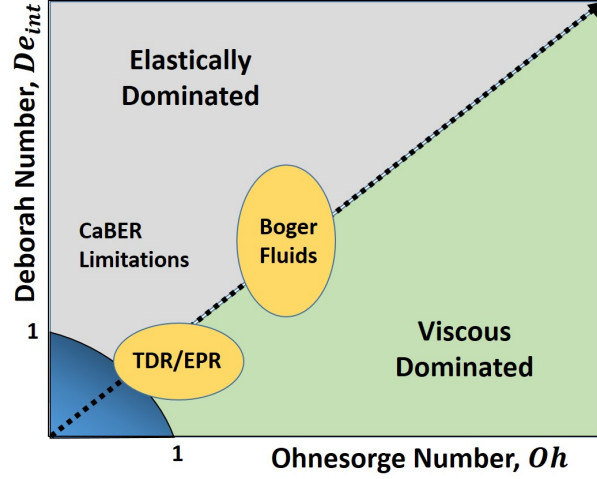


Figure 1.5: Parameter space characterizing capillary self-thinning of viscoelastic filaments using viscous, inertial, and elastic time scales describing a breakup event adapted from [2]. The limitations for the CaBER are plotted, below which measurements cannot be taken. The locations for fluids studied in EPR and TDR are sketched as well as the locations for Boger fluids. The dashed-arrow represents where the elastocapillary number is unity, $Ec = 1$.

filaments. The parameter space for fluids studied in EPR and TDR are noted as well as the parameter space for Boger fluids. Additionally, the limitations for the CaBER are plotted, below which measurements cannot be taken [25]. Fluids must be sufficiently viscous or elastic to resist the capillary-driven necking. CaBER limitations will be discussed in more detail in the next section. In general, less-viscous fluids must be more elastic, and weakly-elastic fluids must be more viscous. When inertial effects are negligible, the dynamics of thinning can be described by balancing the viscous and elastic time scales, t_{vb} and λ . Here, the elastocapillary number resurfaces such that

$$Ec = \frac{De}{Oh} \approx \frac{\lambda}{t_{vb}} = 0.14 \frac{\lambda\sigma}{\eta_0 l}. \quad (1.19)$$

Figure 1.5 depicts the line $Ec = 1$, indicating where the thinning and breakup event transitions from elastically dominated to viscous dominated.

Now that an overview of the relevant physics in the capillary-breakup process has been

presented, simplifications to Equation 1.8 will be used to solve for the diameter-decay profiles of the viscopillary and elastocapillary thinning of a filament.

Viscopillary Balance For more viscous fluids, at early times in the filament-thinning and breakup process, when elastic contributions are negligible (and inertial effects are assumed negligible), a viscopillary balance can be achieved, and Equation 1.8 can be simplified as

$$3\eta_s \dot{\epsilon} + \frac{2\sigma}{D(t)} = \frac{4F_z}{\pi D^2(t)}. \quad (1.20)$$

To include the potential for curvature along the filament, a correlation factor

$$\chi(t) = \frac{F_z(t)}{\pi\sigma D(t)}, \quad (1.21)$$

can be introduced into Equation 1.20 to yield the relationship

$$3\eta_s \dot{\epsilon} = (4\chi(t) - 2) \frac{\sigma}{D(t)}. \quad (1.22)$$

Integrating this expression, the diameter decay profile in the viscopillary regime can be described by

$$D(t) = D_0 - \frac{(2\chi - 1)\sigma}{3\eta_s} t. \quad (1.23)$$

Here, the diameter of the filament decays linearly in time at a rate that is inversely proportional to the solvent viscosity. Thus, for a viscous Newtonian fluid, one could easily predict the time (t_{vb}) for a cylindrical filament to break, where $D(t_{vb}) = 0$.

The breakup of slender columns of viscous Newtonian fluids have been described extensively in the literature [52, 57, 59–64]. Although earlier studies have not accounted for the axial curvature of the filament, more recent studies by Tripathi and McKinley [52] have demonstrated good agreement with experimental data by incorporating the factor $\chi(t)$. In assuming a perfectly-cylindrical filament, earlier solutions assumed that the net longitudinal

stress in the filament was zero and that $\chi(t) = 1$. Accounting for curvature, the similarity solution determined numerically by Papageorgiou [62] revealed that $\chi(t)$ converges to a constant, $\chi = 0.7127$.

Elastocapillary Balance For viscoelastic samples, at middle times in the capillary thinning and breakup process, as elastic stresses grow to compete with the capillary pressures driving the breakup event, the stress balance in Equation 1.8 can again be simplified. Two cases will be presented in the current section. The first case originates from the theory provided by Entov and Hinch [65] and assumes that the filament is uniform along the length of the cylinder and that axial stresses are negligible. The second case, describing the analytical solution provided by Clansen et al. [66], relaxes these assumptions.

For the first scenario, the viscous and axial stress terms vanish, and the resulting force balance simplifies to

$$[\tau_{zz} - \tau_{rr}] = -\frac{2\sigma}{D(t)}. \quad (1.24)$$

Similar to the analysis performed for the viscocapillary balance, the resulting filament decay profile can be evaluated. Since the polymeric contribution to the stress in Equation 1.24 is non-negligible, a constitutive model must be assumed. For the present work, we limit our focus to models representative of dilute polymer solutions. The use of non-interacting dumbbells satisfies this condition.

In the finitely-extensible-nonlinear-elastic model (FENE), derived from molecular theories, long-chained polymers are represented as a sequence of beads connected by nonlinear springs. Entov and Hinch's process for evaluating the elastocapillary thinning of a cylindrical filament used this model to describe the capillary breakup of dilute polymer systems [65]. In a purely extensional flow the axial deformation A_{zz} and radial deformation A_{rr} for the polymer satisfy

$$\dot{A}_{zz} = 2\dot{\epsilon}A_{zz} - \frac{f}{\lambda}(A_{zz} - 1), \text{ and} \quad (1.25)$$

$$\dot{A}_{rr} = -\dot{\epsilon}A_{rr} - \frac{f}{\lambda}(A_{rr} - 1). \quad (1.26)$$

Here, λ is the relaxation time, and f is the FENE factor,

$$f = \frac{L^2}{L^2 + 3 - A_{zz} - 2A_{rr}}, \quad (1.27)$$

which describes the finite extensibility of the polymer such that L^2 is the finite extension limit. The polymeric stress term becomes

$$[\tau_{zz} - \tau_{rr}] = fG(\dot{A}_{zz} - \dot{A}_{rr}) \quad (1.28)$$

such that G is the shear elastic modulus of the dilute suspension of dumbbells [65].

At middle times in the decay of a viscoelastic filament, the deformation of the polymer is smaller than the finite extension limit so that the finite extensibility is approximately one, $f = 1$. Additionally, if the elastic deformation is large, the deformation in the axial direction is greater than in the radial direction, $A_{zz} \gg 1 > A_{rr}$. Equations 1.25 and 1.26 simplify to

$$\dot{A}_{zz} = 2\dot{\epsilon}A_{zz} - \frac{1}{\lambda}A_{zz}. \quad (1.29)$$

Recalling the extensional strain rate in Equation 1.5, the analytical solution for the axial deformation A_{zz} can be evaluated as

$$A_{zz} = \left[\frac{D_1}{D(t)} \right]^4 \exp \left[\frac{-t}{\lambda} \right], \quad (1.30)$$

assuming that the initial deformation of the filament is unity, $A_{zz}(0) = 1$ for an undeformed material and that the relaxation term is small during the initial viscous period. Introducing Equation 1.30 into the polymeric stress term in Equation 1.28 and solving Equation 1.24,

the decay profile for a FENE fluid with non-interacting dumbbells can be described by

$$D(t) = D_1 \left[\frac{GD_1}{2\sigma} \right]^{\frac{1}{3}} \exp \left[-\frac{t}{3\lambda} \right]. \quad (1.31)$$

Thus, in the elastocapillary regime, the filament decay for noninteracting dumbbells was numerically determined by Entov and Hinch to be exponential. Such results are in agreement with several experiments performed in the literature, and they are the basis for the CaBER [39, 67].

For the second scenario presented by Clansen et al. [66], the viscous term again vanishes, and the axial stress term remains in the simplified force balance,

$$[\tau_{zz} - \tau_{rr}] = \frac{4F_z}{\pi D^2(t)} - \frac{2\sigma}{D(t)}. \quad (1.32)$$

Similar to the viscopillary breakup, the correlation factor in Equation 1.21 can be introduced into Equation 1.32 to yield the relationship

$$[\tau_{zz} - \tau_{rr}] = \left(4\chi(t) - 2 \right) \frac{\sigma}{D(t)}. \quad (1.33)$$

Clansen et al. numerically evaluated χ to have a value of 0.48 [66]. Again, for a FENE fluid with non-interacting dumbbells, the decay profile can be described by

$$D(t) = D_0 \left[\frac{GD_1}{4\sigma} \right]^{\frac{1}{3}} \exp \left[-\frac{t}{3\lambda_E} \right]. \quad (1.34)$$

The above result is a factor of $2^{1/3}$ smaller than the result given in Equation 1.31 and impacts the projected breakup time of the filament. Nevertheless, this result does not impact the relaxation time extracted from the filament decay profile.

When Equations 1.31 and 1.34 are compared with uniaxial extension at a constant strain

rate,

$$D(t) = D_0 \exp \left[-\frac{\dot{\epsilon}}{2} t \right], \quad (1.35)$$

the Weissenberg number describing relative viscous and elastic forces can be evaluated as a constant such that

$$Wi = \lambda_E \dot{\epsilon} = 2/3. \quad (1.36)$$

This value is above the critical value, $Wi_c = 1/2$, where individual polymer chains are known to be significantly strained from their equilibrium conformations and undergo coil-stretch transitions [65, 68, 69]. Thus, from the capillary breakup of a liquid filament, both the characteristic relaxation time and strain rate can be extracted.

Recently, a FENE-P model was used to study the dynamics of the capillary thinning of viscoelastic filaments to derive a composite analytical solution for predicting the evolution of a filament in time [70]. The thinning and breakup in such simulations agree with previous numerical solutions presented in the literature, yet they give a better approximation for the time until breakup of the filament.

Comparison of CaBER Results Figure 1.6 compares evolution profiles in CaBER experiments for Newtonian and viscoelastic fluids of similar zero-shear viscosities. In the figure, the normalized diameter is plotted versus time. Here, the diameter is normalized by the initial diameter of the filament upon completion of the initial step-strain. From these general profiles, the Newtonian filament is shown to break quickly relative to the viscoelastic sample, whereas the additional stresses in the viscoelastic sample tend to extend the lifetime of the filament. Furthermore, the Newtonian profile is linear, whereas the profile for the viscoelastic fluid is exponential. By fitting the data in Figure 1.6 with Equations 1.23 and 1.34, the material properties of the fluids can be evaluated. For the Newtonian fluid, if the surface tension is known, the solvent viscosity can be evaluated. For the viscoelastic sample, a characteristic relaxation time can be extracted. In addition to these material

parameters, extracting the final time of breakup is also possible. Although relevant to the current thesis, this topic will not be discussed in detail.

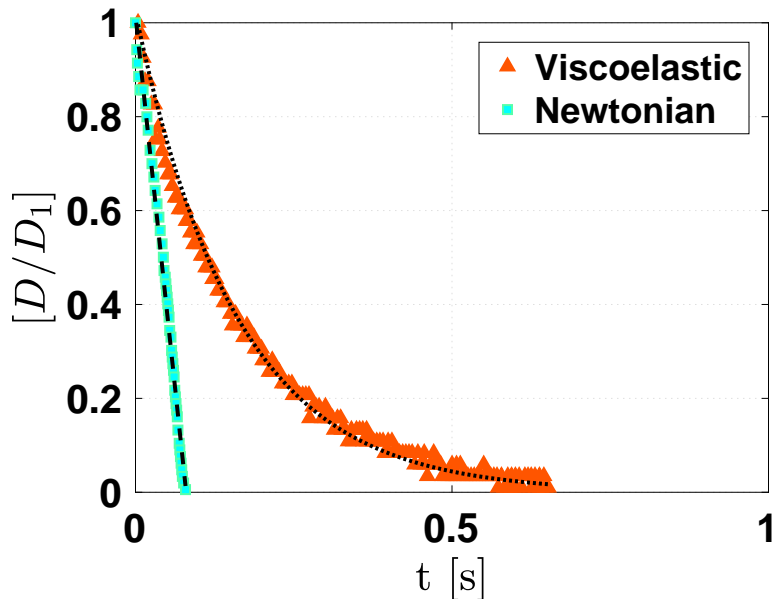


Figure 1.6: Representative CaBER data for Newtonian and viscoelastic fluids. The diameter is normalized by the diameter of the filament after the initial step-strain, D_1 . The black-dashed line represents the linear (Newtonian) fit and the black-dotted line represents the exponential (viscoelastic) fit of the data according to Equations 1.23 and 1.34, respectively.

1.3.3 Challenges in Characterizing Weak Viscoelasticity

In the previous section, a number of dimensionless groups were presented that help to describe the dominating physics for a given flow process. Over the past 20 years, interest has grown in the ability to characterize fluids having weak viscoelasticity. For example, studies have explored low-viscosity elastic fluids ($De > 1 > Oh$), where viscous effects are negligible [24,25,36,37]. Furthermore, several studies have focused on both low-viscosity and weakly-elastic fluids. These properties are desirable in applications such as inkjet-printing, where polymer may be added to minimize the onset of inertially-induced satellite droplets,

yet they are added in small enough quantities to keep elastic effects to a minimum [71,72]. For low-viscosity and weakly-elastic fluids, however, inertial effects often dominate the non-Newtonian stresses in the fluid, making it challenging to characterize the fluid's material properties [73].

Challenges in Characterizing Weak Viscoelasticity in Shear In traditional oscillatory shear tests, shear relaxation times are approximated as the inverse of the frequency at which the storage modulus (G') begins to dominate over the loss modulus (G'') or when elastic effects begin to dominate over viscous effects (Figure 1.7). When the relaxation time is small (indicating weak elasticity), the crossover of G' and G'' often occurs at higher frequencies, where inertial effects are known to cause erroneous results. The frequency required to measure a shear relaxation time of 2.6 ms, for example, is nearly 400 Hz, which exceeds the maximum frequency limits of several commonly used rotational instruments (≈ 100 Hz). Furthermore, for dilute solutions G' may even be undetectable.

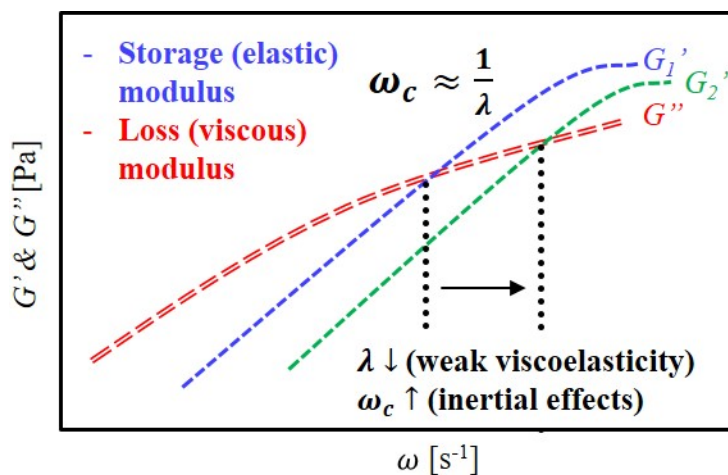


Figure 1.7: Dynamic oscillatory shear test depicting the crossover frequency, ω_c , where the storage modulus (G') and loss modulus (G'') intersect. The characteristic relaxation time of a polymer solution, λ , can be approximated as the inverse of the crossover frequency, $1/\omega_c$. Higher frequencies are needed to evaluate the characteristic relaxation times of weakly viscoelastic solutions, represented by the comparison of G'_1 and G'_2 relative to G'' .

Thus, when evaluating dilute-polymer solutions using a standard rotational rheometer, these fluids may appear Newtonian, having shear viscosities that are not dependent on shear rate and having dominating loss moduli. As a result, several novel techniques for characterizing weak viscoelasticity have been proposed [25, 36, 37, 74, 75]. The present work focuses on extensional techniques.

Challenges in Characterizing Weak Viscoelasticity in Extension – Limitations

of the CaBER The limits of operation for the CaBER have been summarized by Rodd and McKinley [25] in an operability diagram. Under optimal conditions, the minimum measurable relaxation time has been projected to be 1 ms for liquids with a shear viscosity of 3 mPa·s. More generally, for low-viscosity fluids ($Oh < 1$), the elastic stresses must be large enough ($De > 1$) to compete with the capillary-driven breakup. More conservatively, ThermoFischer Scientific lists a shear-viscosity range for the HAAKETM CaBERTM between 10 and 10^6 mPa·s, depending on the elasticity of the sample. Limiting factors for the CaBERTM include gravitational sagging [76], the finite time required to impose an initial axial deformation [77], and concerns regarding endplate effects [78]. In other words, for complex fluids having lower shear viscosities, the elastocapillary regime is often obscured by other dominating edge or inertial effects, or the breakup of the filament occurs on a time scale that is too quick to capture.

Recent improvements extending the capabilities of the CaBER include the use of a high-speed camera combined with a slow retraction method (SRM) to capture the rapid filament-thinning process [79]. By supplementing the CaBER, observed relaxation times have been reported as low as 240 μ s. In addition, by eliminating the finite step-strain required to form an initial filament, Dinic et al. have developed a robust and inexpensive technique that optically detects the elastocapillary self-thinning by dripping a fluid onto the surface of a substrate (DoS), and they have been able to characterize fluids with shear viscosities below 20 mPa·s and relaxation times below 1 ms [3, 43].

A more appropriate description of capillary-breakup limitations employs non-dimensional parameters. For flows that describe “self-thinning” processes in which no externally-imposed driving forces exist, one may consider the set of dimensionless parameters described in the previous section (Figure 1.5). For such experiments, fluids must be sufficiently viscous or elastic to resist the capillary-driven necking. Thus, the limitations for the CaBER can more generally be stated as $De > 1 > Oh$ for low-viscosity-elastic fluids or as $Oh > 1 > De$ for weakly-elastic or Newtonian fluids [25].

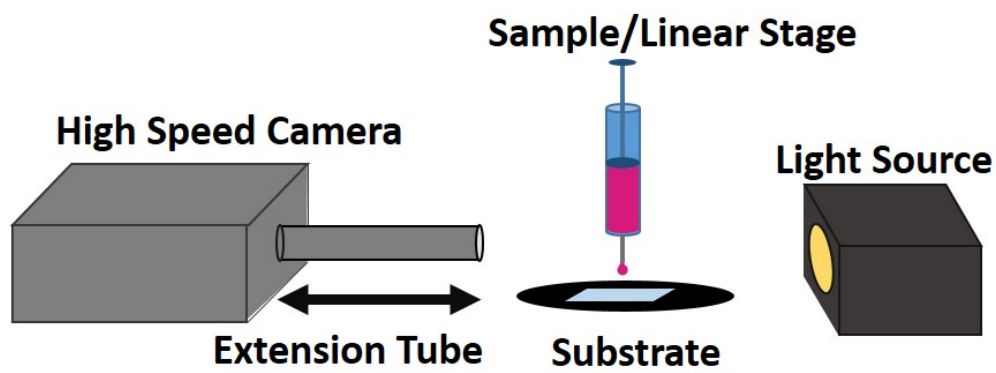
Other Capillary Breakup Techniques In addition to the necking and breakup of an extended liquid bridge [39, 65, 80–83], other techniques that have employed capillary breakup to characterize semi-dilute and dilute polymer solutions include the dripping [23, 84–87] and jetting [47–49, 88–91] of samples. The Rayleigh Ohnesorge jetting extensional rheometer (ROJER), for example, is a jetting technique that has been demonstrated to achieve extensional relaxation times down to $60 \mu\text{s}$ [49]. For the ROJER technique, the breakup of a fluid jet is controlled by imposing perturbations of a known amplitude and frequency. Similar to the CaBER, the evolution of the jet instability is monitored in real time, allowing for the characterization of complex fluids having viscosities on the same order of magnitude as water. Unlike the CaBER technique, however, disadvantages of the ROJER include challenges in optically tracking the evolving filament [48].

Dripping-onto-Substrate (DoS) To extend the capabilities of capillary breakup extensional rheometry, Dinic et al. developed the optically-detected elastocapillary self-thinning dripping-onto-substrate (ODES-DOS) technique (now referred to as DoS) [3]. Instead of applying a step-strain to a material, DoS works by expelling fluid from the tip of a syringe until it contacts the surface of a substrate. If the substrate is selected so that the fluid wets the surface, a filament will form that thins and breaks as a consequence of capillary forces. The extensional properties of the fluid can be evaluated, similar to CABER, by observing the evolution of the filament diameter in time.

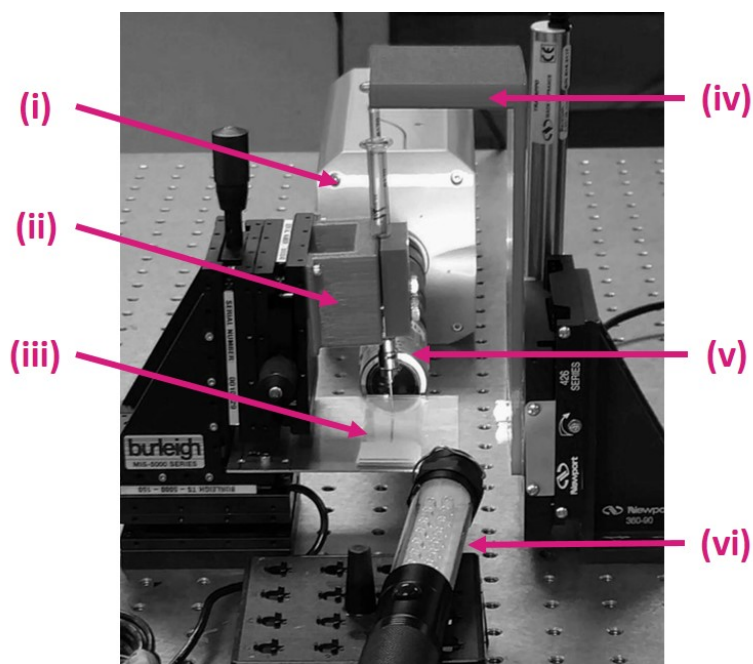
For the present work, a DoS device was built in-house. A diagram and image of the DoS setup are presented in Figure 1.8. Images of the filament-thinning and breakup process were captured using a Phantom[®] V4.1 high-speed camera attached to a 130-mm extension tube and a 10x objective. A Newport[®] compact motorized actuator was used to pump fluid from a syringe onto a glass substrate. Components including the syringe holder and parts of the syringe pump were 3D printed.

An example of raw images captured by the DoS for Newtonian and viscoelastic fluids of similar shear viscosities are presented in Figure 1.9. From a series of images, the breakup of the Newtonian glycerol/DIW solution is observed to occur rapidly, whereas the breakup of the viscoelastic PEO solution occurs in over double the amount of time. Thus, with the addition of a small amount of polymer, the breakup time nearly doubled. Additionally, no noticeable filament formation is observed for the glycerol/DIW solution.

Furthermore, to evaluate the limitations of the DoS device built in-house, a range of aqueous PEO ($MW = 7 \times 10^6$) solutions were tested. The two least concentrated solutions measurable were 250 ppm and 500 ppm. Figure 1.10(a) presents the filament decay profiles for these two samples. Here, the natural logarithm of the diameter is plotted versus time. The data was also normalized by the initial diameter of the filament and the evaluated relaxation times of the samples (Figure 1.10(b)). Normalizing the data in such a way causes the two profiles to collapse into one.

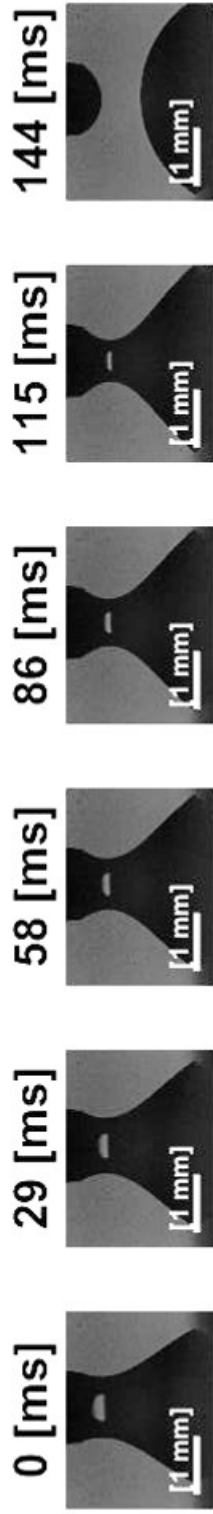


(a) DoS schematic.



(b) DoS laboratory setup.

Figure 1.8: (a) DoS setup adapted from [3]. (b) In-house setup with the components: (i) Phantom[®] V4.1 high-speed camera, (ii) syringe holder and syringe, (iii) substrate (glass slide), (iv) motorized syringe pump, (v) tube lens and 10x objective, and (vi) light source.

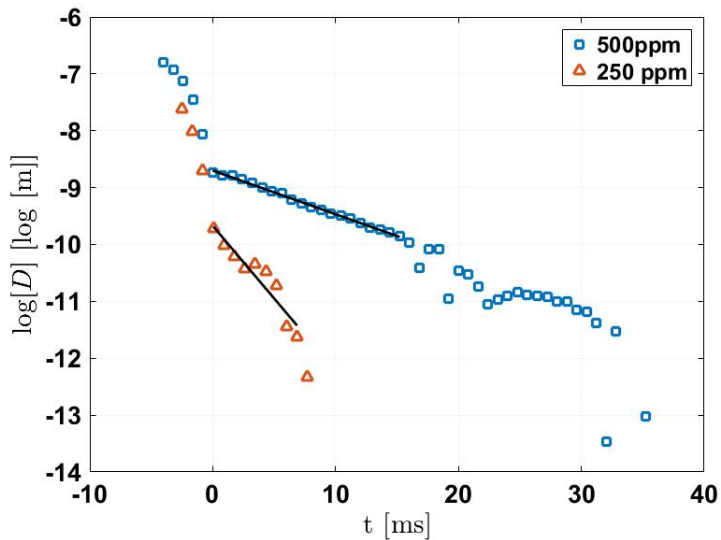


(a) Newtonian 60-wt% glycerol/DIW.

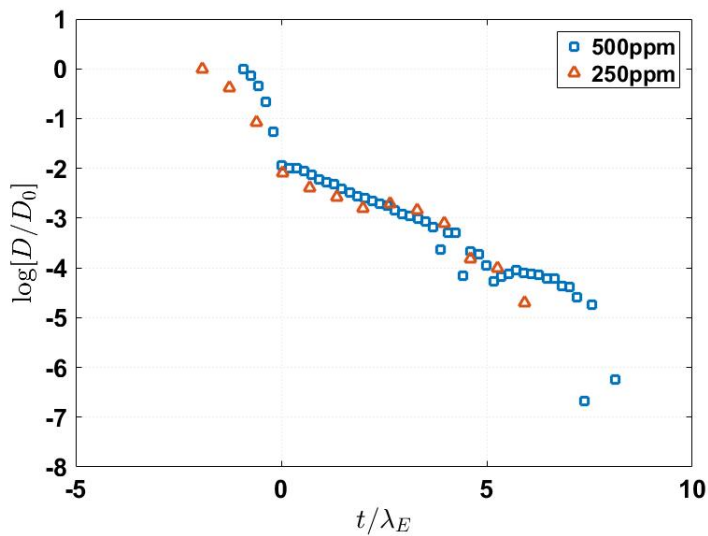


(b) Viscoelastic 65-wt% glycerol/DIW with 65 ppm PEO.

Figure 1.9: DoS diameter decay profiles for (a) a 60 wt% glycerol/deionized (DIW) water solution and (b) a 65 wt% glycerol/DIW with 65 ppm PEO. The breakup of the Newtonian glycerol/DIW solution is observed to occur rapidly, whereas the breakup of the viscoelastic PEO solution occurs in over double the amount of time. Additionally, no noticeable filament formation is observed for the glycerol/DIW solution.



(a) Raw data.



(b) Normalized data.

Figure 1.10: DoS diameter decay plots for 250- and 500-ppm aqueous PEO solutions. (a) Natural log of the diameter versus time. (b) Natural log of the normalized diameter versus normalized time. The diameter is normalized by the initial diameter of the filament, D_0 . Time is normalized by the relaxation times (1.3 ms and 4.3 ms) evaluated for the two samples, λ_E .

1.3.4 Rheology on the Microscale

Efforts to characterize weakly-viscoelastic fluids are ongoing. At lower concentrations of polymer, the filament thinning and breakup process transitions from being dominated by the characteristic time scale of the polymer to being dominated by the viscocapillary time scale described by the breakup of the Newtonian solvent [20]. Furthermore, at low shear viscosities, inertial effects can dominate. From the operating spaces described previously, both the elasticity number and elastocapillary number can be used to describe the relative elastic effects for a given system, and are functions of only the fluid rheology and the geometry. As these numbers become greater than unity, non-Newtonian effects are said to be more distinguishable [20, 37, 42]. Since the elastocapillary number and the elasticity number are proportional to the inverse of the characteristic length scale and the inverse of the characteristic length scale squared, as a system's size is decreased, the effects of elasticity become more pronounced, and inertial effects become less important.

Thus, with the advancement in and growing use of microfluidic devices for various lab-on-a-chip applications, not only does a greater need exist to characterize fluids having properties that are not generally pronounced on large length scales, but an opportunity to exploit these devices also exists. Additional interest in microscale and nanoscale characterization techniques include small sample sizes and the possible use of an outer fluid that is not air. Although commonly used, free-surface techniques are less than desirable for characterizing volatile fluids that can rapidly change properties upon exposure to air.

Recently, several attempts have been made to incorporate the small length scales of microfluidic devices for characterizing the extensional properties of weakly-viscoelastic fluids. A review containing several microfluidic concepts is presented by Galindo-Rosales et al. [37]. The optimized cross-slot device (OSCER) developed by McKinley and co-workers, for example, has proven successful in providing constant, homogeneous extension rates at low Reynolds numbers and has already been used for characterizing fluids such as hyaluronic

acid [4, 31]. A review of such stagnation-point flows is presented by Haward [38]. Although the techniques that are described monitor the behavior of a single-phase flow, two-phase droplet breakup at the center of a cross-slot geometry has yet to be considered.

Chapter 2: Investigating the dynamics of droplet breakup in a microfluidic cross-slot device for characterizing the extensional properties of weakly-viscoelastic fluids

2.1 Abstract

Dilute and semi-dilute polymer solutions are used in a wide-range of applications. In such processes, small amounts of macromolecule are added to enhance the performance of the working fluid, and regardless of being a desired outcome or not, the presence of elasticity may significantly impact the flow response of the fluid, particularly in extension. The present research was conducted in an effort to make improvements to and to provide an in-depth assessment of the techniques available for characterizing weak viscoelasticity. Outcomes of this work include the creation of a new device for extensional characterization and the completion of a study comparing a number of previously described extensional techniques.

A microfluidic device, deemed the Plateau-Rayleigh microfluidic extensional rheometer (PRIMER), is presented that uses a cross-slot geometry to observe a two-phase droplet breakup event. For viscoelastic fluids, we report that a cylindrical filament forms between droplet segments with a diameter that decays exponentially in time. In optically tracking this decay, both transient extensional viscosities and relaxation times can be evaluated. For validating and optimizing the device, a range of poly(ethylene oxide) (PEO) and Newtonian solutions were tested. Comparisons of the evolution profiles as a result of the presence of elasticity are made, and these results are compared with the results from other emerging extensional techniques. In addition to the breakup event, the droplet formation event is investigated to manipulate the spacing of the droplets that are entering the cross-slot.

2.2 Introduction

The addition of linear macromolecules to solvent, even in dilute quantities, can significantly alter a fluid’s response in an extensional or stretching flow. When high-molecular-weight molecules are extended in solution, extensional thickening can result when polymer chains undergo coil-stretch transitions, yielding extensional viscosities that are orders of magnitude larger than values found in shear. Such behavior is often manifested as the “stringy” or “tacky” nature of a fluid, and it will vary depending on the concentration, molecular weight, and type of the polymer that has been added to a given system. For dilute and semi-dilute polymer solutions, the presence of elasticity may not be apparent in steady or oscillatory shear flows, yet it may alter the response of a fluid when undergoing an extensional deformation. For example, during the process of inkjet printing, small amounts of polymer can be added to the ink to prevent unwanted satellite drops from diminishing the quality of the print [72]. Yet, when performing shear rheometry, such inks may “appear” Newtonian, having zero-shear viscosities on the same order of magnitude as water.

Other applications employing small quantities of polymer include additives in subsurface flows [13, 14, 32], turbulent drag flow reduction [16, 17, 92], and enhanced particle removal [15] (Figure 2.1). In each of these applications, the predominant mode of deformation is extensional, and the characteristic length scales are on the order of a few microns or less. Despite the obvious need to measure the extensional properties of such dilute and semi-dilute polymer solutions, developing reliable characterization techniques for fluids that are low viscosity or weakly elastic serves as a major obstacle in the field of rheology [51], and it is the focus of the present study.

Over the past 30 years, accurately measuring the extensional viscosity of polymeric liquids has been a major obstacle in the field of rheology, particularly for more mobile polymer solutions [51]. Despite numerous techniques being developed to address this need, discrepancies as a consequence of pre-deformation history, an inability to provide a com-

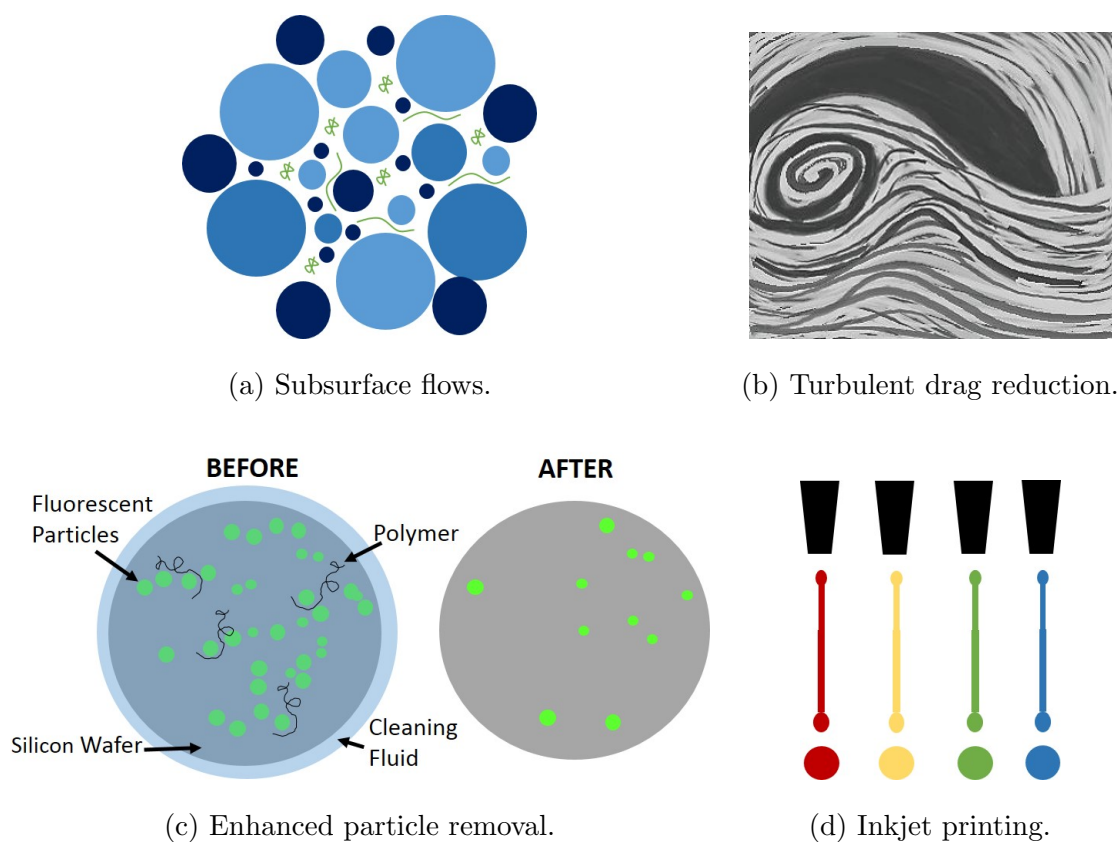


Figure 2.1: Applications employing semi-dilute and dilute polymer solutions. (a) Polymers used in subsurface flows include surfactants for enhanced oil recovery. Pore sizes can vary from nanometers to millimeters, impacting how a fluid is transported. (b) In turbulent drag flow reduction, polymers hinder the formation of turbulent eddies and reduce energy costs associated with pumping. (c) In enhanced particle removal, the addition of polymer to chemical mechanical planarization (CMP) chemistries can assist in the removal of micro- and nano-sized particles from the surfaces of silicon wafers in semi-conductor processing. (d) Polymers are added to inkjet printing chemistries to increase the robustness of the ink and to eliminate satellite droplets. Viscoelastic behavior is noted as small volumes of ink are jetted from micron-sized nozzles.

pletely shear-free flow, and the transient nature of extensional stress growth have led to inconsistencies in apparent extensional viscosity measurements [93, 94]. Nevertheless, the path to improved experimental design is becoming more certain, as progress is being made in the theoretical comprehension of extensional flow behavior. In fact, a number of extensional techniques have been proposed that are capable of characterizing a range of materials from low-viscosity dilute and semi-dilute polymer solutions [25, 36] to more viscous polymer melts [33–35, 40]. Of the techniques commercially available, the majority are geared towards more viscous complex fluids. Methods for characterizing dilute and semi-dilute polymer solutions, on the other hand, are limited in number, and extending the range of testable materials, particularly for less viscous complex fluids, is desired [37].

Capillary Breakup Extensional Rheometry (CaBER) The Capillary Breakup Extensional Rheometer (CaBERTM) is a type of filament stretching rheometer capable of measuring viscoelastic fluids with lower shear viscosities than other commercially available devices. First presented by Entov and co-workers [39, 65], capillary breakup extensional rheometry monitors the gradual necking and breakup of a self-thinning filament as a result of competing viscous, elastic, and capillary forces, where the resulting evolution profile of the filament is distinct for Newtonian and viscoelastic fluids [39, 65]. Unlike a filament stretching rheometer – where a sample continues to stretch while imposing a constant stress or strain rate [40] – the CaBER applies a finite step-strain to a material initially loaded between two parallel plates, forming an unstable filament that breaks under the action of capillary forces [40, 95]. Once the filament is formed, it thins at a strain rate determined by the extensional properties of the fluid. At late times in the thinning process, as the filament necks and breaks, large extensional strains are achieved that can promote significant elastic effects.

Discussions on the early, middle, and late time dynamics of the capillary-driven thinning and breakup process of a cylindrical filament are provided in the literature [42, 65].

For Newtonian fluids, the evolution of the filament diameter is dominated by visco-capillary stresses acting on the fluid, and it has been shown to be linear in time [65]. For quantifying the elastic properties of a sample, the filament-thinning dynamics of interest occur in the middle elastocapillary regime, where elastic stresses grow large enough to counteract the capillary pressures that drive the breakup event. For dilute and semi-dilute polymer solutions modeled as FENE noninteracting dumbbells, the time-evolution of the filament diameter, $D(t)$, is exponential according to

$$\frac{D(t)}{D_1} = \left[\frac{GD_1}{4\sigma} \right]^{1/3} \exp \left[-\frac{t}{3\lambda_E} \right], \quad (2.1)$$

such that λ_E is the characteristic relaxation time of the sample in extension, D_1 is the diameter of the sample after the initial step-strain has been applied, and σ is the interfacial tension [65, 66]. G is the shear elastic modulus.

By evaluating the force balance between viscous, elastic, and capillary stresses that are acting within a sample, the CaBER technique can be used to approximate the transient extensional viscosity ($\eta_E^+(\varepsilon)$) as a function of Hencky strain [28, 42]. For the present text, only the diameter-decay profiles and resulting characteristic relaxation times are considered.

For the uniaxial extension of a cylindrical filament at a constant strain rate, the diameter of a filament decays according to

$$D(t) = D_0 \exp \left[-\frac{\dot{\varepsilon}t}{2} \right], \quad (2.2)$$

such that D_0 is the initial diameter of the fluid element, and $\dot{\varepsilon}$ is the strain rate [28]. Comparing Equations 2.1 and 2.2, the strain rate is found to be self-selected and inversely proportional to the characteristic relaxation time, independent of pre-strain and the initial aspect ratio of the filament. Thus, the corresponding Weissenberg number is a constant, $Wi = \lambda_E \dot{\varepsilon} = 2/3$, which is above a critical value, $Wi_{cr} = 1/2$, where individual polymer chains can be significantly strained from their equilibrium conformations and undergo coil-

stretch transitions [68,69]. Such thinning behavior has been investigated and observed over a range of polymer types, concentrations, and molecular weights [67,96,97].

Several contributors have added to the CaBER technique, both experimentally and theoretically in predicting the evolution of self-thinning filaments for various constitutive models [3,25,41,52,97,98]. Although Equation 2.1 was developed for monodisperse solutions, the exponential relationship has held true for other polymeric solutions of varying concentration and molecular weight that has been investigated in the literature [39,67,93,96,97]. In addition, multi-mode models have been developed, indicating that the presence of shorter relaxation time scales contribute to the initial rapid decay of the filament, whereas the longest relaxation time causes a late-time decay that is exponential [20,96].

The limits of operation for the CaBER have been summarized by Rodd and McKinley in an operability diagram [25]. In a capillary-thinning and breakup test, the capillary-driven thinning is resisted by either viscous or elastic stresses in the filament. Under optimal conditions, the minimum measurable relaxation time has been projected to be 1 ms for liquids with a shear viscosity of 3 mPa·s. More conservatively, ThermoFischer Scientific lists a shear-viscosity range for the HAAKE™ CaBER™ between 10 and 10⁶ mPa·s, depending on the elasticity of the sample. A more appropriate description of CaBER limitations employs the non-dimensional numbers describing the operation window of filament stretching devices. For flows that describe “self-thinning” processes, such as the capillary thinning and breakup of cylindrical filaments in which no externally imposed driving forces exist, one may consider a set of dimensionless parameters clearly outlined by McKinley [2].

For such processes, three time scales – elastic, viscous, and inertial – are employed. The elastic time scale is the relaxation time (λ_E) of the polymer in extension. The viscous time scale is the time for a capillary-driven breakup event to occur as a result of competing viscous and capillary forces, $t_{vb} \sim \eta_0 \ell / \sigma$. The Rayleigh time scale describes the breakup of an inviscid jet ($t_R = [\rho \ell^3 / \sigma]^{1/2}$) and is used to express the magnitude of inertial effects in capillary breakup processes [57]. Here, ℓ is the characteristic length scales of interest, ρ is

the density, and η_0 is the zero shear viscosity of the solution.

Comparing the above time scales, additional dimensionless groups can be evaluated. The Ohnesorge number compares the magnitude of viscous and inertial effects, and it is presented such that

$$Oh = \frac{t_{vb}}{t_R} \sim \frac{\rho\sigma l}{\eta_0^2}. \quad (2.3)$$

To define a low-viscosity fluid in capillary breakup experiments, the viscous time scale should be less than the inertial time scale such that the Ohnesorge number is less than unity, $Oh < 1$.

Additionally, a second dimensionless parameter arises when comparing the time scale for the stress relaxation to the Rayleigh time scale that is presented above. This “intrinsic” Deborah number for free surface viscoelastic flows is defined as follows

$$De_{int} = \frac{\lambda}{t_R} = \frac{\lambda}{\sqrt{\rho l^3 / \sigma}}, \quad (2.4)$$

and it is independent of flow properties such as velocity.

For low-viscosity and weakly-elastic fluids, inertial effects often conceal the non-Newtonian stresses in the fluid. Thus, the limitations for the CaBER can more generally be stated as $De > 1 > Oh$ for low-viscosity elastic fluids or $Oh > 1 > De$ for weakly-elastic or Newtonian fluids [25]. Additional limiting factors for the CaBER include gravitational sagging [76], the finite time required to impose an initial axial deformation [77], and concerns regarding endplate effects [78]. Recent improvements extending the capabilities of the CaBER include the use of a high-speed camera combined with a slow retraction method (SRM) to capture the rapid filament-thinning process [79]. By supplementing the CaBER in this way, observed relaxation times have been reported as low as 240 μs . In addition, by eliminating the finite step-strain required to form an initial filament, Dinic et al. [3, 43] have developed a robust and inexpensive technique that optically detects the elastocapillary self-thinning of a fluid that is dripping onto the surface of a substrate (DoS), and they have

been able to characterize fluids with shear viscosities below 20 mPa·s and relaxation times below 1 ms.

Efforts to characterize weakly-viscoelastic fluids are ongoing. At lower concentrations of polymer, the filament-thinning and breakup process transitions from being dominated by the characteristic time scale of the polymer to being dominated by the visco-capillary or inertio-capillary time scales that are described above [2]. The elastocapillary number describes the ratio of the intrinsic Deborah number to the Ohnesorge number,

$$El = \frac{De}{Oh} = \frac{\lambda\sigma}{\eta_0\ell}, \quad (2.5)$$

comparing the viscous and elastic time scales. As this number becomes greater than unity, elastic effects are said to be more distinguishable [20, 37, 42]. Additionally, the elasticity number

$$El = \frac{Wi}{Re} = \frac{\lambda_E\eta_0}{\rho\ell^2}, \quad (2.6)$$

is another dimensionless parameter that describes the importance of inertial, viscous and elastic contributions in a system [99]. Since the elastocapillary number and the elasticity number are proportional to the inverse of the characteristic length scale and the squared characteristic length scale, as the size of a system is decreased, the effects of elasticity are assumed to become more pronounced.

Despite decades of progress in CaBER and similar capillary breakup techniques [48, 49, 84, 100, 101], several avenues have yet to be exhausted for their potential in characterizing dilute and semi-dilute polymer solutions. Microfluidics provides such a means, and the goal of the present work is to apply the capillary-breakup process, already well established on the macroscale, to the microscale.

Rheometry on the Microscale Recently, attempts have been made to incorporate the small length scales of microfluidic devices for characterizing the extensional properties of

low-viscosity dilute and semi-dilute polymer solutions. Additional benefits of microfluidics are the small sample sizes needed to take a measurement and the growing interest in lab-on-a-chip devices for medical and industrial applications. A review containing several of these concepts is presented by Galindo-Rosales et al. [37]. Devices already considered in the literature include stagnation-point geometries [4,102–104], contraction-expansion flows [105], flow-focusing devices [106], and the passive breakup of droplets at a T-junction [24].

The optimized cross-slot device (OSCER), for example, has proven successful in providing constant, homogeneous extension rates at low Reynolds numbers, and it has already been used for characterizing fluids such as hyaluronic acid [4,31]. The OSCER uses a cross-slot geometry to develop a stagnation point, where polymer molecules can be stretched. Stagnation-point geometries have been shown to produce large Hencky strains, allowing for the full uncoil of flexible macromolecules so that elastic stresses are pronounced. A review of microfluidic extensional rheometry using stagnation point flow is presented by Haward [38]. Although the techniques that are described monitor the behavior of a single-phase flow, two-phase droplet-breakup at the center of a cross-slot geometry has yet to be considered.

The present study investigates the use of droplet breakup in a cross-slot geometry for the extensional characterization of low-viscosity complex fluids. Although the passive breakup of droplets at a T-junction has been previously suggested as a means for characterizing low-viscosity elasticity [24], the present study aims to validate and expand on such ideas, adding a symmetry component to the droplet splitting environment. In the present work, a Plateau-Rayleigh instability microfluidic extensional rheometer (PRIMER) is presented that uses a cross-slot geometry to initiate a droplet-breakup event. A T-junction is used to form monodisperse droplets. To ensure that droplets will not collide downstream, the size and frequency of the droplets are controlled by adjusting the ratio of the flow rates into the device. At the cross slot, droplets are carried to a stagnation point, where they subsequently extend and break, as depicted in Figure 2.2. For viscoelastic samples, filaments that form are evaluated using the same approach as in CaBER experiments.

Since droplet splitting in a cross-slot geometry has not been extensively studied in the literature, the present work compares the breakup dynamics of a range of polymer solutions and Newtonian solutions with comparable shear viscosities. Poly(ethylene oxide) (PEO) is selected as the working polymer, as it is well characterized in the literature, and it has been used to observe the effects of viscoelasticity on droplet formation and splitting at a T-junction [24,107,108]. Both the concentration of PEO as well as the global parameters in the cross-slot are investigated for their impact on the droplet-breakup event. In particular, we observe how flow rates and the selection of the outer viscous fluid can impact measurement results. The early, middle, and late time dynamics of the droplet breakup process are monitored and compared for a variety of flow conditions as well as with previous studies [24,107–110]. The overarching goal of the present study is to explore the capacity of droplet breakup in a microfluidic cross-slot for characterizing the extensional properties of viscoelastic fluids, particularly for low-viscosity and weakly-elastic fluids.

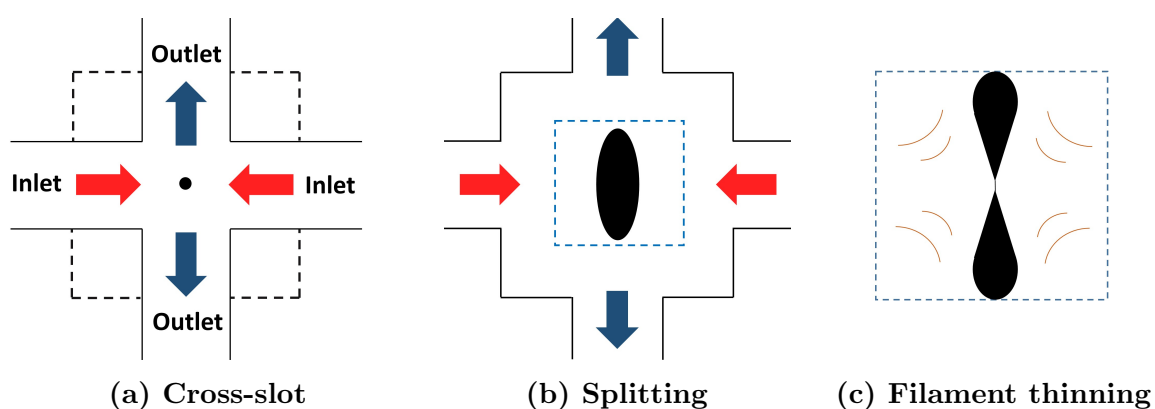


Figure 2.2: A schematic of droplet splitting at the stagnation point of a microfluidic device. (a) A generic cross-slot configuration is presented with opposing inlet and outlet channels (solid lines). A stagnation point is depicted at the center of the geometry. To reduce shearing effects at the channel walls and to promote a purely extensional flow, the shape of the cross-slot can be modified (dashed-lines) as discussed by Haward et al. [4]. (b) Droplet splitting at the stagnation point of the cross-slot is depicted. Initially, the droplet is elongated towards the outlet channels until a rapid breakup event is initiated. (c) An enlarged view of the cross-slot where filament thinning is presented. For viscoelastic fluids, filaments can be formed that connect the two droplet segments. The resulting filament decay profile is monitored and analyzed using a similar approach as in CaBER experiments.

2.3 Materials and Methods

2.3.1 Microfluidic Design and Fabrication

The PRIMER device that was developed for the present study consists of two main geometries – a T-junction that is used for droplet formation and a cross-slot that is used to initiate a droplet-breakup event (Figure 2.3). The generation of Newtonian and viscoelastic droplets at T-junction geometries is well-described in the literature [6, 108, 109, 111, 112]. In an attempt to provide an additional symmetry component and to remove possible wall effects, a cross-slot geometry, rather than a T-junction, was selected for splitting the droplets. In general, a cross-slot geometry consists of perpendicular channels that have opposing inlet and outlet streams, generating a stagnation point, where the channels intersect.

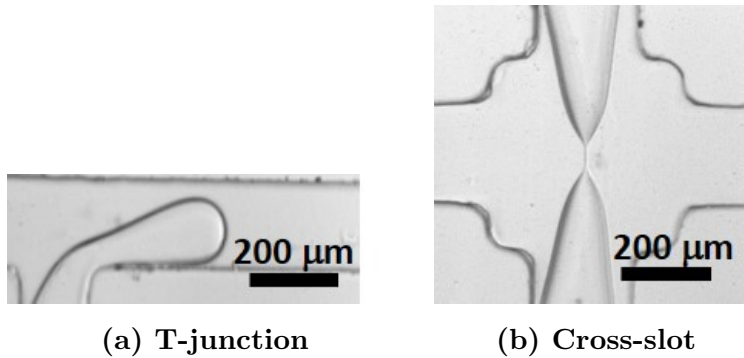


Figure 2.3: The two main geometries used in the PRIMER design. (a) A T-junction geometry used to create droplets as the continuous phase silicone oil pinches the dispersed-phase sample. (b) A cross-slot geometry used to initiate a droplet-breakup event at a stagnation point.

At the stagnation point, the local velocity is zero, and the surrounding streamlines form an elongational flow that is directed towards the outlet channels. Stagnation-point geometries have been shown to produce large Hencky strains, allowing for the uncoil of flexible macromolecules [4, 102, 103, 113]. In the present study, the cross-slot design was fabricated to be similar to the design proposed by Haward et al. [4], such that corners were added to help “self-lubricate” the flow, minimizing shearing effects at the walls (Figure 2.2a). Here,

the “continuous phase” describes the fluid that assists in forming, transporting, and extending droplets of the immiscible “dispersed-phase” sample. More information regarding the selection of the continuous- and dispersed-phase fluids are discussed in Section 2.3.3. Devices were composed of polydimethylsiloxane (PDMS), fabricated using standard photolithography and soft lithography techniques [114,115]. PDMS was chosen as a substrate for the material’s transparency (necessary for optical detection), ease of fabrication, and cost considerations.

Photolithography For performing photolithography, photomask designs were created using SOLIDWORKS[®] 2D CAD software and produced by CAD/Art Services, Inc., with a film size of 500 dots per inch (DPI) for a minimum guaranteed feature size of 50 μm . To prepare the master mold, a MicroChem SU-8 2100 negative photoresist was patterned onto a silicon wafer. To improve the adhesion of the photoresist, the surface of the silicon wafer was plasma cleaned (XEI Scientific Evactron[™] Decontaminator) for approximately two minutes prior to being spun onto the surface of the wafer. The photoresist was spun, baked, exposed, and developed according to SU-8 2100 processing guidelines provided by MicroChem [116].

Soft Lithography For soft lithography, a DOW Corning Sylgard[®] 184 silicone elastomer kit was used with a 1:10 ratio of base to curing agent, as recommended by DOW Corning. The elastomer was then placed under vacuum to remove any excess air bubbles that were generated from the reaction of the base and curing agent. Once air bubbles had been removed, the PDMS was carefully poured over the silicon master, covering the SU-8 pattern. The wafer was then placed in a vacuum oven at 70°C for at least one hour. Once cured, the PDMS was peeled from the silicon master to avoid damaging the SU-8 pattern. To close the channels, a second sheet of PDMS was made on a smooth surface. The two pieces of PDMS were then placed in a oxygen plasma etcher (XEI Scientific Evactron[™] Decontaminator) for three minutes and firmly pressed together to irreversibly bond the surfaces. Devices were

then baked overnight at 70°C to allow the channels to regain hydrophobicity. The second piece of PDMS was used to ensure uniform wetting of the channels. A detailed protocol for soft lithography is provided by Friend et al. [115].

2.3.2 Experimental Setup

The resulting PRIMER device contained rectangular channels having inlet widths, w_{in} and w , of approximately $200\ \mu\text{m}$ and a cross-slot consisting of a $400\ \mu\text{m} \times 400\ \mu\text{m}$ opening with rounded corners. The height, h , of the channels, determined using a Zygo ZeScope, was approximately $176\ \mu\text{m}$, similar to the width to the device channels ($h/w \approx 1$). A schematic of the overall PRIMER device is presented in Figure 2.4.

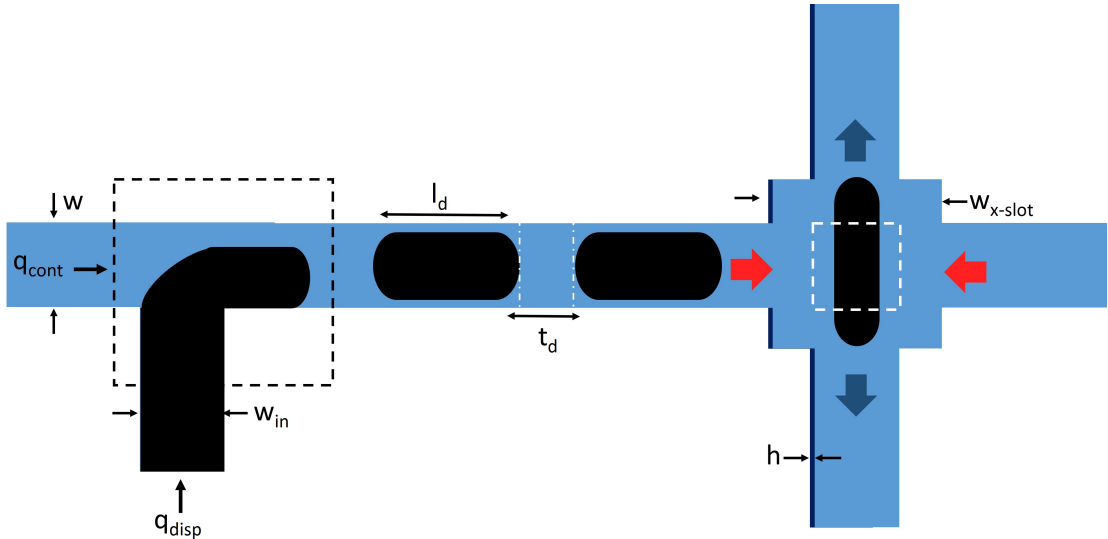


Figure 2.4: An overall schematic of the cross-slot device, including the continuous- and dispersed-phase inlet channels with widths of w and w_{in} , respectively. The length, l_d , and time spacing, t_d , between droplets were controlled by adjusting the ratio of the continuous and dispersed-phase flow rates, q_{cont}/q_{disp} . The height of the device, h , was similar in magnitude to the width of the channels. The width of the cross-slot, w_{xslot} , was greater than the width of the channels, minimizing wall effects.

To control the volumetric flow rates in the device, an NE-1002X Programmable Microfluidics syringe pump and an Orion SageTM M361 syringe pump were used. Flow rates ranged

between 0.01 and 1 ml/hr, depending on the type of continuous- and dispersed-phase fluids being fed into the device. When using higher-viscosity fluids, lower flow rates were required to prevent leaking from the device induced by back pressure. Prior to use, all channels were primed with continuous phase to pre-wet the channel walls. After priming the channels, the dispersed-phase pump was started. When changing flow rates in the device, time was given to ensure that steady-state droplet formation was achieved.

At the T-junction, images were captured at a rate of 50 fps and a resolution of 800 pixels \times 600 pixels using the Phantom[®] V4.1 high-speed camera fixed to a Nikon Eclipse Ti-S inverted microscope at 4x and 10x magnification. Droplet tracking was performed using a custom-built MATLAB[®] code. The code was used to evaluate the length of the dispersed-phase droplets formed, l_d , as well as time delay between two droplets entering the cross-slot, t_d . To ensure that droplets would not collide downstream, the size and frequency of the droplets were controlled by adjusting the ratio of the flow rates into the device. Results on controlling this time spacing are discussed below.

At the cross-slot, images were captured at a rate of 1265 fps and a resolution of 800 pixels \times 600 pixels at 40x magnification. Once entering the cross-slot, droplets were tracked until a breakup event was complete. Image analysis was used to extract the evolution of the droplet diameter as a function of time. Examples of the image processing performed are given in Figures 2.5 and 2.6.

To validate the accuracy of the syringe pumps being used, the droplet velocities were converted into volumetric flow rates using the known dimensions of the channels. The evaluated flow rates were then shown to be consistent with the summation of continuous (V_{cont}) and dispersed phase (V_{disp}) flow rates (Figure 2.7) input into the syringe pumps.

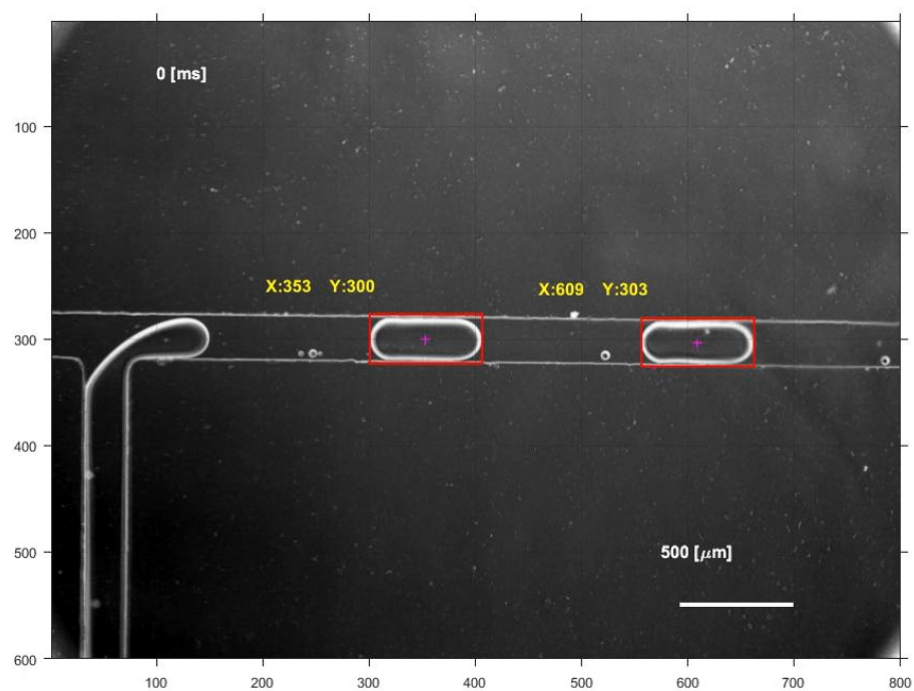


Figure 2.5: Image processing of droplets forming at a T-junction. Droplets are tracked based on parameters such as orientation and size relative to other objects in the frame.

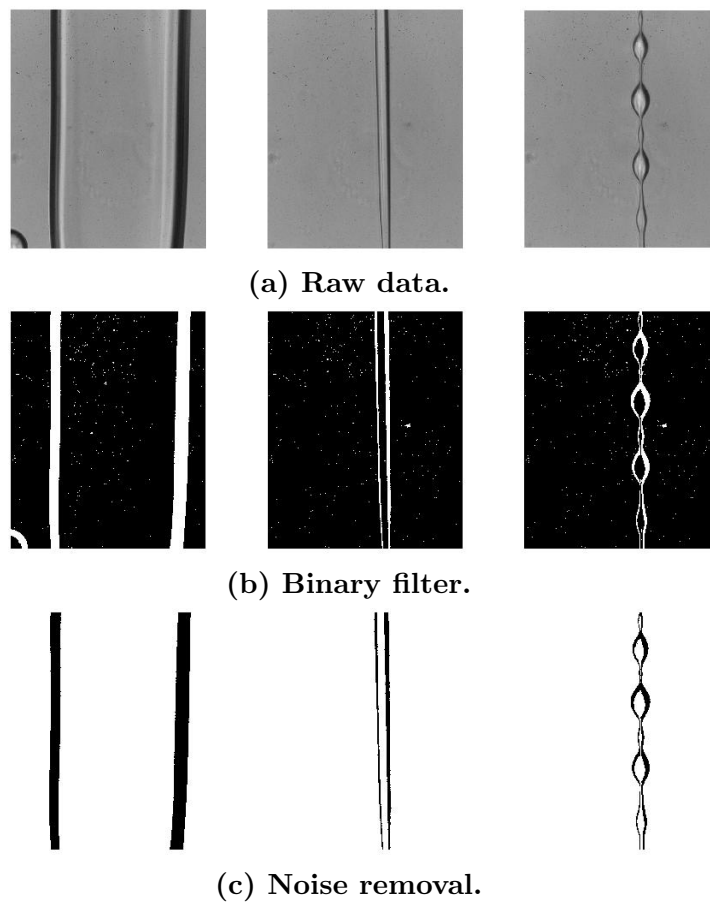


Figure 2.6: Image processing of a single droplet-breakup event in the cross-slot of the PRIMER device at early, middle, and late times. Images were captured in grayscale and converted to binary using a custom-built MATLAB[®] code. (a) Raw images captured in grayscale. (b) A binary filter applied to the raw images. (c) A custom filter applied to remove background noise.

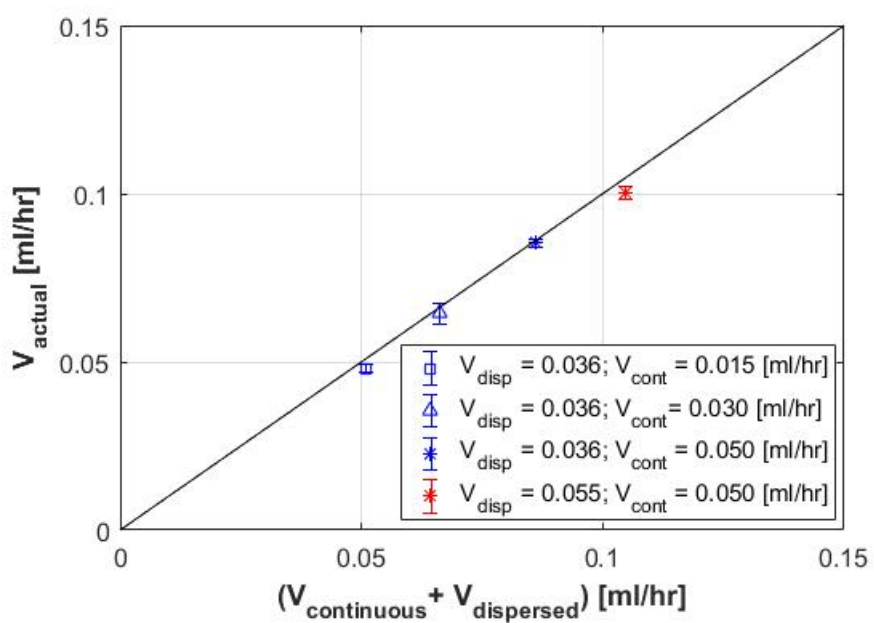


Figure 2.7: Validating the accuracy of the syringe pumps used in the present study. A comparison of the volumetric flow rates evaluated by droplet tracking (V_{actual}) to the summation of the continuous (V_{cont}) and dispersed phase (V_{disp}) flow rates input into the syringe pumps.

2.3.3 Selection of Continuous- and Dispersed-Phase Solutions

Dispersed Phase For testing and validating the device, two types of dispersed-phase solutions were used. The first type of dispersed-phase solution consisted of high-molecular-weight ($MW = 7 \times 10^6$) poly(ethylene oxide) (PEO) dissolved in deionized water (DIW). Aqueous PEO solutions were selected, as they are well-characterized in the literature [3, 48, 117]. The second type of dispersed-phase solution tested consisted of glycerol (GLY) dissolved in deionized water (DIW) to produce Newtonian fluids of similar zero-shear viscosities as the PEO solutions tested. A summary of the dispersed-phase solutions is provided in Table 2.1.

Table 2.1: A summary of the dispersed-phase solutions tested in the PRIMER device, including viscoelastic solutions composed of poly(ethylene oxide) (PEO) in deionized water and Newtonian glycerol (GLY)/water solutions.

Poly(ethylene oxide) in Water				
Composition	c/c^*	η_0 [mPa·s] at 25° C	Shear Thinning	Filament*
5000 ppm	13	200	Yes	Yes
500 ppm	1	1.2	No	Yes
100 ppm	0.3	0.96	No	Yes
50 ppm	0.1	0.95	No	No
10 ppm	0.03	0.90	No	No
Glycerol in Water				
Composition	c/c^*	η_0 [mPa·s] at 25°C	Shear Thinning	Filament*
90 wt%		164	No	No
80 wt%		43	No	No
10 wt%		1.2	No	No

*Filament was formed during the droplet-breakup event.

To prepare the aqueous PEO solutions, a 5000-ppm stock solution was made by dissolving Dow Chemical Company POLYOXTM WSR 303 in DIW and slowly rolling the solution at room temperature to allow for homogenization. The Mark-Houwink-Sakurada (MHS) relationship was used to evaluate the critical overlap concentration, c^* , for PEO in DIW

according to the relationship:

$$[\eta] = K[M_v]^a, \quad (2.7)$$

where $[\eta]$ is the intrinsic viscosity, M_v is the volume average molecular weight, and the parameters K and a depend on the polymer/solvent system, which can be found in a handbook for common polymers [7]. According to Graessley [21], c^* can be evaluated as

$$c^* \approx \frac{1}{[\eta]}. \quad (2.8)$$

The stock solution, evaluated to be approximately 13 times c^* , was diluted as necessary to ensure that the samples were in known concentration regimes. Dilutions were made at 10, 50, 100, and 500 ppm ($c/c^* \approx 0.03, 0.1, 0.3, 1, 13$, respectively). All solutions were prepared at room temperature and allowed to equilibrate for 48 hours prior to use. Samples were stored in amber glass bottles under nitrogen, to prevent degradation to the polymer.

To characterize the shear rheology of the dispersed-phase solutions, the samples were tested using a TA Instruments AR-G2 torsional rheometer equipped with a 60-mm 1° cone and a Peltier plate. In general, for low-viscosity samples, a standard rotational rheometer is limited by low-torque limits as well as secondary flow effects as described by Ewoldt et al. [5], limiting the allowable range of shear rates that can be tested. For the present work, low- and high-shear-rate co-plots approximated for a 60-mm cone were plotted along with the data to indicate where sampling errors may have occurred.

Although the low-torque limit does not appear to describe the thinning behavior seen for the 10- to 500-ppm samples at shear rates below 50 s^{-1} (Figure 2.8), the data in this range was not repeatable when other geometries were used to characterize the samples. Thus, the samples did not appear to shear thin over the reliable range of shear rates tested, and they had shear viscosities of approximately the same order of magnitude, $O(10^{-3})$.

For the 5000-ppm stock solution, shear-thinning behavior was noted over the range of shear rates tested (Figure 2.9). Fitting the data from the plot of viscosity versus shear rate,

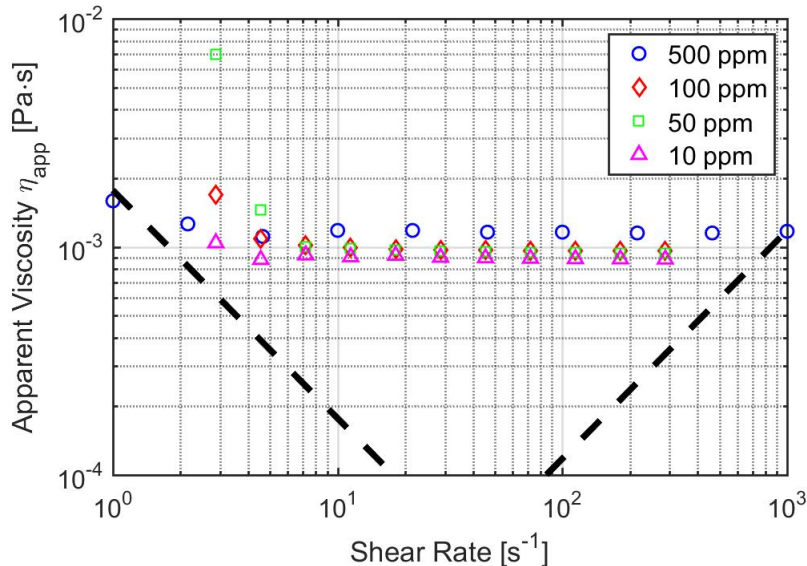


Figure 2.8: AR-G2 flow sweep results for the 10 to 500-ppm PEO ($MW = 7 \times 10^6$) solutions tested using the cross-slot microfluidic device. Shear characterization was performed at 25°C. The black dashed lines indicate where low-torque (left limits) and inertial effects (right limits) may lead to errors in measurement, evaluated according to Ewoldt et al [5].

the zero-shear viscosity of the stock solution was evaluated to be approximately 200 mPa·s, two orders of magnitude greater than the 10-500 ppm solutions. The flow behavior of the 5000-ppm stock solution was thus dominated by the presence of entanglements.

The Newtonian glycerol/DIW solutions were formulated to have similar shear viscosities as the PEO solutions used in the present study. A range of viscosities was desired to better understand how viscous stresses influence the droplet-breakup process. Since glycerol is known to be hygroscopic, shear characterization was performed to validate the compositions of the solutions and to measure the resulting shear viscosities. The data for the glycerol/DIW solutions is presented in Figure 2.10 reflecting compositions of 10, 80, and 90 wt% glycerol.

Continuous Phase In selecting continuous-phase fluids to be used, choosing fluids that preferentially wet the surface of the PDMS channels relative to the dispersed phase was

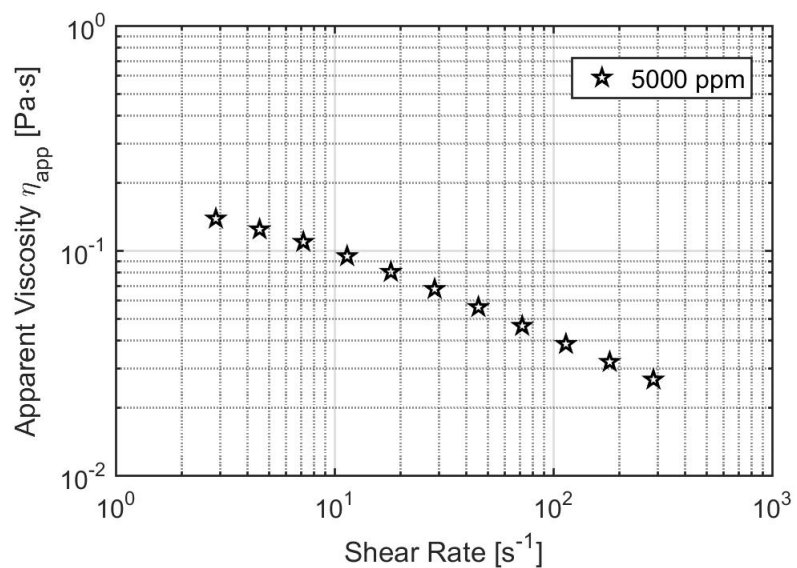


Figure 2.9: AR-G2 flow sweep results for the 5000-ppm PEO ($MW = 7 \times 10^6$) stock solution tested using the cross-slot microfluidic device. Shear characterization was performed at 25°C

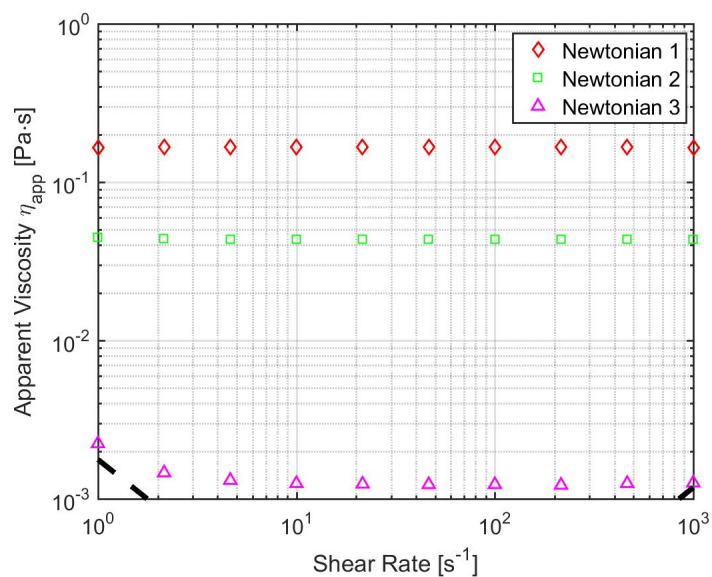


Figure 2.10: AR-G2 flow sweep results for the glycerol/DIW solutions tested using the cross-slot microfluidic device. Shear characterization was performed at 25°C . The data reflects compositions of 10 (Δ), 80 (\square), and 90 (\diamond) wt% glycerol.

important to ensure that the disperse-phase sample would not be attracted to the channels. The wettability of the continuous phase is known to be an important factor in the droplet formation process, and it could interfere with the droplet-breakup event, if not considered appropriately [6]. To better understand the influence of the continuous-phase fluid on the droplet-breakup and filament-formation processes, silicone oils over a range of shear viscosities (from 30 to 500 mPa·s) were tested. For the present work, the interfacial tensions between the continuous- and dispersed-phase fluids were assumed to be on the same order of magnitude, $O(30 \text{ mN/m})$, as what is reported in the literature [24].

Dripping-onto-Substrate (DoS) After preparation, dispersed-phase samples were evaluated using the dripping-onto-substrate (DoS) technique presented by Dinic et al. [3, 43], reminiscent of other extended-liquid-bridge techniques in the literature [81]. Similar to the CaBER, the DoS technique uses capillary breakup to evaluate the extensional properties of a sample by slowly dispensing the sample from the tip of a needle until it touches the surface of a substrate, forming a liquid bridge. If a substrate is chosen so that the sample wets the surface, a uniform filament emerges that breaks in a finite amount of time, driven by dominating capillary forces. For the present work, a DoS device was built in-house. Videos were captured at 1265 fps at a resolution of 800 pixels \times 600 pixels using a Phantom[®] V4.1 high-speed camera attached to a 130-mm extension tube and a 10x objective. Videos were processed using a custom-built MATLAB[®] code that tracked the diameter of the filament in time. In the present study, results from the DoS measurements were used as a comparison for the data collected using the PRIMER device.

2.4 Results & Discussion

2.4.1 Droplet Formation at the T-Junction

For the present study, a passive system was used to monitor the formation (T-junction) and breakup (cross-slot) of droplets as a means of characterizing the extensional properties of dilute and semi-dilute polymer solutions. For the droplet-breakup event to be isolated, droplets needed to be formed such that a droplet could break without being interfered by another droplet that was entering the cross slot. The spacing of droplets was achieved by adjusting the ratio of the continuous- and dispersed-phase flow rates. Here, the time spacing, t_d , is used to describe the spacing between droplets. To better control droplets breaking in the cross-slot, the droplet formation process was first assessed and compared to predictive models presented in the literature [6, 108, 109].

During the droplet-formation process, the emerging dispersed-phase inlet stream enters into the main channel, obstructing a large portion of the cross section and confining the continuous phase to the space at the walls of the channel. As reported in the literature, the “filling” of the main channel causes an increase in upstream pressure, inducing the “squeezing” of the dispersed phase by the surrounding continuous phase [6, 109]. As the neck of the dispersed phase is squeezed, droplet growth occurs on a time scale that is proportional to the dispersed-phase flow rate. At late times in the droplet-formation process, droplets break away from the dispersed-phase supply, and they are carried downstream into the cross slot.

For describing the appropriate “mode” of droplet-formation, the relative effects of viscous and capillary forces are important. The capillary number,

$$Ca = \frac{\mu_c U_c}{\sigma_{cd}}, \quad (2.9)$$

is introduced such that μ_c is the shear viscosity of the continuous phase, U_c is the velocity

of the continuous phase in the main channel, and σ_{cd} is the interfacial tension between the dispersed and continuous phases. For droplet formation occurring above a critical capillary number, $Ca_{cr} = 10^{-2}$, shear stresses are known to become important, and the droplet-formation process is said to operate in an “unbounded,” dripping regime [109, 110, 112]. In the present study, however, the majority of the droplets produced were “bounded” by the width and height of the main channel, indicating that capillary numbers were below this critical value. The capillary numbers that were evaluated were consistent with such observations. Predictive models for “bounded” droplet formation at a T-junction were thus considered.

Other interesting observations were noted for the formation of viscoelastic droplets at the T-junction. Depending on the concentration of PEO in a given sample, threads were formed that connected the newly-formed droplets to the dispersed-phase supply. As droplets were carried downstream, these threads would assume the well-known beads-on-a-string morphology [66, 118, 119]. Yet, as droplets continued to translate farther down the channel, the beads would merge, yielding lone satellite droplets. Studies on the evolution of multiple beads along viscoelastic threads have shown that coalescence can occur as a consequence of drainage, where a fluid drains from the connecting thread into the beads [118, 120]. Such observations were noted for the 5000-ppm stock solution, yet the formation of connecting threads was not observed for the other less-concentrated PEO solutions sampled.

In an attempt to estimate the flow rates required to achieve a given spacing between droplets, the predictive model presented by van Steijn et al. [6] was incorporated. This model describes the relationship between the size of the droplets formed and the flow rates given by

$$\frac{V}{hw^2} = \frac{V_f}{hw^2} + \alpha \frac{q_d}{q_c}, \quad (2.10)$$

such that V is the volume of the droplet, and q_d/q_c is the ratio of the dispersed- and continuous-phase flow rates [109]. The parameters V_f and α are fitting parameters that

depend on the geometry of the T-junction, including the ratios of the height and widths of the channels, h/w and w_{in}/w , as well as the curvature of the edge where droplet formation occurs, ϵ [6]. Equation 2.10 presents a linear scaling relationship initially presented by Garstecki et al. [109], originally developed for Newtonian fluids over a wide range of operating conditions that is independent of material parameters such as viscosity and interfacial tension. Although this relationship may differ for viscoelastic samples, it serves as a reasonable means for analyzing droplet formation of solutions in the present study [6,109].

To calculate the volume of the droplets from two-dimensional images, van Steijn et al. provided the relationship

$$V = hA \pm 2 \left[\frac{h}{2} \right]^2 \left(1 - \frac{\pi}{4} \right) l, \quad (2.11)$$

which describes a planar droplet such that

$$A = \pi \left[\frac{w}{2} \right]^2 + w(L - w) \quad (2.12)$$

is the top-view area and

$$l = \pi W + 2(L - w) \quad (2.13)$$

is the perimeter of the droplet [6]. To find how the parameters $V_f/(hw^2)$ and α differ for more concentrated viscoelastic samples, Figure 2.11 presents data collected using the 5000-ppm PEO stock solution dispersed into a 200-mPa·s silicone oil over a range of flow rates. The values for $V/(hw^2)$ were calculated using Equation 2.11. From the data, a linear relationship is observed between the size of the droplets and the ratio of the dispersed and continuous-phase flow rates. Fitting the data in Figure 2.11 using Equation 2.10, the values for $V_f/(hw^2)$ (the intercept) and α (the slope) were found to be approximately 1.4 and 2, respectively. According to the predictive model presented by van Steijn et al., for a system with geometry ratios of $h/w = 0.9$, $w_{in}/w = 1$, and $\epsilon \approx 0$, the parameters $V_f/(hw^2)$ and α should have values of roughly 1 and 2, respectively.

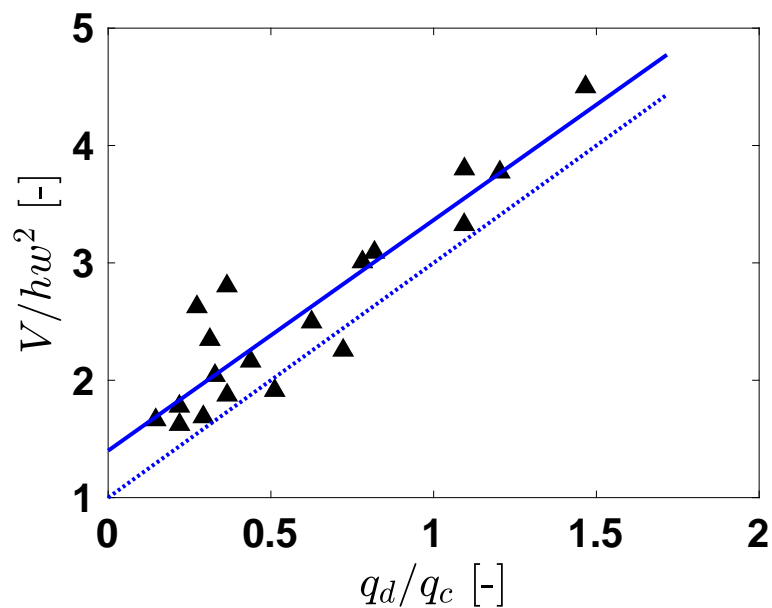


Figure 2.11: Droplet formation at a T-junction for a 5000-ppm PEO solution in 200-mPa·s silicone oil over a range of flow rates from 0.01 ml/hr to 1 ml/hr. The blue solid-line indicates a linear fit using Equation 2.10: $V/(hw^2) = V_f/(hw^2) + \alpha q_{disp}/q_{cont}$, where $V_f/(hw^2)$ and α were found to be 1.4 and 2, respectively. The blue dashed-line indicates the line predicted using the theoretical model presented by van Steijn et al. [6], where values for $V_f/(hw^2)$ and α have been evaluated to be approximately 1 and 2, based on the geometry of the T-junction.

Although the intercept was found to be slightly larger than what was expected from the model, these results are still within an acceptable range as a consequence of inherent errors in calculating the volume from a 2D image and the differences between the experimental setup and the assumptions made in the model. For example, the predictive model does not account for the presence of elastic stresses nor does it account for the viscosity ratio of the working fluids, both of which could influence the droplet filling and squeezing processes. Furthermore, although ε was assumed to be zero, any curvature in the T-junction edge could lead to deviations in the expected size of the droplets [6]. Interestingly, when Hunsy and Cooper-White [108] studied the effects of elasticity on the droplet formation process, increasing the continuous-phase flow rate decreased the drop size in a non-linear manner. Nevertheless, this study occurred in an unbounded “dripping” regime; whereas, the current study monitors droplets forming in a bounded “squeezing” regime.

Understanding how elasticity impacts the droplet formation process was necessary for having better control over the size and frequency of droplets entering the cross slot. Despite the results of the 5000-ppm PEO solution being in relatively good agreement with the predictive model, other observations revealed that elastic stresses can still impact the droplet-formation process. In the present study, the droplet formation of Newtonian and viscoelastic samples over a range of shear viscosities was monitored. As the viscosity of the GLY/DIW was increased, holding the continuous-phase constant, droplet formation proved more difficult to achieve. The formation of viscoelastic droplets, on the other hand, was similar for all of the PEO solutions tested. These observations are in agreement with linear stability analyses of viscoelastic jets as well as droplet-breakup experiments presented in the literature, where disturbances have been shown to propagate faster for viscoelastic samples than for Newtonian samples of the same zero-shear viscosities [24, 108, 121].

Although at lower viscosities the model proposed by van Steijn et al. [6] predicted the formation of Newtonian droplets at the T-junction, increasing the viscosity of the GLY/DIW solutions led to deviations from the model. For example, given the same flow criteria as

the lower viscosity samples, higher viscosity droplets would not form despite the model being material independent. These observations suggest that the ratio of the continuous- and dispersed-phase viscosities are important to the droplet-formation process. Although not considered by van Steijn et al., Garstecki et al. [109] have suggested that the increased viscosity of the dispersed phase could modify such scaling relations. Although further investigation could allow for the development of more robust predictive models, this topic is out of the scope of the present study.

To predict the time spacing between droplets, a custom-built MATLAB[®] code was used to monitor droplets as they moved across the channel. As such, the true time spacing between droplets was evaluated using two approaches: (1) by comparing the relative distance between two droplets in a given frame and (2) by evaluating the time required for two droplets to arrive at a given position along the main channel. The latter method was considered as a result of droplets that would form and enter the cross slot before a second droplet was produced. The time spacing between droplets was then compared to the predicted-filling period approximated for various flow conditions. The filling period was selected for comparison, as it involves the time required for the dispersed phase to enter into the main channel before being squeezed by the continuous phase. Additionally, this period can be predicted if V_f is known. Here, the filling period is evaluated as

$$k\Delta t_f = k \frac{V_f}{q_d}, \quad (2.14)$$

such that V_f is the fitted value approximated by the solid-line in Figure 2.11, and k is a fitting parameter that depends on the regime of droplet formation. Figure 2.12 presents the true time spacings versus the evaluated filling periods for the 5000-ppm PEO solution over a range of flow rates. The estimated filling periods were corrected by a factor of one-half, $k = 1/2$, for flow conditions where the continuous-phase flow rate was more than twice the dispersed-phase flow rate ($q_d/q_c \leq 0.5$). Without this correction, the filling time would

largely overestimate the time spacing for droplets in this range. As the continuous-phase flow rate was increased relative to the dispersed-phase flow rate, the incoming dispersed-phase was susceptible to being “forced” by the continuous phase into the main channel before fully filling the channel. Although the overall velocity of the droplets is known to influence whether droplets form in a dripping or in a squeezing regime, reflected by the capillary number, the present results reveal that the ratio of the flow rates may also influence the mechanism of the filling step. Overall, a good correlation exists between the time spacing and the amount of time necessary for a droplet to “fill” the channel. Thus, for a rough estimate of t_d , Δt_f^* was used such that

$$\Delta t_f^* = \begin{cases} 0.5\Delta t_f, & q_d/q_c \leq 0.5 \\ \Delta t_f, & q_d/q_c > 0.5. \end{cases} \quad (2.15)$$

Ultimately, by reducing the dispersed-phase flow rate, the time spacing between droplets entering the cross slot could be increased. Yet, to maintain the size of the droplets so that a breakup event could be observed in the cross slot (Figure 2.13), the ratio of the dispersed-continuous-phase flow rates were maintained. Lowering both flow rates also ensured that droplets were formed by the two-step filling and squeezing processes. For the present study, as long as the time scale of the droplet breakup in the cross slot was shorter than the time spacing between droplets entering the cross slot, a breakup event was considered to be isolated. Thus, lowering the flow rates helped to better control the droplet-breakup dynamics occurring downstream.

2.4.2 Droplet Breakup for Newtonian and Viscoelastic Fluids

After establishing the conditions required to form droplets at the T-junction, the next step was to explore the effects that viscous and elastic stresses play on the droplet-breakup

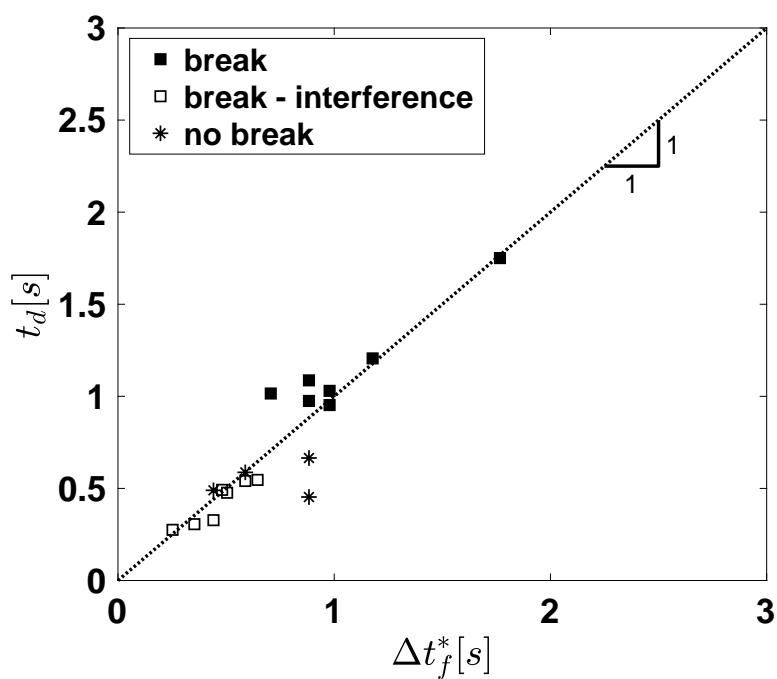


Figure 2.12: time spacing, t_d , and filling period, Δt_f^* , for 5000-ppm PEO droplets formed at a T-junction over a range of flow rates from 0.01 ml/hr to 1 ml/hr dispersed in 200-mPa·s silicone oil. The black dashed-line represents the line of equality between the abscissa and ordinate. The filled-squares represent droplets successfully split in the cross slot without interference. The unfilled squares represent droplets that split with interference from another incoming droplet. The star symbols represent droplets that did not break and that instead entered either outlet channel. For droplets to break without interference, larger time spacings were required.

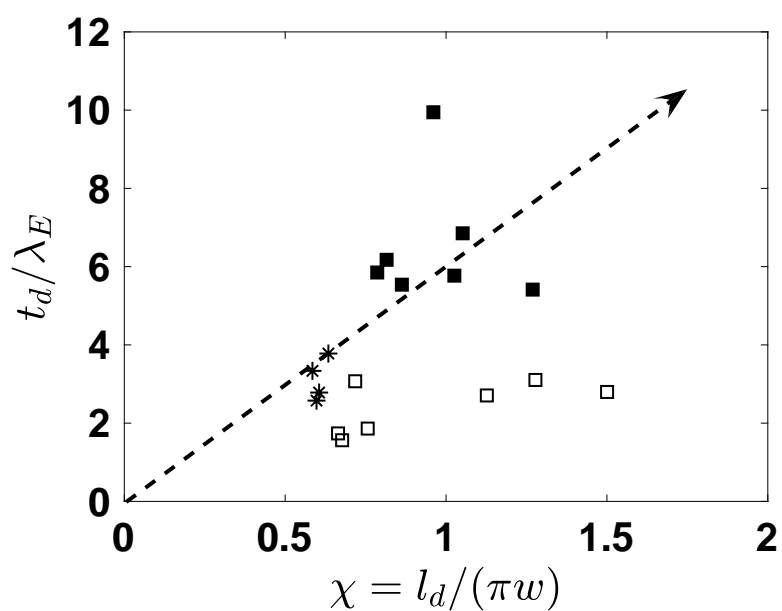


Figure 2.13: Criteria for the successful breakup of droplets in a cross-slot for a 5000-ppm PEO solution dispersed in a 200-mPa·s silicone oil over a range of flow rates from 0.01 ml/hr to 1 ml/hr. The time spacing of the droplets is normalized by the relaxation time of the dispersed phase and is plotted against the initial aspect ratio of the droplets, $l_d/(\pi w)$. The filled-squares represent droplets successfully split in the cross-slot without interference. The unfilled-squares represent droplets that split with interference from another incoming droplet. The star symbols represent droplets that did not break. For a successful breakup event to be observed, both the size and spacing of the droplets is important.

event occurring in the cross slot. For this aim, a number of experiments were performed that varied the ratio and magnitude of the flow rates as well as the types of continuous and dispersed phases that were examined.

As droplets enter into the cross-slot geometry, their shapes are distorted so that they elongated parallel to the outlet channels. Reaching the stagnation point, droplets either extend and break into two segments or remain intact, exiting one of the outlet channels. Conditions for when droplet-breakup events occur have been discussed extensively in the literature [24, 107]. Specifically, operating diagrams depicting breaking and nonbreaking droplets at T-junctions have been presented. In these diagrams, important parameters for droplets breaking include the capillary number, Ca , and the initial aspect ratio of the droplet, $\chi = l_d/(\pi w)$. Consistent with the Plateau-Rayleigh instability for the breakup of a cylindrical thread, an extended droplet can minimize its surface area by splitting. In agreement with what is reported in the literature, droplets in the present study were more likely to break at larger capillary numbers (higher flow rates) and having higher aspect ratios (longer droplets) [107]. Nevertheless, as previously described, controlling the time spacing between droplets was also critical in the current setup, further limiting the flow conditions for a successful breakup event (Figure 2.13).

Typical droplet-breakup profiles at the cross slot for Newtonian and viscoelastic fluids are presented in Figure 2.14. The main discrepancy between the two profiles is that the formation of a filament is clearly observed for the breakup of the viscoelastic droplet in Figure 2.14(b) and is not apparent for the Newtonian GLY/DIW solution in Figure 2.14(a). These observations are consistent with experimental observations for droplet breakup at a T-junction [24], where additional elastic stresses can aid in resisting the breakup process. Furthermore, for viscoelastic droplets, the well-known beads-on-a-string morphology was observed at late times in the breakup process [24, 66, 118–120]. Newtonian fluids, on the other hand, appeared to form satellite droplets with no noticeable connecting threads.

Monitoring the diameter of a droplet of the 5000-ppm PEO solution at a range of points

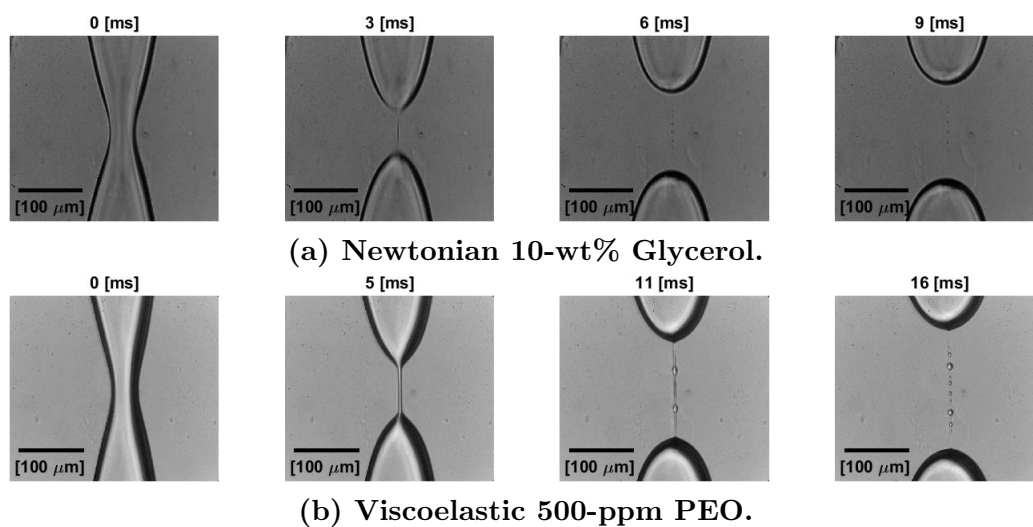


Figure 2.14: Droplet breakup of Newtonian and viscoelastic fluids in the cross-slot of the PRIMER device. At time $t=0$, capillary pressures initiate the droplet-breakup event. (a) A 10-wt% glycerol/water solution rapidly decays in time. Sattelite droplets are observed at late times, and depending on the viscosity of the glycerol/water solution, the number and size of these satellite droplets vary. (b) A 500-ppm PEO/water solution forms a cylindrical filament that decays exponentially in time. At late times, the well-known beads-on-a-string morphology is observed, and depending on the concentration of PEO, the size of the initial filaments and the structure of the beading patterns vary.

along the profile of the droplet (Figure 2.15), four distinct regimes were noted including (i) the early stretching and necking of the droplet as it reaches the stagnation point, (ii) a rapid decrease in the diameter driven by dominating capillary forces, (iii) an elastocapillary regime where the growth of elastic stresses compete with the capillary pressures driving the breakup process, and (iv) the formation of the beads-on-a-string morphology. The regime of interest for the present study is the elastocapillary regime (regime iii), where the elastic properties of a material can be extracted. The other three remaining regimes will be briefly described below.

At early times (regime i), a droplet is carried to the stagnation point by the continuous-phase fluid. As the droplet is aligned and stretched towards the outlet channels, the diameter of the droplet decreases, causing capillary pressures to grow within the droplet [107]. At a critical diameter, dependent on the material properties of the fluid, a rapid breakup event is initiated (regime ii). The factors controlling these early-time dynamics include the flow rates and the relative zero-shear viscosities of the continuous- and dispersed-phase fluids.

Over the first three regimes, results, as exemplified in Figure 2.15, appear insensitive to the vertical position along the filament where a measurement is taken. The fourth regime, however, is apparent by the “fanning” of the decay profile, as droplets or “beads” of alternating sizes are formed. Iterated stretching is known to occur in the late-time thinning dynamics for finitely-extensible polymer solutions, where the neck connecting a thread to a primary drop becomes unstable [118]. This process leads to the formation of secondary droplets, which, in turn, can lead to the formation of higher generation droplets. In the present study, the size and generation of bead growth depended on the concentration and type of polymer. Although beads-on-a-string instabilities have been extensively studied both numerically [66, 119] and experimentally [118] for capillary breakup experiments, few studies have observed how a viscous outer fluid impacts the iterated-stretching process. Christopher and Anna [24], for example, observed the formation of the beads-on-a-string instability in their investigation of droplets splitting at a T-junction in a viscous silicone

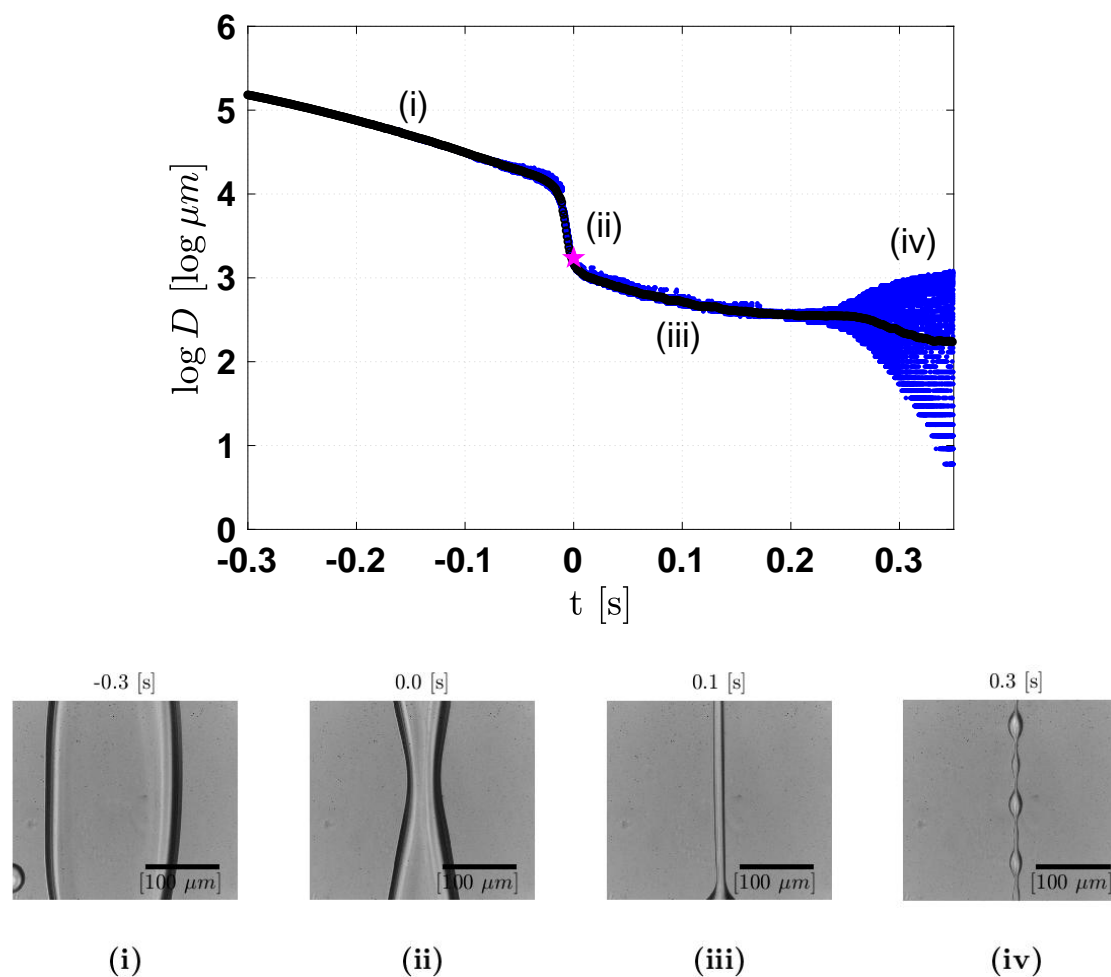


Figure 2.15: Diameter decay profile for a droplet of 5000-ppm PEO stock solution at a range of points along the filament profile. Four distinct regimes are noted including (i) the early stretching and necking of the droplet as it reaches the stagnation point, (ii) a rapid decrease in the diameter caused by dominating capillary forces, (iii) an elastocapillary regime where the growth of elastic stresses compete with the capillary pressures driving the breakup process, and (iv) the formation of the beads-on-a-string morphology. The initial time at $t=0$, is the time at the end of regime (ii) in which a filament forms. The natural logarithm of the diameter at this point is highlighted on the plot.

oil. Although the phenomena of iterated stretching can prevent the elastocapillary regime of interest, Christopher and Anna used the exponential thinning of the secondary filaments to extract a characteristic relaxation time of the polymer solution being tested [24].

In the present study, the regimes iii and iv are found to be unique to viscoelastic samples, and Newtonian fluids did not appear to form appreciable filaments over the range of the shear viscosities that were tested.

2.4.3 Comparison of the DoS and PRIMER techniques

To validate the use of a droplet-breakup event for extracting extensional measurements, a 5000-ppm PEO solution was tested using both the dripping-onto-a-substrate (DoS) and droplet breakup at a cross-slot (PRIMER) techniques. The results of ten droplet-thinning profiles using PRIMER were then averaged and compared with the evolution profiles of liquid filaments formed using the DoS technique. A more concentrated polymer solution was selected to ensure that a comparison could be made using both techniques.

In anticipation of leveraging Equation 2.1, the natural logarithm of the resulting diameter decay profiles are plotted in Figure 2.16. Both the DoS and the PRIMER techniques show similar trends in filament-thinning profiles. The initial diameter at $t = 0$, D_0 , is the diameter of the initial filament formed at the end of regime ii. For the DoS method the initial filament diameter was orders of magnitude larger than the filaments formed in the cross slot. The differences in characteristic length scales are reflected in the vertical shift in diameter plotted in Figure 2.16. In addition, the filament-thinning and breakup process was nearly three times longer in the DoS technique than in the PRIMER, allowing for the dynamics of interest to be more easily captured in the former at 1265 fps. One argument for these observations is that the small length scales in the cross slot necessitate small time scales associated with the droplet-breakup event. Additionally, the dashed line in Figure 2.16 represents the transition into the beads-on-a-string regime, where an instability causes the

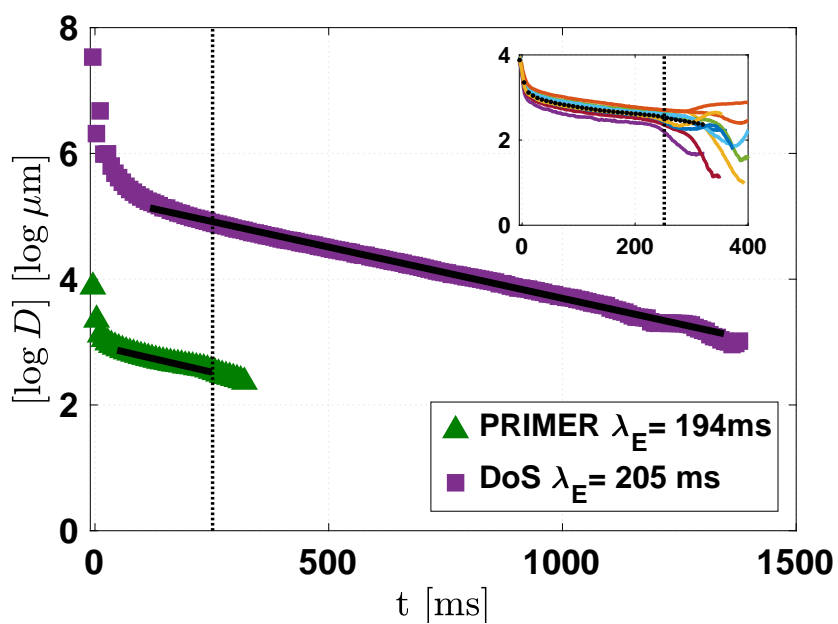


Figure 2.16: A comparison of diameter-decay profile for a 5000-ppm PEO stock solution using PRIMER and DoS techniques. For the PRIMER results (green triangles), a 200-mPa·s silicone oil was used as the continuous phase fluid. The solid lines represent the linear fits in the elastocapillary regime of interest, where relaxation times can be extracted.

formation of beads along the filament. The onset of the beads-on-a-string instability may obscure the elastocapillary regime of interest, and it will thus be investigated in more detail below.

To extract information from the diameter-decay profiles for both PRIMER and DoS, an analysis is performed in the same manner as in CaBER experiments. At this point, subtle differences in the procedure for the DoS and the PRIMER techniques from the standard CaBER procedure need to be explicitly described. The extensional techniques presented are not completely shear free, and they can be sensitive to the shear history. In the DoS technique, rather than applying a finite step-strain to a material, the sample continues to wet the surface of a substrate as it thins and breaks. Similarly, in the PRIMER device, the filament continues to stretch as it enters the outlet channels of the cross-slot geometry. These observations may impact how the characteristic relaxation times can be extracted from the filament decay profiles. Nevertheless, when exponential thinning of the filament occurs, the relaxation time can generally be extracted according to Equation 2.1. Assuming that the dominant forces in this regime are interfacial tension and elastic stresses, the strain rate and transient extensional viscosity may also be evaluated.

For the present experiments, despite the 5000-ppm fluid being concentrated, the natural logarithm of the diameter decay profiles observed in Figure 2.16 appear to have linear elastocapillary regimes, highlighted by the solid-lines. The characteristic relaxation times were evaluated using the slopes of the fitted curves, where the slope, m , is inversely proportional to the characteristic relaxation time ($m = 1/(3\lambda_E)$). When evaluated, the relaxation times from the two techniques are in good agreement, with a relaxation time of 204 ms found using the DoS trials, and the PRIMER, a relaxation time of 194 ± 49 ms found using the PRIMER technique.

Although the results of the DoS and PRIMER techniques are consistent, testing how sensitive the elastocapillary regime is to varying experimental conditions is necessary to establish the robustness of the PRIMER technique. Since droplet breakup in a cross-slot

is not well-defined in the literature, significant interest in how changing parameters such as the flow rate, the dispersed-phase fluid, and the continuous-phase fluid may impact the droplet-breakup event exists. Furthermore, since the splitting of droplets could serve as a means of characterizing low-viscosity elasticity, understanding the limitations of such a technique is critical.

2.4.4 Flow-Rate and Continuous-Phase Sensitivity

To explore how varying flow conditions impacted the dynamics of droplet breakup in a cross-slot, droplets of the 5000-ppm PEO stock solution were tested using a variety of continuous-phase oils ranging from 30 to 500 mPa·s at flow rates varying from 0.01 and 1 ml/hr. Figure 2.17 contains a plot of the raw diameters versus time for droplets splitting in the 200 mPa·s silicone oil. As a first observation, the elastocapillary regime (regime iii) appears relatively unaffected by the flow conditions compared to early times (regime i), where the stretching of the droplet occurs. As the overall flow rates in the cross slot are increased, the drag acting on a droplet is more substantial, which causes the droplet to elongate more rapidly, reflected by the steepening of the slope at early times in Figure 2.17. In terms of the elastocapillary regime, the evaluated relaxation times fall within the same order of magnitude as the DoS trials (Table 2.2).

Table 2.2: A summary of the continuous- and dispersed-phase flow rates tested for the 5000-ppm stock solution dispersed in the 200-mPa·s in the PRIMER.

\dot{V}_c [ml/hr]	\dot{V}_d [ml/hr]	λ_E [ms]
0.13	0.04	170
0.13	0.02	240
0.73	0.04	180
0.73	0.03	150
0.05	0.01	220

Since the length of the initial filament [$O(10 \mu m)$] is much less than the characteristic length of the cross slot, the elastocapillary regime is assumed to be less affected by global

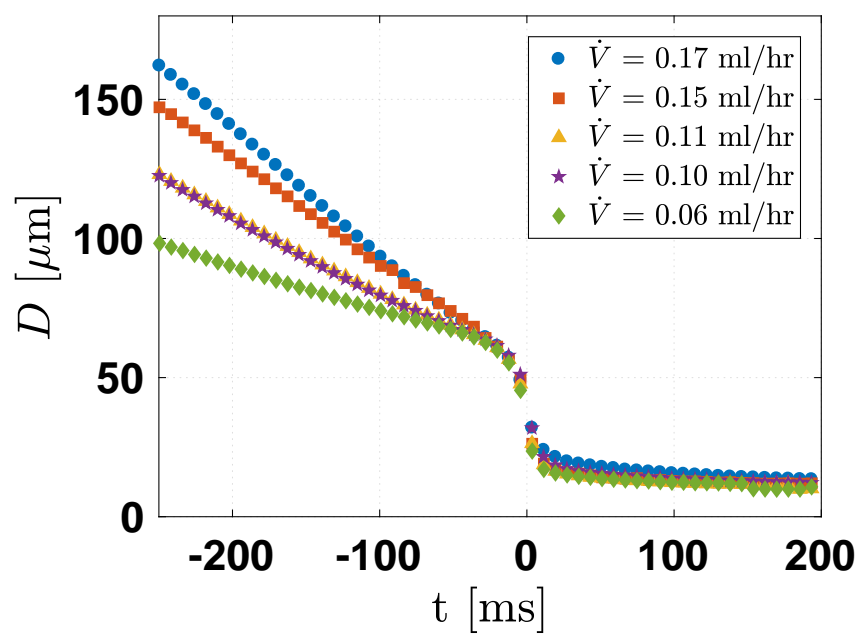


Figure 2.17: Plot of diameter versus time for varying flow rates for stock solution of 5000-ppm PEO dispersed in 200-mPa·s silicone oil. The slope of the initial viscous-drag regime is increased as the overall flow rates in the device are increased.

flow conditions. To see if this assumption is valid, the size of the droplets, a function of q_d/q_c , and the capillary number, a function of U_c and μ_c , were varied, and the resulting relaxation times were again evaluated using Equation 2.1. Figure 2.18 contains the results for these trials. The filled-black markers represent varying continuous-phase viscosity at a fixed flow ratio, $q_{disp}/q_{cont} = 0.8$.

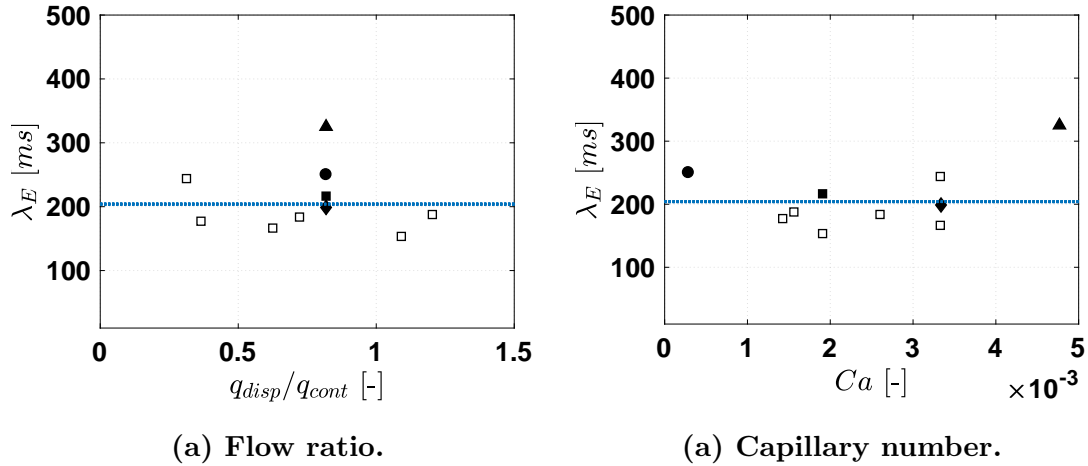


Figure 2.18: Results for trials varying the size of the droplets, a function of q_d/q_c , and the capillary number, a function of U_c and μ_c using the 5000-ppm PEO dispersed in 200-mPa-s silicone oil. (a) The extensional relaxation time is plotted versus the ratio of the dispersed- and continuous-phase flow rates. (b) The extensional relaxation time is plotted versus the capillary number. The filled-black markers represent varying continuous-phase viscosity at a fixed flow ratio, $q_{disp}/q_{cont} = 0.8$. The blue-dotted lines represent the relaxation time characterized in the DoS trial.

Unlike what was observed in the passive breakup of droplets at a T-junction, the relaxation times that were characterized did not appear to be greatly influenced over a variety of experimental conditions tested. Furthermore, although some variability existed, no systematic cause for the variability was noted, and all of the approximate relaxation times fell within the range of the values calculated by the DoS technique. For droplet breakup at a T-junction, Christopher and Anna [24] found relaxation times to be influenced by the capillary number and initial aspect ratio. In those experiments the initial capillary numbers were above 10^{-2} , whereas in the present experiments, the capillary numbers were maintained

below this value. When capillary forces dominate over viscous stresses, we believe that the breakup event will be less influenced by the surrounding continuous-phase flow.

2.4.5 Viscoelasticity of the Dispersed-Phase

After confirming that the breakup dynamics at higher concentrations of polymer were relatively repeatable and consistent, the dynamics at lower concentrations of polymer were explored. Figure 2.19 presents data collected for dilutions of the stock solution at 10, 50, 100, and 500 ppm. From the data at lower concentrations of polymer, filament formation is observed to be less pronounced. The lowest concentration in which a filament was observed was around 50 ppm. Yet, the number of frames was too low to fit a decay profile at concentrations below 500 ppm. At 500 ppm, the relaxation time measured was approximately 8 ms, in agreement with what has been observed in the literature [3]. A possible solution for monitoring less concentrated samples could be to employ a better camera, capturing a greater number of frames per second. This solution would allow for more data points to be collected over a given breakup period.

When going to lower concentrations, the initial size of the filament decreased and the beading profiles were altered, as seen in Figure 2.20. Furthermore, the “strings” connecting the beads were challenging to discern as their diameter size neared the limits of optical detection. In the paper by Christopher and Anna [24], the self-thinning of these connecting strings was used to measure the properties of a dispersed-phase sample. As was found with the current setup, these secondary and tertiary filaments were too difficult or impossible to track.

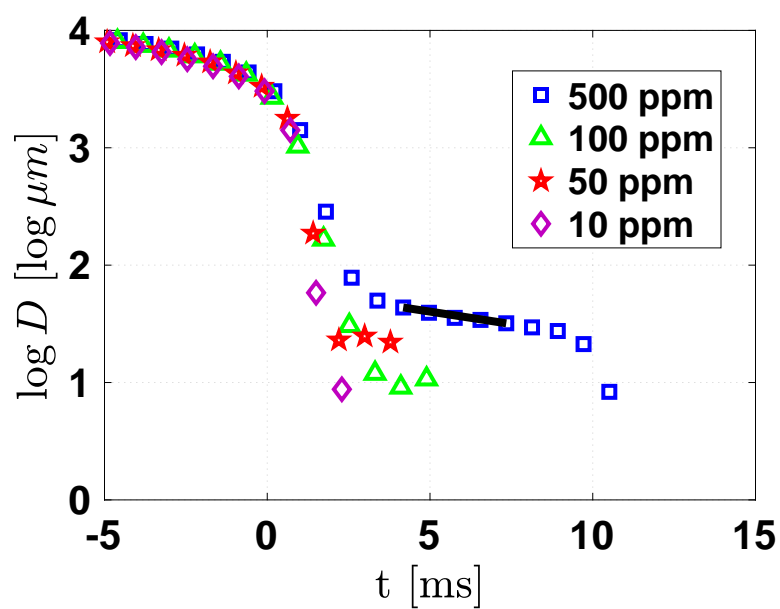
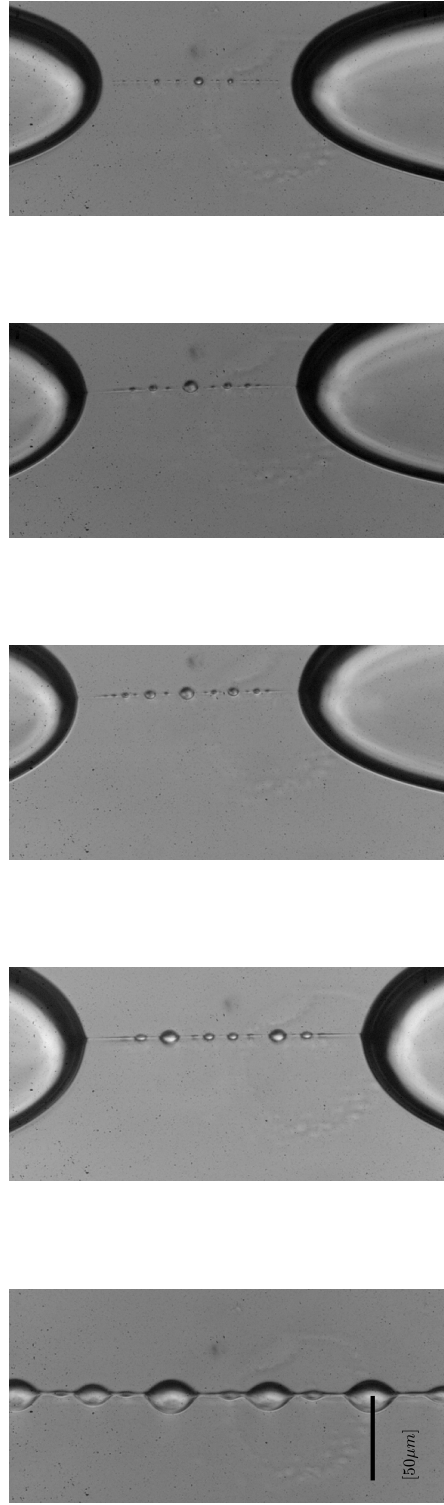


Figure 2.19: Diameter-decay profiles for filaments at concentrations of 10, 50, 100, and 500 ppm PEO. The natural logarithm of the diameter is plotted versus time. Only the 500-ppm solution had a elastocapillary regime that could be fit.



(a) 5000-ppm PEO. (b) 500-ppm PEO. (c) 100-ppm PEO. (d) 50-ppm PEO. (e) 10-ppm PEO.

Figure 2.20: Beading profiles for filaments of PEO at (a) 5000, (b) 500, (c) 100, (d) 50, (e) 10 ppm PEO dispersed in 200-mPa-s silicone oil. When going to lower concentrations, the initial size of the filament decreased and the beading profiles were altered.

2.5 Conclusions & Future Work

In the present study, droplet breakup in the cross-slot of a microfluidic device was presented as a means of characterizing weakly-viscoelastic fluids. Since the length scales associated with such devices are on the order of a few microns or less, the effects of elasticity are thought to be more pronounced. To successfully break droplets in a cross-slot geometry, a time spacing parameter was considered. Although the effects of elasticity were clearly observed for a 5000-ppm PEO sample, with a droplet evolution profile similar to that captured using the DoS technique, attempts to extract a characteristic relaxation time proved unsuccessful at more dilute concentrations.

In some instances, the time scale associated with the droplet-breakup event was too rapid to be captured using the current camera setup. For filaments that form and break on a time scale that is on the order of a millisecond or less, a more capable camera is needed to collect enough data points to fit the elastocapillary regime. Additionally, at lower concentrations of PEO, the onset of beads-on-a-string was observed to conceal the elastocapillary regime. To address this issue, a proper study of the onset of beads-on-a-string in the cross-slot geometry is required. As discussed by Bhat et al. [119], for systems with larger intrinsic Deborah numbers and Ohnesorge numbers, no beads should be observed. In theory, by reducing the length scale of the system, the values of both of these parameters should increase. Nevertheless, the numerical studies presented by Bhat et al. did not involve a viscous outer fluid. A deeper investigation into how the viscous outer fluid influences the onset of beads-on-a-string is thus imperative for improving the design of the device.

Although much of the present work draws attention to the elasticity and elastocapillary numbers, Clansen et al. [20] discuss that for an elastocapillary number greater than unity ($Ec > 1$) the filament thinning process may not be possible if a minimum concentration is not achieved. In his paper, the minimum concentration requirement for observing any

viscoelastic effects was found to be

$$c_{min} = \frac{3}{2} \frac{M_w \eta_0}{RT \lambda_z L^2}, \quad (2.16)$$

where M_w describes the molecular weight of the polymer, η_0 describes the shear viscosity of the solvent, R is the ideal gas constant, T is the temperature, λ_z is the Zimm longest relaxation time of the polymer, and L^2 describes the finite extensibility of the polymer. Below this concentration, the fully extended polymer carries less stress than the solvent, causing viscous stresses to play a greater role than elastic stresses in resisting filament thinning. For the solutions tested in the current setup, however, distinct beads-on-a-string profiles were observed for the breakup of droplets with small amounts of polymer versus droplets with no polymer at all.

Aside from smaller length scales, additional benefits of the current setup are smaller sample sizes and an outer continuous-phase fluid that is not air. For samples that are volatile or easily degraded in air, such a setup is highly desirable. Furthermore, the current technique employs theory that is well-understood on the macro-scale, employing a CaBER-like system.

Still, differences between the CaBER and PRIMER are important to distinguish. For example, the CaBER applies a finite step-strain to a material whereas the PRIMER continues to stretch a sample as the filament thins. Thus, the assumption of a “self-thinning” filament may not hold if the time scale of breakup is less than the time scale of the external forcing. In this regard, the PRIMER may be more similar to the FISER than the CaBER. To make the cross-slot device more similar to a CaBER, a possible improvement could be to employ a more advanced pumping systems to actively break droplets. Such a system could also be explored to create droplets on demand, removing the time spacing concern. A sample pump design for the PRIMER is presented in Figure 2.21.

Other improvements to the cross-slot geometry could make the device operate more like a

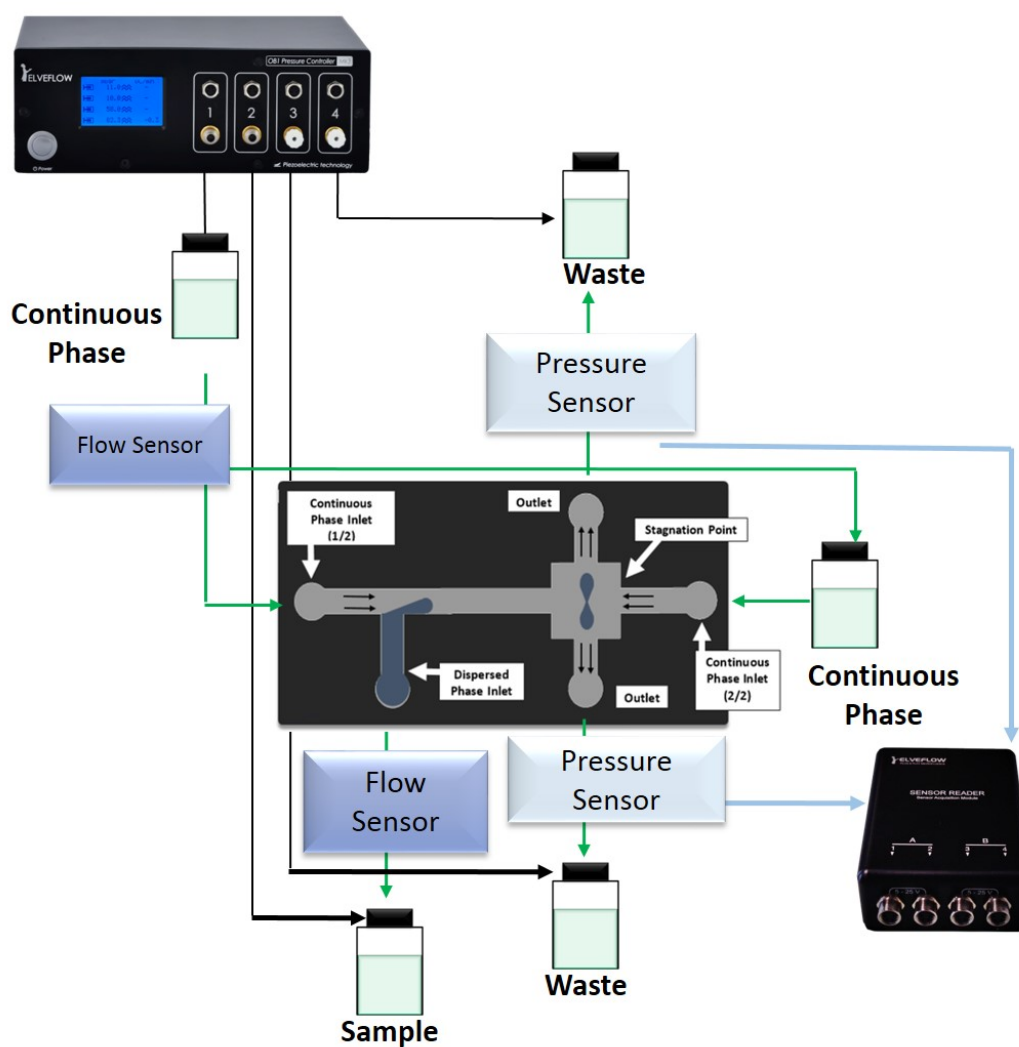


Figure 2.21: A sample pump design for the PRIMER. Two flow sensors are used to accurately monitor the flow rates into the device. Pressure sensors at the waste streams can be used to control the droplet-splitting event.

CaBER or more like a FISER (Figure 2.22). For a CaBER design, a droplet would rapidly extend and then remain still to allow for the self-thinning of the filament. To passively achieve such a process, the droplet could enter into a small cross section that opens into an expansive reservoir, lowering the flow rate out of the device (Figure 2.22(a)). For a FISER design, a filament would be extended at a constant strain rate. To passively achieve such a process, the shape of the cross-slot geometry could be modified to ensure a constant strain rate (Figure 2.22(b)).

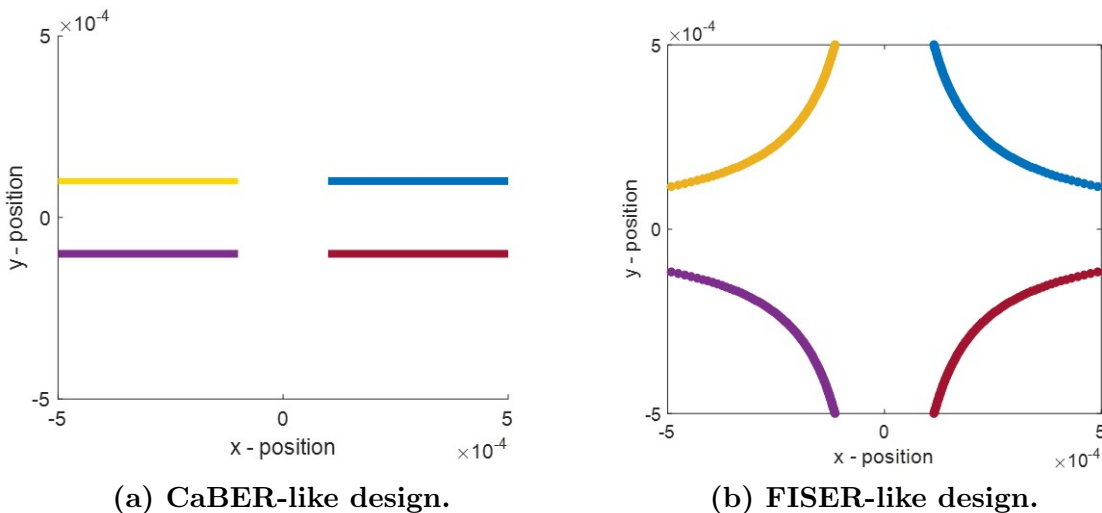


Figure 2.22: Sample geometry designs for the PRIMER. (a) CaBER-like design in which a droplet is rapidly extended and then remains still to allow for the self-thinning of a filament. (b) FISER-like design where a filament is extended at a constant strain rate.

To ensure that the velocity profiles are achieved by the device geometry, flow-field visualization techniques, such as the addition of TiO_2 tracer particles, can be employed to observe flow streamlines within the device. Although cross-slot geometries have been previously used to observe the effects of elasticity in an extensional flow, they have only been used to observe single-phase flow [38]. Such techniques would provide insight on the interaction between the continuous and dispersed phases in the droplet-breakup event.

2.6 Acknowledgements

The authors would like to thank Aleesha Liedtke, Anika Todt, Katie Moreno, Shelley Haug, Dr. Skip Rochefort, and Dr. Adam Higgins for their contributions to this work. In addition, the authors would like to thank Oregon State University's (OSU) Johnson Summer Internship program and the Saturday Academy's Apprenticeships in Science and Engineering (ASE) program for providing funding and interns to assist in this work. KAM would also like to thank the OSU Diversity Pipeline Fellowship for funding.

Chapter 3: Handheld Extensional Rheometry with a Mobile Device

Submitted to Experiments in Fluids

3.1 Abstract

The on-site characterization of complex fluids is important for a number of academic and industrial applications. Consequently, a need exists to develop portable rheometers that can provide in-the-field diagnostics and serve as tools for rapid quality assurance. With the advancement of smartphone technology and the widespread global ownership of smart devices, mobile applications are attractive as platforms for rheological characterization. The present work investigates the use of a smartphone device for the extensional characterization of a series of Boger fluids composed of glycerol/water and poly(ethylene oxide), taking advantage of the increasing high-speed video capabilities (currently up to 240 Hz capture rate at 720p) of smartphone cameras. We report a noticeable difference in the characterization of samples with slight variations in polymer concentration and discuss current device limitations. Potential benefits of a handheld extensional rheometer include its use as a point-of-care diagnostic tool, especially in developing communities, as well as a simple and inexpensive tool for assessing product quality in industry.

3.2 Introduction

Over the past 10 years, smartphone applications have emerged as utilities that can positively benefit people's lives both at home and in the workplace. Smart devices provide information by employing built-in sensors to track position, motion, and environmental conditions such

as ambient temperature and pressure. Furthermore, newer smart devices are equipped with high-speed video capabilities that can be used to optically monitor systems. Aside from the plethora of health-care and educational applications that exist, smartphones are being utilized both in the field and in the laboratory. For example, these devices have been used in agricultural fieldwork to monitor crop and produce readiness [122], demonstrated capable of flow visualization using particle image velocimetry (PIV) [123], and integrated with a single-ball lens microscope for infertility screening [124].

By modifying existing experimental techniques, smart devices have the capacity to serve as inexpensive, portable, and multi-purpose alternatives to instruments commonly found in the field. For these reasons and the present need for more robust rheological techniques, smartphones are attractive as tools for rapid, on-site rheological characterization. The present work investigates the viability of a smartphone camera for performing rheological measurements, specifically focusing on measuring the extensional properties of Newtonian and viscoelastic fluids.

3.2.1 Extensional Rheology

One common example of an extensional diagnostic tool is the spinnbarkeit test (Figure 3.1). Taking a sample of saliva between one's thumb and pointer finger, or between two glass slides, and subsequently stretching the sample until it breaks, an individual can identify if he or she is sufficiently hydrated, depending on the "stringy" quality of the saliva. Similar qualitative tests are performed in the field and in industry, and developing a simple and inexpensive means of extracting quantitative information from these tests is desirable [125, 126] and the goal of the present research.

Unlike shear flows, extensional flows more readily uncoil flexible macromolecules, which can result in extensional thickening, noticeably altering a fluid's flow response. This phenomena is observed as the "stringy" or "tacky" nature of a fluid as it is stretched. When

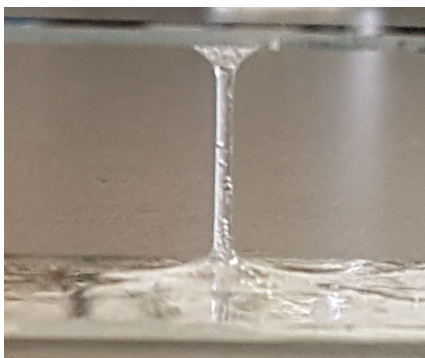


Figure 3.1: Saliva spinnbarkeit test performed by stretching saliva between two glass slides and observing the formation and breakup of the resulting filament as the slides are pulled apart.

undergoing an extensional deformation, small amounts of macromolecule that are added to a Newtonian solvent, such as the enzyme amylase in human saliva, can resist breakup relative to the Newtonian solvent alone, despite the solvent and the solution having zero-shear viscosities that are on the same order of magnitude. Thus, when stretched between two fingers, saliva will often form a persistent filament, whereas water will not. Since small changes in molecular weight, structure, and concentration of polymer can affect how a sample will respond in extension, extensional rheometry can serve as a powerful tool for quality control.

Knowing the extensional properties of a fluid is not only imperative for processing operations, such as jetting, spinning, and coating that have predominantly extensional modes of deformation, but also to medical communities for examining biological fluids, such as human saliva and synovial fluid (hyaluronic acid) in our joints, that have extensional viscosities that serve essential functions in our bodies [127,128]. Thus, despite shear rheometry being the more commonly used characterization approach, the need for extensional characterization is certain, having implications in the monitoring of product quality, in making optimal processing and design decisions, and in aiding in point-of-care diagnostics.

3.2.2 Capillary Breakup Extensional Rheometry

For assessing the extensional properties of complex fluids, samples are often measured using commercially available filament stretching rheometers. One such device is the capillary breakup extensional rheometer (CaBERTM) [41, 53]. Capillary breakup extensional rheometry works by applying a uniaxial extensional step-strain to a sample that is initially loaded between two circular plates. As the sample is stretched, an unstable filament is formed that thins and subsequently breaks under the action of capillary forces. The breakup process is monitored using either a laser micrometer and/or a high-speed camera at the filament's mid-point. From the diameter decay profile, information can be gained on the presence of elasticity and the material properties of a given sample.

The experimental and theoretical work behind the CaBER was first presented by Entov & co-workers [39, 65] and further developed by a number of contributors [3, 25, 41, 52, 82, 98, 129]. Reviews of filament-stretching rheometry of complex fluids and the elasto-capillary thinning and breakup of complex fluids are provided by McKinley and co-workers [40, 130]. The force balance describing the diameter decay profile as a function of time, $D(t)$, for the stretching of a idealized cylindrical filament with a radius that is independent of the position in the z -coordinate is given as

$$3\eta_s \left(\frac{-2}{D(t)} \frac{dD(t)}{dt} \right) + (\tau_{zz} - \tau_{rr}) + \frac{2\sigma}{D(t)} = \frac{4F_z}{\pi[D(t)]^2}, \quad (3.1)$$

where η_s is the shear viscosity of the Newtonian solvent, σ is the surface tension of the sample, $(\tau_{zz} - \tau_{rr})$ is the elastic contribution to the normal-stress difference, and F_z is the tensile force acting on the sample [65, 83, 131]. To solve Equation 3.1, a constitutive model must be assumed for the polymeric contribution to the normal-stress term.

Setting the normal-stress term equal to zero and neglecting end effects for Equation 3.1, Newtonian fluids in a capillary breakup experiment are evaluated to have filaments that decay linearly in time. Such processes have been well developed in the literature [52, 57, 61,

64]. From the slope of this decay profile, one can determine either the surface tension or the shear viscosity of the sample, if the other variable is known.

For viscoelastic fluids, the filament-thinning and breakup process includes three distinct regimes, caused by competing viscous, elastic, and capillary forces. At early times when the elastic stress contribution is small, and viscous stresses dominate, the decay profile will appear linear in time. However, as elastic stresses grow, the thinning filament will decay nonlinearly. Finally, not considered here, late-time dynamics are governed by the finite extensibility of the polymer. The focus of the present work is the elasto-capillary regime, where the first normal-stress difference is balanced by the capillary pressures driving the breakup process, $((\tau_{zz} - \tau_{rr}) \approx -2\sigma/D(t))$. For the upper convected Maxwell model, the form of the solution in this regime is an exponential,

$$\frac{D(t)}{D_1} = \left[\frac{GD_1}{4\sigma} \right]^{1/3} \exp \left[-\frac{t}{3\lambda_E} \right], \quad (3.2)$$

such that λ_E describes the characteristic relaxation time of the sample in extension, D_1 is the diameter of the sample immediately after it has been stretched, and G describes the elastic modulus of the filament [65].

Since strain rate cannot be controlled using the CaBER technique, to compare the extensional and shear properties of a fluid, results are often expressed using a transient apparent Trouton ratio that is defined as

$$Tr(\epsilon) = \frac{\eta_{E,app}(\epsilon)}{\eta_0}. \quad (3.3)$$

Here, ϵ is the Hencky strain, $\eta_{E,app}$ is the apparent extensional viscosity, and η_0 is the zero-shear viscosity. For a Newtonian fluid in uniaxial extension, the Trouton ratio is shown to be a constant of three ($Tr = 3$). For a viscoelastic fluid, however, the extensional viscosity can be orders of magnitude larger than the shear viscosity, yielding a Trouton ratio that is much greater.

The present research explores a number of methods for performing extensional characterization using a smartphone device with the overarching goal of making progress towards inexpensive and robust techniques for rapid, on-site rheological characterization.

3.3 Experimental Verification

3.3.1 Materials & Test Solutions

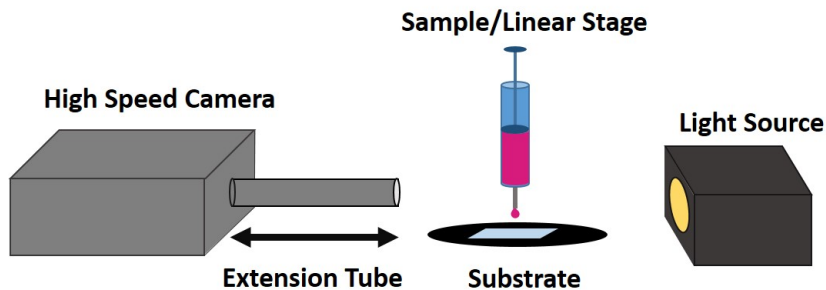
In the present work, a smartphone (Apple iPhone 6TM) was used to monitor the diameter decay profiles of four Boger and three Newtonian fluids. Boger fluids were created from a stock solution of aqueous 0.5 wt% poly(ethylene oxide) (PEO), deionized water (DIW), and glycerol (GLY) at the dilutions listed in Table 3.1. All solutions were prepared at room temperature and allowed to equilibrate for 48 hours prior to use. The stock solution of aqueous PEO was made by dissolving Dow Chemical Company POLYOXTM WSR 303 (MW = 7×10^6) in DIW, and it was stored in an amber glass bottle under nitrogen. All Boger fluids contained roughly 55.8 wt% glycerol and 44.2 wt% DIW. Three Newtonian solutions of varying shear viscosity were also selected for validation and to test device limitations.

Shear characterization was performed using a TA Instruments AR-G2 rotational rheometer with a titanium 60-mm cone upper geometry and Peltier plate lower geometry. Flow-sweep data confirmed that the Boger fluids had similar zero-shear viscosities (Table 3.1) and did not appear to shear thin over the range of shear rates tested (5 to 500 s⁻¹). Surface tension measurements were performed using a Krüss K10T tensiometer fitted with a du Noüy ring, and results are listed in Table 3.1.

Table 3.1: Composition and physical properties of test fluids.

No.	Composition	η_0 [mPa·s]	σ [mN/m]	Captured*
Solvent	55.8 wt% GLY	6.87	67.6	No
1	20 ppm PEO	9.17	58.7	Yes
2	40 ppm PEO	8.24	57.6	Yes
3	110 ppm PEO	9.03	57.0	Yes
4	660 ppm PEO	21.2	56.6	Yes
5	Silicone Oil	200	21.1	No
6	Silicone Oil	350	21.1	No
7	Silicone Oil	4870	21.4	Yes

* Filament decay successfully captured by smartphone camera



(a) Dripping-onto-Substrate (DoS).

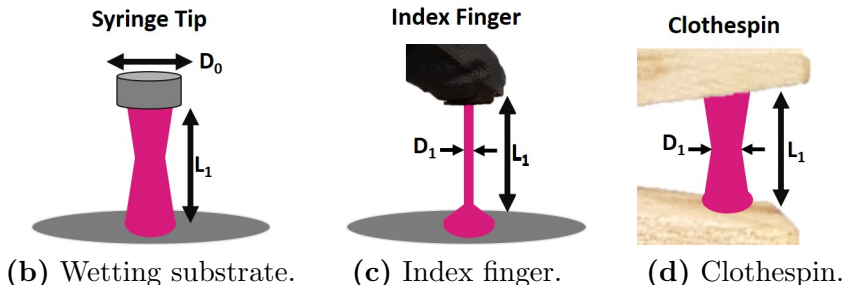


Figure 3.2: Capillary-breakup techniques for characterizing the extensional properties of fluids, with relevant dimensions including D_0 , D_1 , and L_1 . (a) A schematic of the DoS technique adapted from Dinic et al. [3]. (b) The thinning and breakup of a filament by allowing a sample to wet the surface of a substrate (DoS). (c) The formation of a filament using one's index finger by placing a sample on a glass substrate and stretching the sample to a set height. (d) The formation of a filament using a clothespin by placing a sample between the prongs of a wooden clothespin and stretching the sample to a set height.

3.3.2 Dripping-onto-Substrate (DoS)

After preparation, Boger fluid samples were evaluated using the dripping-onto-substrate (DoS) technique first presented by Dinic et al. [3,43]. Earlier dripping techniques have also been presented in the literature [81]. Similar to the CaBER, this technique uses capillary breakup to evaluate the extensional properties of a sample by slowly dispensing the sample from the tip of a needle until it touches the surface of a substrate to form a liquid bridge. If a substrate is chosen so that the sample wets the surface, a uniform filament will develop that breaks in a finite amount of time, driven by dominating capillary forces. For the present work, a DoS device was built in-house with a schematic depicted in Figure 3.2(a-b). Videos were captured at 1265 fps at a resolution of 800 pixels \times 600 pixels using a Phantom[®] V4.1 high-speed camera attached to a 130-mm extension tube and a 10x objective. Videos were processed using a custom built MATLAB[™] code that tracked the diameter of the filament in time. Results from the DoS measurements were used as a comparison for the data collected using the smartphone camera.

3.3.3 Smartphone Protocol

For the smartphone trials, two techniques were used to provide an initial step-strain to the material. The techniques performed were selected based on material attainability and cost considerations. In the first technique, a small amount (25-30 μ l) of sample was distributed on a glass slide, where it was subsequently pulled to a set height using the tester's index finger (Figure 3.2(c)). Latex gloves were worn to protect the tester and to prevent contamination to the sample. In the second technique, a small amount of sample was placed in-between the prongs of a wooden clothespin, where the sample was stretched by pressing and releasing the prongs of the pin (Figure 3.2(d)). To provide stability, both methods were performed on solid surfaces with the smartphone positioned no more than 70 mm from the sample. The smartphone was positioned directly on the table with the camera facing the sampling

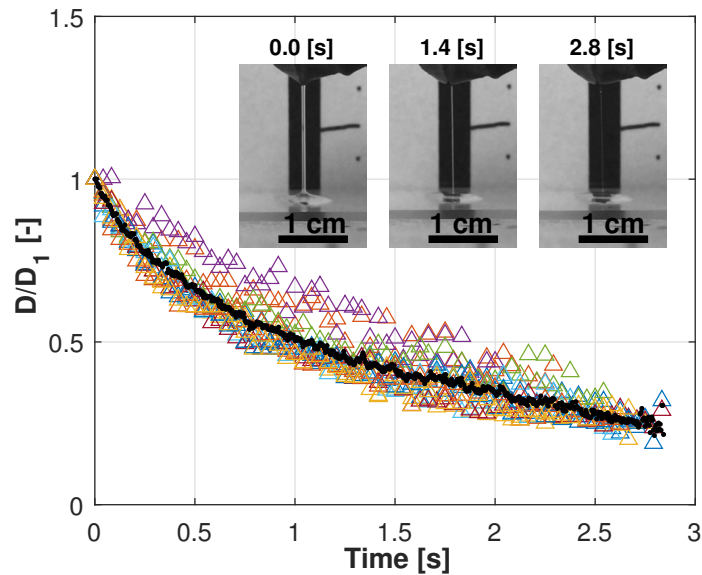
region. Details regarding the camera's specifications are included below. Care was taken so that both the camera and the sample were held as steady as possible.

Once extended, a sample's diameter decay profile was recorded at 240 fps, capturing frames at 1280 pixels \times 720 pixels HD resolution using a slow-motion setting. A square grid with 0.5-cm markings was placed in the background to serve as a measurement reference. Additionally, a solid-black background helped to provide contrast for filament recognition. Image analysis was performed using a custom built MATLABTM code to track the evolution of the filament over time. For image processing, the top and bottom of the filament was manually located, and the code tracked the evolution of a range of 20 points above and below the midpoint.

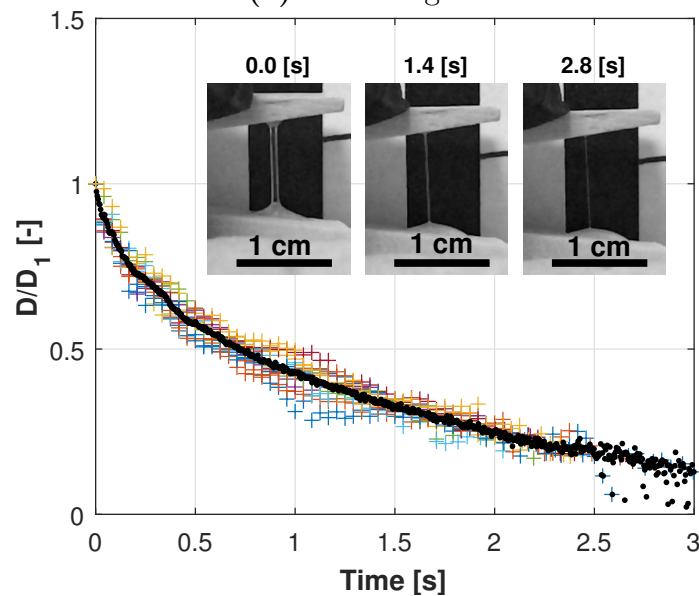
3.4 Results & Discussion

3.4.1 Step-strain Comparison

To compare the index-finger and clothespin methods depicted in Figure 3.2(c-d), a 660-ppm Boger fluid was tested using each step-strain technique. For the present trials, the final sample height was chosen to be the same length as a fully extended clothespin, approximately 10 mm. The normalized-diameter-decay profiles for ten trials of each technique are presented in Figure 3.3. Overall, decay profiles were found to be relatively repeatable with minor fluctuations arising from problems tracking the filament. When comparing the two step-strain techniques, both data sets show good agreement, having similar exponential trends. The characteristic relaxation times for these trials are presented below. For the index-finger method, however, controlling the final height in which the sample was stretched proved challenging and led to variations in starting diameter. Average starting diameters were approximately 0.6 ± 0.1 mm for the index-finger method and 0.7 ± 0.04 mm for the clothespin method.



(a) Index finger.



(b) Clothespin.

Figure 3.3: Comparison of results for the techniques providing an initial step-strain to a material. (a) Normalized diameter-decay profile using the index-finger method in an attempt to stretch and hold a sample at a set height. (b) Normalized diameter decay profile using the clothespin method to stretch and hold a sample at a set height. Ten trials were performed for each technique and the average of the ten trials is given (black-dotted curves). Diameter profiles were normalized by the diameter of the filament after the initial step-strain, D_1 . Images depicting the filament-breakup process are included for each technique.

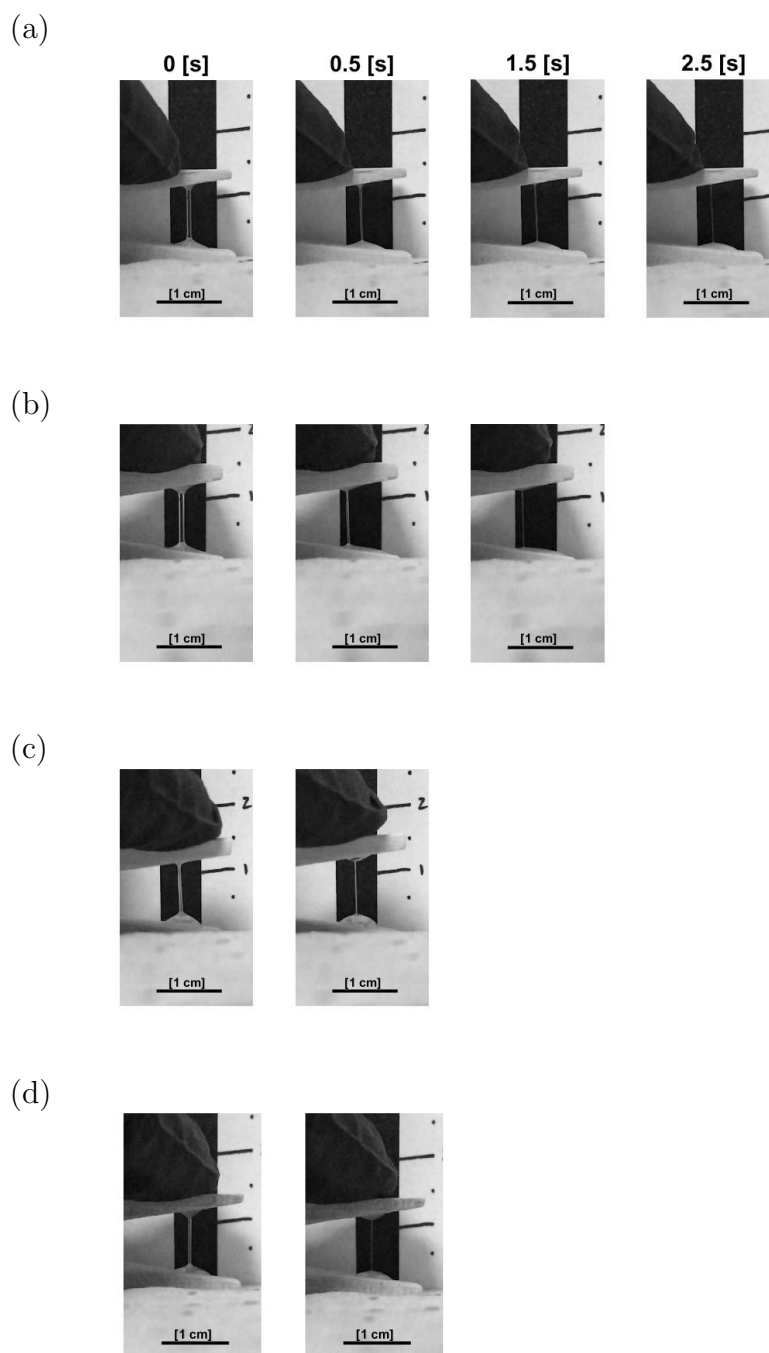


Figure 3.4: Filament decay profiles for concentrations of (a) 660 ppm, (b) 110 ppm, (c) 40 ppm, and (d) 20 ppm PEO in a glycerol/water solution. The time for filament breakup is dependent on the concentration of PEO in the solution.

Other challenges in performing the index-finger technique included controlling the rate of stretching as well as keeping one’s hand steady during the capillary-breakup event. Variability in the normalized-diameter-decay profiles in Figure 3.3(a), reflect these challenges. Relative to the index-finger method, the clothespin method provided a more precise means of stretching the sample (Figure 3.3(b)), and to have better control over the step-strain process, the remaining trials were performed using the clothespin technique.

3.4.2 DoS Comparison

To validate the use of a smartphone for taking extensional measurements, a series of Boger fluids (Table 3.1) were tested, and the results were compared with the results from the DoS technique (Figure 3.5). Plotting the natural logarithm of the normalized diameter profiles versus time, linear elasto-capillary regimes are observed for both techniques. The DoS results, however, also contain the transition of filaments from an inertio-capillary regime (where filament decay is rapid) into an elasto-capillary regime, as shown in the power-law necking dynamics observed at early times in Figure 3.5(a). The inertio-capillary regime is absent from the decay profiles in Figure 3.5(b), however, because elastic stresses had already significantly appreciated by the end of the initial step-strain. These variations in the decay profiles highlight the differences in pre-stretch history of the two techniques in which the startup processes are distinct for each technique.

For capillary breakup techniques, the amount of strain applied to a sample is important when evaluating a sample’s transient extensional properties. For example, when taking CaBER measurements, a pre-strain is included in the total Hencky strain, ($\epsilon_0 = 2 \log[D_0/D_1]$), arising from the initial separation of the plates [96]. In this equation, D_0 is the diameter of the sample prior to stretching, and D_1 is the diameter of the filament after the initial step-strain. For the present work, however, the characteristic relaxation time is the metric of interest, and the selection of D_0 and D_1 should not influence our abil-

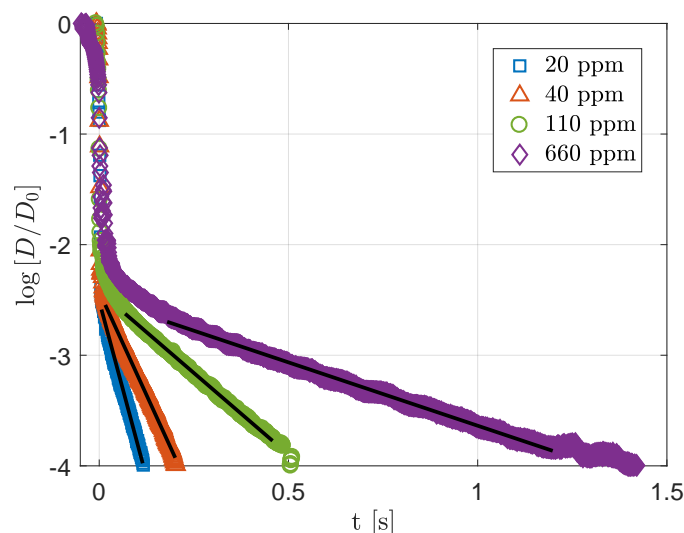
ity to extract such information from the filament thinning and breakup results. To confirm this assumption, a series of controlled experiments were performed, varying the volume and final height of the sample, and the resulting relaxation times were found to be unaffected.

Comparing the DoS and smartphone trials, the decay profiles of the Boger fluids (Figure 3.5) were fit to a linearized version of Equation 3.2, and the resulting characteristic relaxation times were evaluated and plotted versus concentration (Figure 3.6). The results for the clothespin trials appear to be sensitive to small changes in concentration, where increasing the concentration of PEO yielded greater characteristic relaxation times. The order of magnitude of the resulting relaxation times are in agreement with values reported in the literature [132]. Relative to the DoS results, however, the clothespin trials appear to have consistently higher relaxation times. Despite these findings, the slopes of the observed concentration dependencies are similar and consistent with the relationship reported by Dinic et al. ($\lambda_E \propto \Phi^\alpha$ and $\alpha = 0.65$) [3].

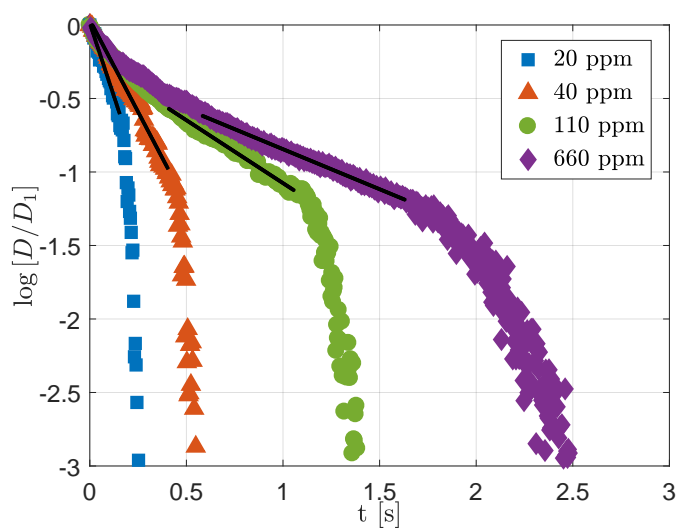
One possibility for the discrepancy in magnitude of the relaxation times taken using the clothespin and DoS techniques is that the start-up processes for these techniques affect the resulting relaxation measurements. The DoS technique, for example, requires an initial flow for the creation of an unstable filament, while the smartphone trials require startup and shutdown timescales that affect results, as shown in the CaBER literature [25]. Up to this date, no direct comparisons have been published between the CaBER and DoS techniques, partially as a result of the CaBER's limitations at low viscosities. Regardless, both the DoS and smartphone techniques appear to be sensitive to small changes in concentration.

3.4.3 Time-Scale Considerations

To explore technique limitations, a wide-range of fluids was selected for comparison. Among the Newtonian fluids tested, the filament breakup of the 55.8-wt% GLY solvent, the 200-mPa·s silicone oil, and the 350-mPa·s silicone oil were too rapid to be captured at 240 fps.



(a) Dripping-onto-Substrate (DoS).



(b) Smartphone.

Figure 3.5: Comparing the resulting decay profiles for the DoS and smartphone techniques. (a) Normalized diameter decay profiles for Boger fluids with PEO concentrations ranging from 20 ppm to 660 ppm tested using the DoS technique. The initial diameter, D_0 , is defined as the diameter of the syringe tip used to expel the sample [3]. (b) Averaged diameter results from the clothespin method for ten repetitions for Boger fluids with PEO concentrations ranging from 20 ppm to 660 ppm. Solid black lines on the diameter decay profiles indicate the exponential fits of the elasto-capillary regime.

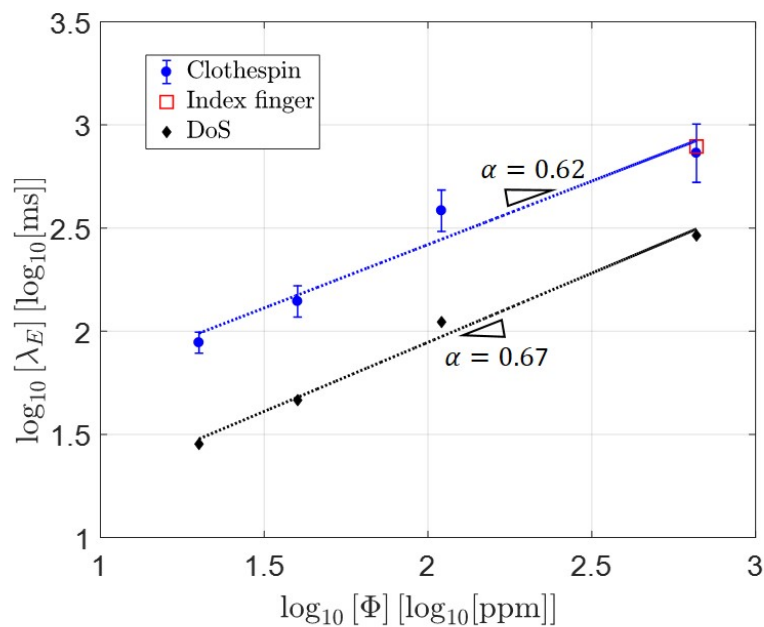


Figure 3.6: Resulting relaxation times (λ_E) versus concentration (Φ) for the DoS (black diamonds) and clothespin (blue circles) techniques. Dashed lines indicate a power law fit of the relaxation time versus concentration, $\lambda_E \propto \Phi^\alpha$. The clothespin relaxation times represent the average relaxation times over ten trials, with error bars representing the standard deviation of these trials. A single point (red square) for the index-finger method is plotted for the 660-ppm Boger fluid and shows good agreement with the clothespin method.

Using a silicone oil with an increased viscosity of 4,870 mPa·s slowed the breakup process, allowing for extensional measurements to be made. For the viscoelastic samples containing PEO, despite these fluids having viscosities on the order of 10 mPa·s, the additional elastic stresses aided in the resisting of filament breakup, allowing for measurements to be taken. Under optimal conditions, the CaBER has been projected to measure relaxation times as low as 1 ms for fluids with shear viscosities of 3 mPa·s or greater [25]. More conservatively, ThermoFischer Scientific lists a shear-viscosity range for the HAAKE™ CaBER™ between 10 and 10^6 mPa·s, depending on the elasticity of the sample.

A more appropriate description of CaBER limitations employs the non-dimensional numbers describing the operation window of filament stretching devices. For flows that describe “self-thinning” processes, such as the capillary thinning and breakup of cylindrical filaments in which no externally imposed driving forces exist, one may consider a set of dimensionless parameters clearly outlined by McKinley [2]. For this process, three important timescales are considered that describe the viscous, inertial, and polymeric contributions to the filament-thinning dynamics.

The elastic timescale is the timescale associated with the longest relaxation time of polymer in solution. Additionally, the viscous timescale is the timescale for a capillary-driven breakup event to occur due to competing viscous and capillary forces, $t_{vb} \sim \eta_0 \ell / \sigma$, and will be discussed in more detail below. The Rayleigh timescale that describes the breakup of an inviscid jet ($t_R = [\rho \ell^3 / \sigma]^{1/2}$) is often used to express the magnitude of inertial effects in capillary breakup processes [57]. Here, ℓ is the characteristic lengthscales of interest, ρ is the density, η_0 is the zero shear viscosity, and σ is the surface tension.

Comparing the above timescales, additional dimensionless groups can be evaluated. The Ohnesorge number compares the magnitude of viscous and inertial effects and is presented such that

$$Oh = \frac{t_{vb}}{t_R} \sim \frac{\eta_0}{[\rho \sigma \ell]^{1/2}}. \quad (3.4)$$

To define a low-viscosity fluid in capillary breakup experiments, the viscous timescale should be less than the inertial timescale such that the Ohnesorge number is less than unity, $Oh < 1$.

Additionally, a second dimensionless parameter arises when comparing the timescale for the stress relaxation to the Rayleigh timescale presented above. This ‘intrinsic’ Deborah number for free surface viscoelastic flows is defined as follows

$$De_{int} = \frac{\lambda}{t_R} = \lambda \left[\frac{\sigma}{\rho \ell^3} \right]^{1/2} \quad (3.5)$$

and is independent of flow properties such as velocity.

For the CaBER, fluids must be sufficiently viscous or elastic to resist the capillary-driven necking. Thus, the limitations for the CaBER can more generally be stated that for low-viscosity samples where the Ohnesorge number is less than unity the Deborah number must be greater than unity, and for weakly-elastic or Newtonian samples where the Deborah number is less than unity, the Ohnesorge number must be greater than unity for a measurement to be taken [2, 25].

As a consequence of the rapid timescales associated with filament breakup for less viscous and weakly elastic fluids, the ability to record a breakup event is limited by a smartphone’s camera technology and the method used to apply the initial step-strain. Although rapidly advancing, smartphone cameras currently only capture 240 fps with their slow-motion settings. To better understand the sampling limitations for capturing a breakup event, we will consider the timescales associated with the breakup of Newtonian and viscoelastic fluids in a similar manor described by Rodd et al. [25] for evaluating the CaBER.

Evaluating limitations for Newtonian samples: At early viscous times for capillary breakup, elastic stresses are negligible, and the filament decays according to

$$D(t) = D_1 - \frac{(2\beta - 1) \sigma}{3 \mu} t, \quad (3.6)$$

developed from slender body theory [53]. Here β has been numerically evaluated to be 0.71 for a viscous filament, derived from the similarity solution for visco-capillary breakup [62]. Rearranging this expression, the viscous breakup time ($t_{vb} = 7.1\mu D_1/\sigma$) can be evaluated by setting $D(t_{vb}) = 0$.

For Newtonian samples, the intrinsic Deborah number limits to zero. Thus, for a measurement to be possible, the Ohnesorge number must be greater than or equal to unity, as previously described. For a 1-mm filament of oil with a density similar to water and surface tension around 20 mN/m, the viscosity should be greater than 150 mPa·s.

This estimate, however, neglects the limitations of the high-speed camera. Assuming that a minimum of 10 data points (frames) are needed for crude data processing and neglecting the finite time required for a sample to be stretched, for the clothespin method having an initial diameter of roughly 1 mm, a fluid with a surface tension of approximately 72 mN/m would require a viscosity of nearly 430 mPa·s to be evaluated at 240 fps. Reintroducing the finite time required to stretch the sample only increases this minimum estimate.

Of the three Newtonian fluids tested, only the 4,870 mPa·s silicone oil was measurable. Having lower surface tensions, according to Equation 3.6, these Newtonian fluids should be measurable at viscosities above 130 mPa·s. Since the 200- and 350-mPa·s silicone oils fell within the estimated range of measurability, these results reflect the importance of the initial step-strain on the ability to capture the filament-decay profile, revealing one advantage that the DoS technique has over the commercially available CaBER. Considerations for integrating the DoS technique with a smartphone are discussed in the conclusions.

Figure 3.7 contains a plot of the diameter versus time for fifteen trials of the 4,870-mPa·s silicone oil taken using the clothespin technique. Fitting the data using Equation 3.6 and knowing the surface tension to be 21.4 mN/m, the estimated viscosity was 4,544 mPa·s, having a true percent relative error of 6%. Although individual trials contain much more variability, fitting the average of the fifteen trials shows good agreement with the known viscosity of the standard. Furthermore, when fitting the individual trials the evaluated

viscosity was $4,762 \pm 712$ mPa·s, still within a reasonable range of the true value. Knowing the viscosity of the silicone oil, the surface tension can also be determined. Using the same procedure, except solving for surface tension, the surface tension for the 4,870 silicone oil was found to be 22.9 mN/m.

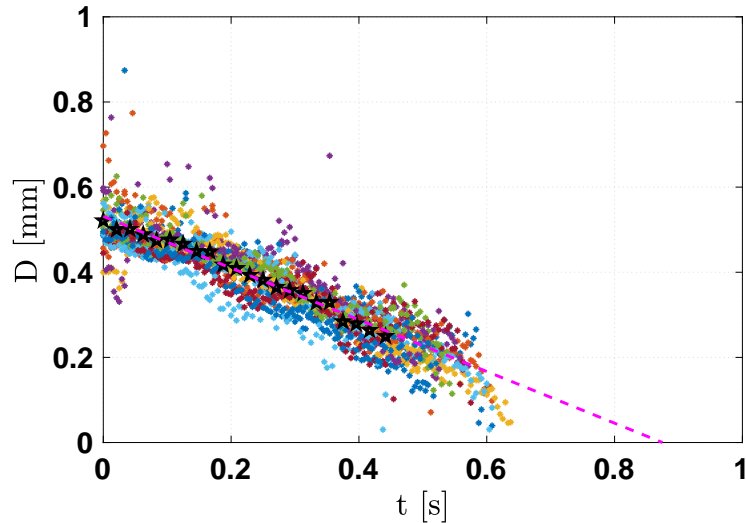


Figure 3.7: Results for fifteen trials of the 4,870-mPa·s silicone oil. The normalized diameter is plotted versus time. The average of the fifteen trials (black stars) and the linear fit (blue line) are also included.

Evaluating limitations for viscoelastic samples: To evaluate the limitations for viscoelastic fluids, the necking of viscoelastic threads of low viscosity are often considered [25, 66, 119]. Here, the timescale of elastic-stress growth is represented by the characteristic relaxation time, λ_E . For the inertio-capillary breakup of an inviscid jet, the Rayleigh timescale is used to describe the timescale of the breakup event [25, 66, 119, 133]. Again, for a stable filament to form, the growth in elastic stresses must overcome the growth in perturbations caused by the capillary-driven instability. The ratio of these two timescales is the intrinsic Deborah number [2, 119]. Issues with the above analysis include the neglect of the initial step-strain and the absence of viscous-stress considerations. Furthermore, the

characterization of such low-viscosity elasticity is an ongoing challenge in the field of rheology and is out of the scope of the present text. Thus, for crude measurements of more viscous Newtonian and viscoelastic samples, the use of a handheld extensional device may prove valuable.

3.4.4 Length-Scale Considerations

One of the primary issues in using a smartphone camera without a macro-lens or other source of magnification is that the measurable length scales are greatly limited by current camera specifications. The iPhone 6, for example, has a sensor size of 4.80 mm \times 3.60 mm and a focal length of approximately 4.15 mm. Furthermore, at capture rate of 240 fps, the camera's resolution is 1280 pixels \times 720 pixels. At a known distance, the number of pixels per millimeter can be found using the relationship

$$\frac{\text{obj width [px]}}{\text{obj width [mm]}} = \frac{\text{image width [px]} \times \text{focal length [mm]}}{\text{sensor width [mm]} \times \text{obj distance [mm]}}. \quad (3.7)$$

Thus, at a distance of 30-70 mm the number of pixels per millimeter can be evaluated to be between 12 to 37 pixels/mm, depending on the orientation of the smartphone.

For initial filaments of around 1 mm, the object width is small both in absolute terms and relative to the size of the image, making the filament more challenging to detect. One option for improving measurements is to monitor the decay profile at a range of 41 pixels about the midpoint, along the length of the filament. For example, Figure 3.8 presents the diameter decay results for a range of points around the midpoint of the filament, for a single trial of the the 660-ppm Boger fluid. Note that the results are reported in terms of pixel length as a function of frames. The average of the results is also included. Depending on the position about the midpoint of the filament, the slopes of the individual decay profiles, calculated using Equation 3.2, fell within 10% of the average value. Thus, a small amount

of error is introduced by the location from which a measurement is taken. Ultimately, this variability is a result of the difficulty in tracking filaments of 10 or less pixels in width. As the pixel length decreases, the error in measurement increases. This trend is observed in the “fanning out” of the individual decay profiles as the filament size decreases in time.

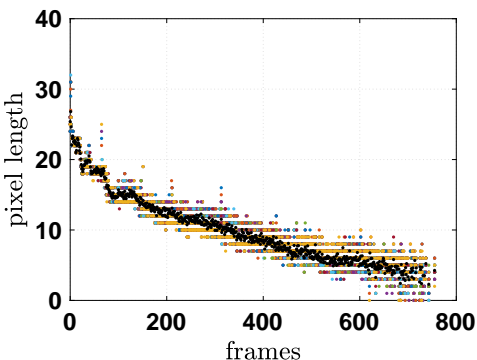


Figure 3.8: Diameter decay results for a range of 41 points along the length of a filament for the 660 ppm Boger fluid. The raw pixel length is plotted versus the frame number. The average of the results (black points) are included. Depending on the point along the length of the filament, the slope calculated from the line of best fit fell within 15% of the average. Thus, a small amount of error is introduced in the location along the filament from which a measurement is taken.

3.5 Conclusion and Future Work

The present study demonstrates the potential of a smartphone device in providing a robust means of performing capillary breakup extensional measurements. Boger fluids were tested using both smartphone and DoS techniques. Despite the low-cost use of a standard smartphone and a simple clothespin for performing extensional measurements, small changes in polymer concentration were detected. We suggest that differences in relaxation times between the DoS and clothespin techniques could be a consequence of the filament formation process, since relaxation dynamics are sensitive to the deformation history of the molecules within a solution.

Two main considerations moving forward are (1) exploring alternative methods for straining samples and (2) improving the quality of the image capturing process. The former could involve finding other means of providing a step-strain or developing a low-cost dripping-onto-substrate technique to be performed with a smartphone. In analyzing the important timescales in the step-strain technique, the finite-step time was identified as a limiting factor for measuring fluids with lower shear viscosity.

Nearing breakup, filaments appeared faint, making them challenging to detect via image processing. Such challenges emphasize the importance of the image capturing protocol on the ability to take a measurement. The latter consideration could involve magnifying the region of interest by integrating a macro-lens with a smartphone camera or by optimizing the position of the smartphone relative to the sample. Preliminary data collected using a macro-lens supports these hypotheses.

At a minimum, this work demonstrates the capacity for smartphone devices to be transformed into simple and low-cost rheometers to be used in the field. As developing communities are skipping the computer generation and joining the smartphone revolution, such technologies have the potential to serve as multifaceted tools that can improve peoples lives around the world while not being limited to the laboratory setting.

3.6 Acknowledgements

The authors would like to thank Aleesha Liedtke, Zach Wallace, Shelley Haug, Dr. Skip Rochefort, and Dr. Adam Higgins for their contributions to this work. In addition, the authors would like to thank Oregon State University's (OSU) Johnson Summer Internship program and the Saturday Academy's Apprenticeships in Science and Engineering (ASE) program for providing funding and interns to assist in this work. KAM would also like to thank the OSU Diversity Pipeline Fellowship for funding.

Chapter 4: General Conclusions

The overarching goal of the present thesis was to expand on current methods for extensional characterization. Two manuscripts were presented. The first manuscript addressed challenges in characterizing weak viscoelasticity and investigated droplet breakup in the cross-slot of a microfluidic device for taking extensional measurements. The benefits of this technique included small sample sizes and the ability to test fluids that are sensitive to air. Drawbacks of this technique included complexities in controlling the droplet-formation process.

In terms of future work, other means of introducing droplets into the splitting geometry should be explored. Furthermore, although the technique presented attempts to transport the well-known CaBER to the microscale, more efforts can be done to ensure that the deformation satisfies the assumptions being made in a typical capillary-breakup event. Although progress has been made in developing techniques to extend the range of fluids that can be tested, devices on the micro scale hold much promise.

The second manuscript presented explored a portable, low-cost means of capillary breakup extensional rheometry by employing the high-speed video capabilities of a smartphone device. At a minimum, this work demonstrated the capacity for smartphone devices to be transformed into simple and low-cost rheometers to be used in the field. Relative to the CaBER (MSRP\$40,000), smartphones are cheap and widely accessible. Such technologies are not limited to the laboratory setting, and have the potential to improve peoples lives around the world.

That being said, future work for an improved handheld extensional device could be to eliminate the step-strain required to initiate the capillary-breakup event. The finite time required to strain a material significantly reduces the range of fluids that can be tested, as

a result of the filament-breakup time being too rapid to capture via the current capture rate of smartphones.

Additional next steps for handheld rheometry include exploring the use of smartphones for monitoring biological fluids such as cervical mucus to improve the quality of life for individuals in developing communities. Specifically, an application is desired for addressing women's reproductive health in developing communities. According to the United Nations Foundation, complications during a woman's pregnancy are one of the leading causes of death in women that are in their reproductive years. Furthermore, similar reports estimate maternal deaths could be prevented by improving access to family planning and maternal health services [134]. Future research could provide an inexpensive and simple-to-use method for measuring the properties of cervical mucus, allowing women to monitor their own reproductive health.

Bibliography

- [1] I. Teraoka, *Models of Polymer Chains* (Wiley, 2002)
- [2] G.H. McKinley, *Society of Rheology Bulletin* **2005**, 6 (2005)
- [3] J. Dinic, Y. Zhang, L.N. Jimenez, V. Sharma, *ACS Macro Letters* **4**(7), 804 (2015)
- [4] S.J. Haward, M.S. Oliveira, M.A. Alves, G.H. McKinley, *Physical Review Letters* **109**(12), 128301 (2012)
- [5] R.H. Ewoldt, M.T. Johnston, L.M. Caretta, in *Complex Fluids in Biological Systems* (Springer, 2015), pp. 207–241
- [6] V. van Steijn, C.R. Kleijn, M.T. Kreutzer, *Lab on a Chip* **10**(19), 2513 (2010)
- [7] J. Brandrup, E.H. Immergut, E.A. Grulke, A. Abe, D.R. Bloch, *Polymer Handbook*, vol. 7 (Wiley, 1989)
- [8] P.G. De Gennes, *Scaling Concepts in Polymer Physics* (Cornell University Press, 1979)
- [9] R.G. Larson, *Constitutive Equations for Polymer Melts and Solutions: Butterworths Series in Chemical Engineering* (Elsevier, 2013)
- [10] S.K. Lai, Y.Y. Wang, J. Hanes, *Advanced Drug Delivery Reviews* **61**(2), 158 (2009)
- [11] S.K. Lai, Y.Y. Wang, D. Wirtz, J. Hanes, *Advanced Drug Delivery Reviews* **61**(2), 86 (2009)
- [12] R. Brummer, *Rheology Essentials of Cosmetic and Food Emulsions* (Springer, 2006)
- [13] D. Wever, F. Picchioni, A. Broekhuis, *Progress in Polymer Science* **36**(11), 1558 (2011)
- [14] L. Zhong, M. Oostrom, M.J. Truex, V.R. Vermeul, J.E. Szecsody, *Journal of Hazardous Materials* **244**, 160 (2013)
- [15] T. Walker, T.T. Hsu, S. Fitzgibbon, C. Frank, D.S.L. Mui, J. Zhu, A. Mendiratta, G. Fuller, *Journal of Rheology* **58**(1), 63 (2014)
- [16] A. Gyr, H. Bewersdorff, *Drag Reduction of Turbulent Flows by Additives*, vol. 32 (Springer, 2013)
- [17] R.W. Paterson, F. Abernathy, *Journal of Fluid Mechanics* **43**(4), 689 (1970)
- [18] M. Doi, S.F. Edwards, *The Theory of Polymer Dynamics*, vol. 73 (Oxford University Press, 1988)

- [19] L.H. Sperling, *Introduction to Physical Polymer Science* (Wiley, 2005)
- [20] C. Clasen, J. Plog, W.M. Kulicke, M. Owens, C. Macosko, L. Scriven, M. Verani, G.H. McKinley, *Journal of Rheology* **50**(6), 849 (2006)
- [21] W.W. Graessley, *Polymer* **21**(3), 258 (1980)
- [22] P.J. Flory, *Principles of Polymer Chemistry* (Cornell University Press, 1953)
- [23] V. Tirtaatmadja, G.H. McKinley, J.J. Cooper-White, *Physics of Fluids* **18**(4), 043101 (2006)
- [24] G. Christopher, S. Anna, *Journal of Rheology* **53**(3), 663 (2009)
- [25] L.E. Rodd, T.P. Scott, J.J. Cooper-White, G.H. McKinley, *Applied Rheology* **15**(1), 12 (2005)
- [26] I.Z. Fisher, *Statistical Theory of Liquids*, vol. 28 (University of Chicago Press, 1964)
- [27] R.G. Larson, *The structure and rheology of complex fluids*, vol. 150 (Oxford University Press, 1999)
- [28] C.W. Macosko, R.G. Larson, *Rheology: Principles, Measurements, and Applications* (Wiley-VCH, 1994)
- [29] H.C. Öttinger, *Stochastic Processes in Polymeric Fluids: Tools and Examples for Developing Simulation Algorithms* (Springer Science & Business Media, 2012)
- [30] H. Yamakawa, *Annual Review of Physical Chemistry* **25**(1), 179 (1974)
- [31] S.J. Haward, *Biopolymers* **101**(3), 287 (2014)
- [32] D. Jones, K. Walters, *Rheologica Acta* **28**(6), 482 (1989)
- [33] F. Cogswell, *Transactions of the Society of Rheology* **16**(3), 383 (1972)
- [34] J.R. Collier, O. Romanoschi, S. Petrovan, *Journal of Applied Polymer Science* **69**(12), 2357 (1998)
- [35] D. James, K. Walters, in *Techniques in Rheological Measurement* (Springer, 1993), pp. 33–53
- [36] G.G. Fuller, C.A. Cathey, B. Hubbard, B.E. Zebrowski, *Journal of Rheology* **31**(3), 235 (1987)
- [37] F.J. Galindo-Rosales, M. Alves, M. Oliveira, *Microfluidics and Nanofluidics* **14**(1-2), 1 (2013)
- [38] S. Haward, *Biomicrofluidics* **10**(4), 043401 (2016)

- [39] A. Bazilevsky, V. Entov, A. Rozhkov, in *Third European Rheology Conference and Golden Jubilee Meeting of the British Society of Rheology* (Springer, 1990), pp. 41–43
- [40] G.H. McKinley, T. Sridhar, *Annual Review of Fluid Mechanics* **34**(1), 375 (2002)
- [41] M.I. Kolte, P. Szabo, *Journal of Rheology* **43**(3), 609 (1999)
- [42] G.H. McKinley, *Rheology Reviews* 2005 pp. 1–48 (2005)
- [43] J. Dinic, L.N. Jimenez, V. Sharma, *Lab on a Chip* **17**, 460 (2017)
- [44] P. Dontula, M. Pasquali, L. Scriven, C.W. Macosko, *Rheologica Acta* **36**(4), 429 (1997)
- [45] C.G. Hermansky, D.V. Boger, *Journal of Non-Newtonian Fluid Mechanics* **56**(1), 1 (1995)
- [46] N. Willenbacher, R. Hingmann, *Journal of Non-Newtonian Fluid Mechanics* **52**(2), 163 (1994)
- [47] P. Schümmer, K. Tebel, *Journal of Non-Newtonian Fluid Mechanics* **12**(3), 331 (1983)
- [48] A. Ardekani, V. Sharma, G. McKinley, *Journal of Fluid Mechanics* **665**, 46 (2010)
- [49] B. Keshavarz, V. Sharma, E.C. Houze, M.R. Koerner, J.R. Moore, P.M. Cotts, P. Threlfall-Holmes, G.H. McKinley, *Journal of Non-Newtonian Fluid Mechanics* **222**, 171 (2015)
- [50] K. Marshall, T. Walker, in *American Physical Society Meeting Abstracts* (2016). DOI 10.1103/BAmerican Physical Society.2016.DFD.H25.3
- [51] C.J. Petrie, *Journal of Non-Newtonian Fluid Mechanics* **137**(1), 15 (2006)
- [52] G.H. McKinley, A. Tripathi, *Journal of Rheology* **44**(3), 653 (2000)
- [53] A. Tripathi, P. Whittingstall, G.H. McKinley, *Rheologica Acta* **39**(4), 321 (2000)
- [54] P.W. Bridgman, *Dimensional Analysis* (Yale University Press, 1922)
- [55] M. Denn, K. Porteous, *The Chemical Engineering Journal* **2**(4), 280 (1971)
- [56] W.V. Ohnesorge, *ZAMM - Journal of Applied Mathematics and Mechanics* **16**(6), 355 (1936)
- [57] L. Rayleigh, *Proceedings of the London Mathematical Society* **1**(1), 4 (1878)
- [58] R.F. Day, E.J. Hinch, J.R. Lister, *Physical Review Letters* **80**(4), 704 (1998)
- [59] M.P. Brenner, J.R. Lister, H.A. Stone, *Physics of Fluids* **8**(11), 2827 (1996)
- [60] J. Eggers, *Physical Review Letters* **71**(21), 3458 (1993)

- [61] J. Eggers, *Reviews of Modern Physics* **69**(3), 865 (1997)
- [62] D.T. Papageorgiou, *Physics of Fluids* **7**(7), 1529 (1995)
- [63] M. Renardy, *Journal of Non-Newtonian Fluid Mechanics* **59**(2-3), 267 (1995)
- [64] L.R.S. R.S., *Philosophical Magazine Series 5* **34**(207), 145 (1892)
- [65] V. Entov, E. Hinch, *Journal of Non-Newtonian Fluid Mechanics* **72**(1), 31 (1997)
- [66] C. Clasen, J. Eggers, M.A. Fontelos, J. Li, G.H. McKinley, *Journal of Fluid Mechanics* **556**, 283 (2006)
- [67] R. Liang, M. Mackley, *Journal of Non-Newtonian Fluid Mechanics* **52**(3), 387 (1994)
- [68] P. De Gennes, *The Journal of Chemical Physics* **60**(12), 5030 (1974)
- [69] E. Hinch, *Polymères et Lubrification* pp. 351–372 (1974)
- [70] C. Wagner, L. Bourouiba, G.H. McKinley, *Journal of Non-Newtonian Fluid Mechanics* **218**, 53 (2015)
- [71] B.J. de Gans, P.C. Duineveld, U.S. Schubert, *Advanced Materials* **16**(3), 203 (2004)
- [72] N.F. Morrison, O.G. Harlen, *Rheologica Acta* **49**(6), 619 (2010)
- [73] A. Lindner, J. Vermant, D. Bonn, *Physica A: Statistical Mechanics and its Applications* **319**, 125 (2003)
- [74] W. Jones, *Journal of Non-Newtonian Fluid Mechanics* **28**(2), 255 (1988)
- [75] J.R. Van Wazer, H. Goldberg, *Journal of Applied Physics* **18**(2), 207 (1947)
- [76] S.L. Anna, G.H. McKinley, *Rheologica Acta* **47**(8), 841 (2008)
- [77] E. Miller, C. Clasen, J.P. Rothstein, *Rheologica Acta* **48**(6), 625 (2009)
- [78] S.H. Spiegelberg, D.C. Ables, G.H. McKinley, *Journal of Non-Newtonian Fluid Mechanics* **64**(2), 229 (1996)
- [79] L. Campo-Deano, C. Clasen, *Journal of Non-Newtonian Fluid Mechanics* **165**(23), 1688 (2010)
- [80] A. Bazilevskii, V. Entov, A. Rozhkov, *Polymer Science, Series A* **43**(7), 716 (2001)
- [81] A. Bazilevsky, V. Entov, A. Rozhkov, *Fluid Dynamics* **46**(4), 613 (2011)
- [82] M. Stelzer, G. Brenn, A. Yarin, R. Singh, F. Durst, *Journal of Rheology* **44**(3), 595 (2000)
- [83] A.L. Yarin, *Free Liquid Jets and Films: Hydrodynamics and Rheology* (Longman Publishing Group, 1993)

- [84] J. Cooper-White, J. Fagan, V. Tirtaatmadja, D. Lester, D. Boger, *Journal of Non-Newtonian Fluid Mechanics* **106**(1), 29 (2002)
- [85] Y. Amarouchene, D. Bonn, J. Meunier, H. Kellay, *Physical Review Letters* **86**(16), 3558 (2001)
- [86] O.A. Basaran, *AIChE Journal* **48**(9), 1842 (2002)
- [87] C. Wagner, Y. Amarouchene, D. Bonn, J. Eggers, *Physical Review Letters* **95**(16), 164504 (2005)
- [88] Y. Christanti, L.M. Walker, *Journal of Non-Newtonian Fluid Mechanics* **100**(1), 9 (2001)
- [89] Y. Christanti, L.M. Walker, *Journal of Rheology* **46**(3), 733 (2002)
- [90] V. Sharma, S.J. Haward, J. Serdy, B. Keshavarz, A. Soderlund, P. Threlfall-Holmes, G.H. McKinley, *Soft Matter* **11**(16), 3251 (2015)
- [91] P. Schummer, K.H. Tebel, *German Chemical Engineering* **5**, 209 (1982)
- [92] J. Savins, et al., *Society of Petroleum Engineers Journal* **4**(03), 203 (1964)
- [93] S.L. Anna, G.H. McKinley, D.A. Nguyen, T. Sridhar, S.J. Muller, J. Huang, D.F. James, *Journal of Rheology* **45**(1), 83 (2001)
- [94] D. Nguyen, R. Gupta, T. Sridhar, *Journal of Non-Newtonian Fluid Mechanics* **35**(2), 207 (1990)
- [95] J. Matta, R. Tytus, *Journal of Non-Newtonian Fluid Mechanics* **35**(2-3), 215 (1990)
- [96] S.L. Anna, G.H. McKinley, *Journal of Rheology* **45**(1), 115 (2001)
- [97] C. Clasen, M. Verani, J.P. Plog, G.H. McKinley, W. Kulicke, *Proceedings of the XIVth International Congress on Rheology* (2004)
- [98] P.C. Sousa, E.J. Vega, R.G. Sousa, J.M. Montanero, M.A. Alves, *Rheologica Acta* pp. 1–10 (2017)
- [99] L. Rodd, J. Cooper-White, D. Boger, G. McKinley, *Journal of Non-Newtonian Fluid Mechanics* **143**(2), 170 (2007)
- [100] P. Erni, M. Varagnat, C. Clasen, J. Crest, G.H. McKinley, *Soft Matter* **7**(22), 10889 (2011)
- [101] N. Kojic, J. Bico, C. Clasen, G.H. McKinley, *Journal of Experimental Biology* **209**(21), 4355 (2006)
- [102] S. Hudson, F. Phelan Jr, M. Handler, J. Cabral, K. Migler, E. Amis, *Applied Physics Letters* **85**(2), 335 (2004)

- [103] J.S. Lee, R. Dylla-Spears, N.P. Tecler, S.J. Muller, *Applied Physics Letters* **90**(7), 074103 (2007)
- [104] J. Odell, S. Carrington, *Journal of Non-Newtonian Fluid Mechanics* **137**(1), 110 (2006)
- [105] L.E. Rodd, T.P. Scott, D.V. Boger, J.J. Cooper-White, G.H. McKinley, *Journal of Non-Newtonian Fluid Mechanics* **129**(1), 1 (2005)
- [106] P.E. Arratia, J.P. Gollub, D.J. Durian, *Physical Review E* **77**(3), 036309 (2008)
- [107] D. Link, S.L. Anna, D. Weitz, H. Stone, *Physical Review Letters* **92**(5), 054503 (2004)
- [108] J. Husny, J.J. Cooper-White, *Journal of Non-Newtonian Fluid Mechanics* **137**(1), 121 (2006)
- [109] P. Garstecki, M.J. Fuerstman, H.A. Stone, G.M. Whitesides, *Lab on a Chip* **6**(3), 437 (2006)
- [110] J. Xu, S. Li, J. Tan, G. Luo, *Microfluidics and Nanofluidics* **5**(6), 711 (2008)
- [111] J. Xu, S. Li, J. Tan, Y. Wang, G. Luo, *AIChE Journal* **52**(9), 3005 (2006)
- [112] M. De Menech, P. Garstecki, F. Jousse, H. Stone, *Journal of Fluid Mechanics* **595**, 141 (2008)
- [113] J. Feng, L. Leal, *Journal of Non-Newtonian Fluid Mechanics* **90**(1), 117 (2000)
- [114] K.F. Lei, in *Microfluidics in Detection Science* (Royal Society of Chemistry, 2014), pp. 1–28
- [115] J. Friend, L. Yeo, *Biomicrofluidics* **4**(2), 026502 (2010)
- [116] MicroChem, *Permanent Epoxy Negative Photoresist Processing Guidelines For: SU-8 2100 and SU-8 2150*
- [117] A. Eshuis, P. Mijnlief, *Polymer* **27**(12), 1951 (1986)
- [118] M.S. Oliveira, G.H. McKinley, *Physics of Fluids* **17**(7), 071704 (2005)
- [119] P.P. Bhat, S. Appathurai, M.T. Harris, M. Pasquali, G.H. McKinley, O.A. Basaran, *Nature Physics* **6**(8), 625 (2010)
- [120] J. Li, M.A. Fontelos, *Physics of Fluids* **15**(4), 922 (2003)
- [121] S. Middleman, *Chemical Engineering Science* **20**(12), 1037 (1965)
- [122] S. Pongnumkul, P. Chaovalit, N. Surasvadi, *Journal of Sensors* **2015** (2015)
- [123] C. Cierpka, R. Hain, N.A. Buchmann, *Experiments in Fluids* **57**(6), 1 (2016)

- [124] Y. Kobori, P. Pfanner, G.S. Prins, C. Niederberger, *Fertility and Sterility* **106**(3), 574 (2016)
- [125] C. Collett, A. Ardron, U. Bauer, G. Chapman, E. Chaudan, B. Hallmark, L. Pratt, M.D. Torres-Perez, D.I. Wilson, *Plant Methods* **11**(1), 1 (2015)
- [126] B. Hallmark, M. Bryan, E. Bosson, S. Butler, T. Hoier, O. Magens, N. Pistre, L. Pratt, B.A. Ward, S. Wibberley, D.I. Wilson, *Measurement Science and Technology* **27**(12), 125302 (2016)
- [127] S.J. Haward, J.A. Odell, M. Berry, T. Hall, *Rheologica Acta* **50**(11-12), 869 (2011)
- [128] S.J. Haward, A. Jaishankar, M. Oliveira, M. Alves, G. McKinley, *Biomicrofluidics* **7**(4), 044108 (2013)
- [129] M. Stelzer, G. Brenn, A. Yarin, R. Singh, F. Durst, *Journal of Rheology* **46**(2), 507 (2002)
- [130] G.H. Mckinley, *Rheology Reviews* pp. 1–48 (2005)
- [131] J. Eggers, E. Villermaux, *Reports on Progress in Physics* **71**(3), 036601 (2008)
- [132] T.T. Hsu, T.W. Walker, C.W. Frank, G.G. Fuller, *Experiments in Fluids* **55**(1), 1 (2014)
- [133] J.W. Strutt, L. Rayleigh, *Proceedings of the London Mathematical Society* **10**(4) (1878)
- [134] L. Chola, S. McGee, A. Tugendhaft, E. Buchmann, K. Hofman, *PLOS one* **10**(6) (2015)

